



## Nomenclature

AM	Additive manufacturing	HIP	Hot isostatic pressing
BCC	Body-centered cubic	IPF	Inverse pole figure
CAD	Computer-aided design	LAGBs	Low angle grain boundaries
CALPHAD	Calculation of phase diagram	LDED	Laser directed energy deposition
CCAs	Complex concentrated alloys	LBM	Laser beam melting
CET	Columnar to equiaxed transition	LENS	Laser engineered net shaping
DED	Direct energy deposition	LMD	Laser melting deposition
DLD	Direct laser deposition	LPBF	Laser powder bed fusion
DLF	Direct laser fabrication	LSP	Laser shock peening
DMD	Direct metal deposition	MPEAs	Multi-principal element alloys
EBM	Electron beam melting	SEBM	Selective electron beam melting
EBS	Electron backscattered diffraction	SEM	Scanning electron microscope
EDS	Energy dispersive spectrum	SLM	Selective laser melting
EDX	Energy dispersive x-ray detector	STEM	Scanning transmission electron microscope
EELS	Electron energy loss spectroscopy	TEM	Transmission electron microscope
EPMA	Electron probe micro analyzer	VED	Volumetric energy density
FCC	Face-centered cubic	WAAM	Wire arc additive manufacturing
GND	Geometrically necessary dislocation	WHR	Work hardening rate
HCP	Hexagonal close-packing	XRD	X-ray diffraction
HEAs	High entropy alloys		
HAGBs	High angle grain boundaries		

## 1. Introduction

High entropy alloys (HEAs), also referred as multi-principal element alloys (MPEAs) and complex concentrated alloys (CCAs), were firstly reported by Yeh et al. [1] and Cantor et al. [2] in 2004, which was defined originally as an alloy that contains more than five principal elements with the concentration of each between 5% and 35%. Recently, the concept of HEAs has been extended to an alloy with four principal elements as well [3]. The underlying mechanism behind HEAs is to minimize the Gibbs free energy through a balance between enthalpy and entropy. To be specific, when a solid solution is formed from multiple elements, the change of configuration entropy is larger than that of most metallic materials, resulting in the formation of random solid solution during the solidification process instead of competing intermetallics or other complex phases [4,5]. Generally, HEAs exhibit a simple solid solution phase, such as body-centered cubic (BCC) [6,7], face-centered cubic (FCC) [8,9] or hexagonal close-packing (HCP) structures [10–12]. The combination of high entropy, severe lattice distortion, sluggish diffusion, short-range ordering and cocktail effects contributes to the high phase stability and excellent performance of HEAs [13,14], such as the combination of high yield strength and high ductility [15–17], excellent strength retention at cryogenic [18–20] and elevated temperatures [21,22], excellent thermal stability [23,24], high resistance to corrosion [25,26], oxidation [27,28], wear [29,30] and fatigue [31–33].

The multi-component HEAs are typically produced by conventional induction melting or vacuum arc melting followed by casting, which requires repeated remelting to achieve chemical homogeneity [34,35]. With the cooling rates of 10–20 K·s<sup>-1</sup>, conventional casting usually causes significant phase separation during the fabrication process of HEAs, where a post-treatment process is usually required to further adjust the microstructure for desired properties [13,36,37]. Besides, it is still difficult to overcome the inherent complexity and high degree of control needed to produce homogeneous bulk alloys in industry by traditional

manufacturing routes [38]. Therefore, there is an urgent need to develop effective and efficient techniques to fabricate this new class of alloys, among which the additive manufacturing (AM) methods that can generate fast cooling and solidification rates, and enable the production of complex geometries as well as the design of high freedom, have shown great potentials for producing HEAs as high-performance engineering materials [38,39].

AM, also known as rapid prototyping or 3D printing, has developed rapidly in the past few decades due to its ability to directly produce 3D parts layer by layer with near-net-shaping dimensions based on a computer-aided design (CAD) model. AM is especially suitable for fabricating geometrically complex parts with less consuming time. With such advantages, AM has been applied in almost all fields including automotive, aerospace, machinery, electronics, medical industries and building construction, etc. [38,40,41]. There are several AM techniques available for the fabrication and production of metallic materials, mainly including selective laser melting (SLM), laser melting deposition (LMD), electron beam melting (EBM) and wire arc additive manufacturing (WAAM) methods [40,42,43]. Each of these AM processes has its own characteristics which will be briefly summarized as follows.

SLM, also known as laser beam melting (LBM) [44,45] and laser powder bed fusion (LPBF) [46–48], is the most widely used powder bed-based AM technique. During the SLM process, a laser beam is used for melting and fusing the metal powders together. A thin layer of powder is spread evenly over the substrate or a previously deposited layer, and subsequently the laser beam selectively melts and fuses the powder particles, as dictated by the CAD model. For the SLM technique, several process parameters, mainly the laser power, laser scanning speed, layer thickness, hatching distance and scanning strategy, have to be carefully adjusted to fabricate defect-free parts with optimized microstructure and properties. Depending on the reactivity of the used metallic powders, the SLM process is usually performed in a closed chamber filled with an inert atmosphere such as argon or nitrogen. Additionally, the build chamber is also subject to an overpressure condition, which both help minimize

the oxygen contamination during the manufacturing process. A high cooling rate ranging from  $10^4$  to  $10^6$  K·s<sup>-1</sup> could be achieved during the SLM process [40,44]. By ensuring the quality of the metallic powders, precise dimensional control and good final homogeneity of the fabricated parts could be guaranteed with optimized processing parameters during this AM process [40,49].

LMD is another laser-based AM method with powder feed systems instead, which allows higher flexibility and throughput production via adjusting the raw material. LMD is also referred as laser engineered net shaping (LENS) [50,51], direct laser fabrication (DLF) [52,53], direct metal deposition (DMD) [42,54], direct laser deposition (DLD) [55,56], direct energy deposition (DED) [57,58] and laser directed energy deposition (LDED) [59] in some literatures. During the LMD process, metallic powders are dynamically fed into the laser beam spot and melted together with the previously deposited layer to build up a certain structure [60]. The laser melting pool is usually protected from oxidation by applying protection gases such as argon or nitrogen [44,61]. This method can apply two or more hoppers with different feeders [49], which is particularly attractive for the fabrication of HEAs as the requirement of pre-alloyed powders can be avoided by using elemental powders as feedstock. At the same time, it is possible to produce both chemically homogeneous and compositionally gradient materials by controlling the powders supply from different hoppers and in-situ alloying under optimized processing conditions [54,62,63]. Compared with the SLM technology, LMD provides a higher deposition rate and allows printing bulk samples of large dimensions [44,63]. One problem to be aware of is that the generated chemical composition may deviate from the starting powder composition due to the evaporation of some elements during this process [54].

EBM is a powder bed fusion technique with a high-power electron beam that functions as heating source to melt and fuse the metallic powders under vacuum, also referred as selective electron beam melting (SEBM) [64–66] in some literatures. EBM has a similar working principle with SLM, both of which use a layer-by-layer method to melt and fuse metallic powders [40]. The EBM process is carried out in a high vacuum atmosphere where the oxidation of the fabricated parts is usually averted. During the EBM process, preheating the powder bed is needed in order to prevent the structural deformation of the built part caused by residual thermal stress [67], which will affect the cooling rate and the final microstructure in as-manufactured components [44,68]. More process parameters are involved in the EBM process than other AM techniques, including beam power, beam focus, beam diameter, beam line spacing, beam scanning speed, plate temperature, preheating temperature, contour strategy, and scanning strategy. This EBM process is quite slow and thus makes the fabricated parts very expensive. In addition, there are restrictions in terms of the size of the built parts and the minimum size of cells in the lattice structure [44].

Essentially different from the metal powder-based AM techniques mentioned above, WAAM employs an electric arc as the heat source and metal filler wires as the feedstock materials, which is considered to be a cost-effective technology [43,69]. During the WAAM process of HEAs, considering the desired compositions, a combined cable of commercially available metal wires is usually used as raw materials, which can be fully melted to avoid materials loss due to unfused powders in the case of applying powder-based AM methods. Besides, WAAM also has the advantages of high deposition rate, low equipment and materials cost, enabling it suitable for the production of large-scale metal components [70–73]. Therefore, WAAM has emerged as a promising AM method for HEAs since last year. However, the use of WAAM to fabricate metal components also leads to drawbacks such as poor sub-optical surface quality, insufficient dimensional accuracy, and occasional low density due to vigorous melt pool interactions. In addition, the

relatively slow cooling rate and large heat source spot of WAAM may result in larger tensile residual stress and distortion of the fabricated parts [73–75].

The rapid solidification during above-mentioned AM processes can restrict the compositional segregation and the formation of the brittle intermetallics in the built parts, contributing to the strengthening effect through grain refinement [62,76,77], presenting great potentials for fabricating HEAs, which has gained increasing interest in the research community. It is worth noting that some of the previous AM research focused on HEAs coatings [55,78–87]. Here, we highlight the microstructure and properties of bulk HEAs fabricated by AM techniques. The first research work of additive manufactured HEAs was conducted by Kuncce et al. [88] in 2013. Subsequently, publications on this topic have shown a substantially increasing number over the last ten years (see Fig. 1), especially since 2019.

It should be noted that there are several review papers focusing on the AM of HEAs [36,60,89–93], which have provided important information on the microstructure and properties of HEAs; however, a systematic review article with regard to the detailed subsets on the microstructural characterization, mechanical and functional performance of AM in HEAs is still lacking. In the current work, we review the application of different AM techniques in different HEAs systems from the aspects of their detailed microstructures and properties in the following sections, providing a timely and comprehensive summary of this promising research topic to guide future developments. Specifically, a general summary of the applied alloying elements and detailed HEAs systems in AM field will be introduced in Section 2, and then Section 3 reviews the microstructural characterizations of additive manufactured HEAs from the perspectives of relative density, residual stress, crystal features, dislocation networks, element distribution, phases and precipitations as well as the effects of post-treatment. After that, the mechanical properties of printed HEAs parts will be reviewed in terms of hardness, tensile and compressive properties, cryogenic and high-temperature properties, fatigue and creep behavior as well as the post-treatment effect in Section 4, moreover, multiple strengthening mechanisms will also be discussed in Section 4. The functional properties including the corrosion resistance, oxidation behaviors, magnetic and hydrogen storage properties of additive manufactured HEAs will be reviewed in Section 5. Finally, the current challenges and future opportunities in this research field are proposed based on the current development trend.

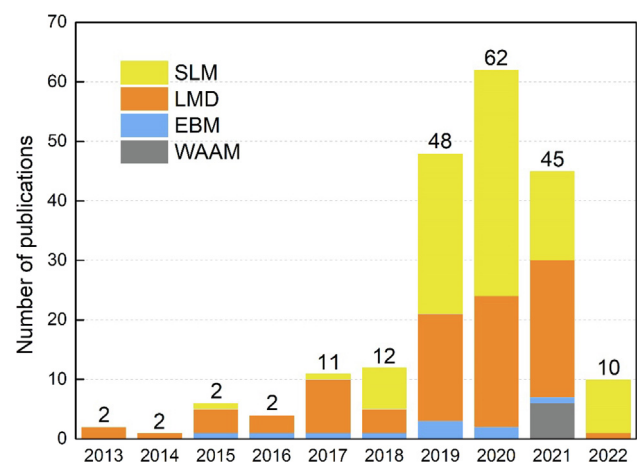


Fig. 1. Papers published since 2013 on AM HEAs (publications counted in 2022 until March 2022).

## 2. HEAs systems for additive manufacturing

Fig. 2 shows the alloying elements that have been selected for fabricating HEAs parts by AM techniques up to now, mainly including lightweight element Al, 3d transition metals, refractory metals, metalloid element Si and lanthanide element La, Sm. Some variants of the HEAs systems also include other substitutional or interstitial elements like C and N.

Table 1 gives information on the detailed HEAs systems used for AM by now, as well as on the phase compositions found by each investigation (which will be discussed in detail in Section 3.5), where available. In this review, all the HEAs systems mentioned are named alphabetically for summary and analysis. It can be seen that the AlCoCrFeNi and CoCrFeMnNi HEAs systems, based on the core group of transition metals, constitute the main group of these alloy classes developed through AM techniques. In addition, some other HEAs have also been explored in the AM field. For example, Dobbstein et al. [54,94,95] successfully demonstrated that LMD can be used to produce HfNbTaTiZr, MoNbTaW and NbTaTiZr HEAs, respectively, from a mixture of elemental powders through in-situ alloying. Considering the expected improved mechanical strength and service performance at elevated temperature, Sarswat et al. [96] combined 3d transition metals with refractory elements as well as lanthanide elements and Al to fabricate new hybrid HEAs namely AlCoFeNiSm<sub>0.1</sub>V<sub>0.9</sub>, AlCoFeNiSm<sub>0.1</sub>TiV<sub>0.9</sub> and AlCoFeNiSm<sub>0.05</sub>TiV<sub>0.95</sub>Zr. HEAs parts with gradient composition have also been produced by LMD technique, for evaluating the relationship between the composition, microstructure and properties. Gwalani et al. [97] successfully fabricated compositionally graded AlCrFeMoV<sub>x</sub> (0 < x < 1) HEAs with a length of ~20 mm. Another example of this possibility was illustrated by the work of Zhou et al. [98] where CoCrFeNiNb<sub>x</sub> HEA system was introduced with varying Nb content.

## 3. Microstructure characterization of additive manufactured HEAs

For additive manufactured metallic materials, the microstructures are often complex with varying spatial distribution arising from the complex temperature histories and layered structure.

Since the microstructure governs the materials' performances and potential improvement approaches, it is crucial to understand the microstructure evolution in additive manufactured materials. In this section, the relative density, residual stress, grain structure, texture and dislocation networks, element distribution, phase constituent, precipitations and post-treatment effects of additive manufactured HEAs are reviewed in detail.

### 3.1. Relative density

During the AM processes, the fabrication of parts with high relative density (typically > 99.5%) is usually the primary goal of process parameters optimization and control. Otherwise, high porosity in the components will facilitate crack propagation and thereby deteriorate mechanical performance [44,271].

Zhou et al. [246] studied the influence of SLM processing parameters on the density of printed C-containing CoCrFeNi HEAs. It was found that the density was quite sensitive to the processing parameters and a higher relative density (> 99%) can be obtained by increasing the scanning power or reducing the scanning speed. The density of C-doped CoCrFeMnNi HEAs was observed to firstly increase with increasing laser scanning speed and then decrease [217]. In order to describe the laser parameters more comprehensively, volumetric energy density (VED) has been introduced during laser-based AM techniques [185,240,272], which is defined as  $VED = P/(vht)$ , where  $P$  is the laser power (W),  $v$  is the scanning speed (mm·s<sup>-1</sup>),  $h$  is the hatching space (mm) and  $t$  is the layer thickness (mm). It turned out that the relative density of SLM-built CoCrFeMnNi first increased gradually with increasing VED, reaching its maximum value above 99.5% when the VED varied from 62.5 to 115.6 J·mm<sup>-3</sup>. However, further increasing VED would be detrimental to the surface finish and lead to dramatically decreased relative density of the produced HEAs, attributed to the keyhole effect and partial evaporation of certain elements, especially Mn, which has a higher vapor pressure and a lower melting point than other constituent elements [189]. The range of optimum VED (100~130 J·mm<sup>-3</sup>) for SLM-printed CrFeNiTiW was obtained through orthogonal experiments in [257]. By contrast, the AlCrCuFeNi and AlCoCrCuFeNi HEAs fabricated by SLM showed

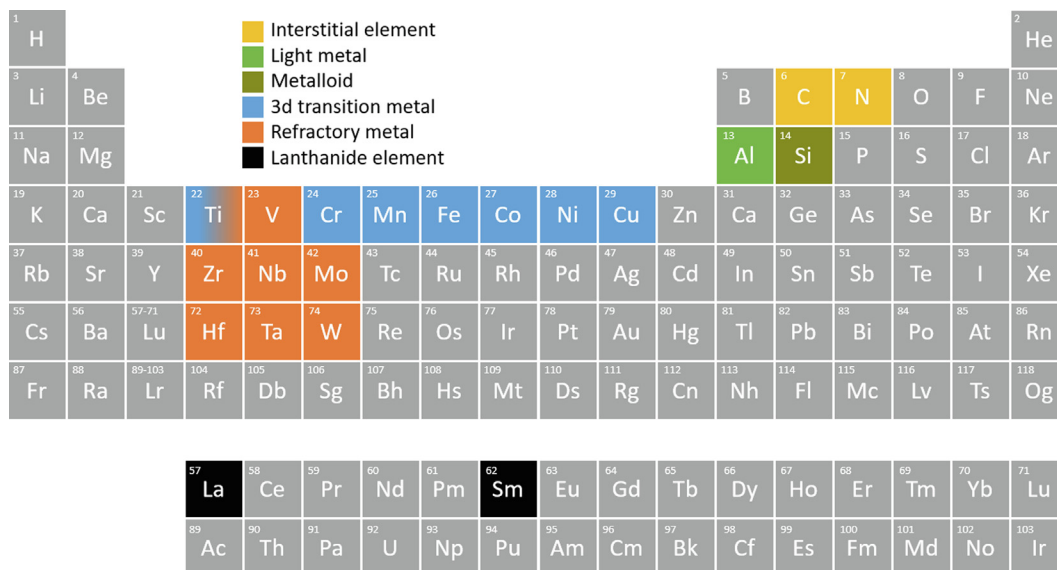


Fig. 2. Alloying elements groupings highlight the main ingredients used for AM HEAs.

**Table 1**  
Detailed HEAs systems used for AM.

HEAs systems	AM techniques	Phase compositions (Detailed HEA compositions)	Ref.
AlCoCrCuFeNi	SLM	FCC + BCC (AlCoCrCuFeNi)	[99]
	LMD	BCC + B2 (Al <sub>1.5</sub> CoCrCuFeNi)	[50]
AlCoCrCuFeNiTi	LMD	FCC + BCC (AlCoCrCuFeNi)	[100]
		BCC + L2 <sub>1</sub> (AlCo <sub>0.5</sub> CrCu <sub>0.5</sub> FeNi <sub>1.5</sub> Ti <sub>0.4</sub> )	[101]
AlCoCrCuFeNi + WC	SLM	FCC + WC + W <sub>2</sub> C + $\eta$ -carbide (20% AlCoCrCuFeNi + 80% WC)	[102]
AlCoCrFeMnNi	SLM	FCC (AlCo <sub>0.9</sub> CrFeMn <sub>0.9</sub> Ni), FCC + BCC + B2 + Oxides (AlCoCrFeMnNi)	[103]
AlCoCrFeMoNiW	LMD	FCC (Al <sub>0.1</sub> CoCrFeMnNi), FCC + BCC (Al <sub>0.26</sub> CoCrFeMnNi, Al <sub>0.43</sub> CoCrFeMnNi)	[104]
	SLM	FCC + B2 (Al <sub>18</sub> Co <sub>30</sub> Cr <sub>10</sub> Mo <sub>1</sub> Ni <sub>30</sub> W <sub>1</sub> )	[105]
AlCoCrFeNi	SLM	FCC (Al <sub>0.1</sub> CoCrFeNi)	[106]
		FCC (Al <sub>0.3</sub> CoCrFeNi)	[107]
AlCoCrFeNi	LMD	FCC (Al <sub>0.5</sub> CoCrFeNi)	[108]
		FCC + BCC (Al <sub>0.5</sub> CoCrFeNi)	[106,109]
		BCC (AlCoCrFeNi)	[110]
		BCC + B2 (AlCoCrFeNi)	[106,111]
		A2 + B2 (AlCoCrFeNi)	[112]
		BCC + Oxides (AlCoCr <sub>1.3</sub> FeNi <sub>1.3</sub> )	[103]
		FCC (Al <sub>0.3</sub> CoCrFeNi), FCC + BCC (Al <sub>0.6</sub> CoCrFeNi), BCC (Al <sub>0.85</sub> CoCrFeNi)	[34,113]
		FCC (Al <sub>0.3</sub> CoCrFeNi), FCC + BCC + B2 (Al <sub>0.6</sub> CoCrFeNi), BCC + B2 (Al <sub>0.85</sub> CoCrFeNi)	[114]
		FCC (Al <sub>0.2</sub> CoCrFeNi), FCC + BCC (Al <sub>0.45</sub> CoCrFeNi, Al <sub>0.7</sub> CoCrFeNi), BCC + B2 (AlCoCrFeNi)	[115]
		FCC (Al <sub>0.3</sub> CoCrFeNi <sub>1.7</sub> ), FCC + B2 (Al <sub>0.7</sub> CoCrFeNi <sub>1.3</sub> ), A2 + B2 + L1 <sub>2</sub> (AlCoCrFeNi), A2 + B2 (Al <sub>1.7</sub> CoCrFeNi <sub>0.3</sub> )	[116]
	EBM WAAM	FCC (Al <sub>0.3</sub> CoCrFeNi), FCC + BCC (Al <sub>0.7</sub> CoCrFeNi)	[117,118]
		FCC (Al <sub>0.3</sub> CoCrFeNi)	[52,119]
		FCC + B2 (Al <sub>0.3</sub> CoCrFeNi)	[120]
		FCC + B2 (Al <sub>x</sub> CoCrFeNi <sub>2.1</sub> , 0.6 ≤ x ≤ 1.1)	[121]
		BCC (AlCoCrFeNi)	[53]
		BCC + B2 (AlCoCrFeNi)	[51]
		BCC + B2 (AlCo <sub>x</sub> Cr <sub>1-x</sub> FeNi, 0 < x < 1)	[122,123]
		FCC + B2 (AlCoCrFeNi <sub>1.2</sub> )	[124]
		FCC + BCC (AlCoCrFeNi <sub>2.1</sub> )	[125]
		FCC + BCC (AlCo <sub>2.2</sub> CrFeNi, AlCo <sub>2.8</sub> CrFeNi)	[126]
FCC + B2 (Al <sub>18</sub> Co <sub>30</sub> Cr <sub>10</sub> Fe <sub>10</sub> Ni <sub>32</sub> )	[127]		
FCC + L1 <sub>2</sub> (Al <sub>7.1</sub> Co <sub>14.2</sub> Cr <sub>14.2</sub> Fe <sub>14.2</sub> Ni <sub>50</sub> ), FCC + L1 <sub>2</sub> + BCC (Al <sub>12.5</sub> Co <sub>12.5</sub> Cr <sub>12.5</sub> Fe <sub>12.5</sub> Ni <sub>50</sub> , Al <sub>16.7</sub> Co <sub>1.1</sub> Cr <sub>11.1</sub> Fe <sub>11.1</sub> Ni <sub>50</sub> )	[128]		
FCC + BCC + B2 (AlCoCrFeNi)	[64,67,129,130]		
FCC + BCC (Al <sub>2</sub> Co <sub>1.8</sub> Cr <sub>0.3</sub> Fe <sub>2.7</sub> Ni <sub>3.2</sub> )	[71,72]		
A2 + B2 (Al <sub>2.1</sub> Co <sub>0.3</sub> Cr <sub>0.5</sub> FeNi <sub>2.1</sub> )	[131]		
Al <sub>3</sub> Ni+(Ni, Co) <sub>3</sub> Al <sub>4</sub> (Al <sub>2.1</sub> Co <sub>0.3</sub> Cr <sub>0.5</sub> FeNi <sub>2.1</sub> )	[132]		
AlNi + CrFe + Al <sub>2</sub> FeCo (Al <sub>36.5</sub> Co <sub>4.9</sub> Cr <sub>8.6</sub> Fe <sub>16.4</sub> Ni <sub>33.7</sub> )	[133]		
FCC + BCC (AlCoCrFeNi + CoCrFeNi)	[134,135]		
AlCoCrFeNi/CoCrFeNi laminated structure	LMD		
AlCoCrFeNiTi	SLM	FCC (AlCoCrFeNiTi), FCC + BCC + B2 (AlCo <sub>0.8</sub> CrFeNiTi)	[103]
AlCoCrFeNiTi	LMD	FCC + Oxides (Al <sub>0.2</sub> Co <sub>1.5</sub> CrFeNi <sub>1.5</sub> Ti <sub>0.3</sub> )	[136]
		A2 + B2 (AlCoCrFeNiTi <sub>0.5</sub> )	[82,137]
		FCC + BCC + AlNi <sub>3</sub> intermetallic (AlCoCrFeNiTi)	[100]
		FCC (Al <sub>4</sub> (CoCrFeNi) <sub>94</sub> Ti <sub>2</sub> )	[138]
		-(AlCoCrFeNiTi)	[139]
AlCoCrFeNiTi/CoCrFeMnNi laminated structure	LMD	FCC + BCC (AlCoCrFeNiTi <sub>0.5</sub> + CoCrFeMnNi)	[140]
AlCoCrFeNiV	SLM	FCC (Al <sub>0.5</sub> CoCr <sub>0.8</sub> FeNi <sub>2.5</sub> V <sub>0.2</sub> )	[141]
AlCoCuFeNi	SLM	BCC (AlCoCuFeNi)	[142,143]
		BCC + B2 (AlCoCuFeNi)	[144]
AlCoFeMnNi	LMD	FCC (Al <sub>0.25</sub> CoCu <sub>0.75</sub> FeNi, Al <sub>0.5</sub> CoCu <sub>0.5</sub> FeNi), FCC + BCC (Al <sub>0.75</sub> CoCu <sub>0.25</sub> FeNi)	[145]
	SLM	FCC (Al <sub>0.26</sub> CoFeMnNi)	[47]
AlCoFeMnNi + C	SLM	-(Al <sub>0.26</sub> C <sub>0.12</sub> CoFeMnNi)	[47]
AlCoFeNi	LMD	BCC + B2 (AlCo <sub>x</sub> Cr <sub>1-x</sub> FeNi, 0 ≤ x ≤ 1)	[122]
AlCoFeNiSmTiV	SLM	FCC (AlCoFeNiSm <sub>0.1</sub> TiV <sub>0.9</sub> )	[96,146]
AlCoFeNiSmTiVZr	SLM	Several intermetallic such as Al-Sm, Al <sub>3</sub> V, Al <sub>3</sub> Zr, (Fe, Al) <sub>2</sub> Zr (AlCoFeNiSm <sub>0.05</sub> TiV <sub>0.95</sub> Zr)	[96]
AlCoFeNiSmV	SLM	FCC (AlCoFeNiSm <sub>0.1</sub> V <sub>0.9</sub> )	[96,146]
AlCoFeNiTi	SLM	-(Al <sub>7</sub> (CoFeNi) <sub>86</sub> Ti <sub>7</sub> )	[147]
AlCoFeNiTiVZr	SLM	FCC (AlCoFeNiTiVZr)	[96]
AlCrCuFeNbNi	LMD	FCC + BCC (AlCrCuFeNb <sub>x</sub> Ni, x = 0.05, 0.16, 0.26)	[148]
AlCrCuFeNi	SLM	BCC + B2 (AlCrCuFeNi)	[149,150]
		FCC (Al <sub>0.5</sub> CrCuFeNi <sub>2</sub> ), FCC + BCC + B2 (Al <sub>0.75</sub> CrCuFeNi <sub>2</sub> , Al <sub>1.0</sub> CrCuFeNi <sub>2</sub> )	[151]
AlCrCuFeNiW	LMD	FCC + BCC + B2 (AlCrCuFeNi <sub>x</sub> , x = 2.0, 2.5, 2.75, 3.0, 3.5)	[150,152,153]
		FCC + L1 <sub>2</sub> + BCC + B2 (Al <sub>0.8</sub> CrCuFeNi <sub>2</sub> , Al <sub>1.0</sub> CrCuFeNi <sub>2</sub> ), FCC + BCC + B2 (Al <sub>1.3</sub> CrCuFeNi <sub>2</sub> , Al <sub>1.5</sub> CrCuFeNi <sub>2</sub> )	[5,154]
AlCrCuFeNiW	LMD	FCC + BCC (AlCrCuFeNi)	[148,155]
		FCC + BCC (AlCrCuFeNiW <sub>x</sub> , x = 1% and 3%)	[155]
AlCrFeMoV	LMD	BCC (AlCrFeMoV <sub>x</sub> , 0 < x < 1)	[97]
AlCrFeNi	SLM	FCC + BCC + B2 (AlCrFe <sub>2</sub> Ni <sub>2</sub> )	[156]
	LMD	BCC + B2 (AlCrFeNi)	[97]
		FCC + BCC + B2 (AlCrFe <sub>2</sub> Ni <sub>2</sub> )	[157]

(continued on next page)

Table 1 (continued)

HEAs systems	AM techniques	Phase compositions (Detailed HEA compositions)	Ref.
AlCrFeNiV	SLM	FCC + L1 <sub>2</sub> (Al <sub>0.5</sub> Cr <sub>0.9</sub> FeNi <sub>2.5</sub> V <sub>0.2</sub> )	[158]
		- (Al <sub>0.5</sub> CrFeNi <sub>2.5</sub> V <sub>0.2</sub> )	[159]
AlCrMoNbTa	EBM	BCC (Al <sub>0.5</sub> CrMoNbTa <sub>0.5</sub> )	[160]
		BCC + Cr <sub>2</sub> Nb intermetallic phases (Al <sub>0.5</sub> CrMoNbTa <sub>0.5</sub> )	[161]
CoCrCuFeNi	LMD	- (CoCrCu <sub>0.5</sub> FeNi)	[162]
CoCrCuFeMnSi	SLM	FCC + HCP (Co <sub>20</sub> Cr <sub>15</sub> Cu <sub>1.5</sub> Fe <sub>38.5</sub> Mn <sub>20</sub> Si <sub>5</sub> )	[163]
CoCrFeMn	SLM	FCC + HCP (Co <sub>10</sub> Cr <sub>10</sub> Fe <sub>50</sub> Mn <sub>30</sub> )	[164]
	LMD	FCC + HCP (Co <sub>10</sub> Cr <sub>10</sub> Fe <sub>50</sub> Mn <sub>30</sub> )	[165,166]
CoCrFeMn + C	SLM	FCC (Co <sub>10</sub> Cr <sub>10</sub> Fe <sub>49.5</sub> Mn <sub>30</sub> Co <sub>0.5</sub> )	[167]
	LMD	FCC (Co <sub>10</sub> Cr <sub>10</sub> Fe <sub>49.5</sub> Mn <sub>30</sub> Co <sub>0.5</sub> )	[168]
CoCrFeMnNbNi	LMD	- ((CoCrFeMnNi) <sub>1-x</sub> Nb <sub>x</sub> , 0 < x < 0.3)	[169]
CoCrFeMnNi	SLM	FCC (CoCrFeMnNi)	[46,170-184]
		FCC + σ (CoCrFeMnNi)	[185]
		FCC + HCP (CoCrFeMnNi)	[186]
		FCC + Oxides (CoCrFeMnNi)	[187]
		FCC + ω (CoCr <sub>1.3</sub> FeMnNi <sub>0.7</sub> )	[103]
		- (CoCrFeMnNi)	[188-195]
	LMD	FCC (CoCrFeMnNi)	[18,19,58,59,104,196-209]
		FCC + BCC (CoCrFeMnNi)	[210]
		FCC ((CoCrFeMnNi) <sub>1-x</sub> Fe <sub>x</sub> , x = 0.1, 0.2, 0.3, 0.4, 0.5),	[211]
		FCC + BCC ((CoCrFeMnNi) <sub>0.4</sub> Fe <sub>0.6</sub> )	
		- (CoCrFeMnNi)	[212]
CoCrFeMnNi + C	EBM	FCC (CoCrFeMnNi)	[213,214]
	SLM	FCC (CoCrFeMnNi + 1% C)	[215,216]
		FCC (CoCrFeMnNi + 0.2% C)	[217]
		FCC ((CoCrFeMnNi) <sub>100-x</sub> C <sub>x</sub> , x = 0.5, 1.0, 1.5)	[218]
CoCrFeMnNi + CeO <sub>2</sub>	LMD	FCC + Oxides (CoCrFeMnNi + 1% CeO <sub>2</sub> )	[219]
CoCrFeMnNi + Fe-based metallic glass	SLM	FCC + amorphous phase (CoCrFeMnNi + x%)	[220]
		(Fe <sub>43.7</sub> Co <sub>7.3</sub> Cr <sub>14.7</sub> Mo <sub>12.6</sub> C <sub>15.5</sub> B <sub>4.3</sub> Y <sub>1.9</sub> ), x = 5, 10, 20, 30)	
CoCrFeMnNi + N	SLM	FCC (CoCrFeMnNi + 50% N <sub>2</sub> mixed with Ar)	[179]
CoCrFeMnNi-(N, Si)	SLM	FCC + amorphous phase (Co <sub>20.26</sub> Cr <sub>19.43</sub> Fe <sub>21.69</sub> Mn <sub>16.83</sub> Ni <sub>20.45</sub> N <sub>0.92</sub> Si <sub>0.42</sub> )	[221]
CoCrFeMnNiTa	LMD	- ((CoCrFeMnNi) <sub>1-x</sub> Ta <sub>x</sub> , 0 < x < 0.9)	[169]
CoCrFeMnNiTi	EBM	FCC + CrFe + Cr <sub>2</sub> Ti + Ni <sub>3</sub> Ti (CoCrFeMn <sub>0.18</sub> NiTi), BCC + CrFe + Cr <sub>2</sub> Ti + Ni <sub>3</sub> Ti (CoCrFeMn <sub>0.5</sub> NiTi, CoCrFeMn <sub>2</sub> NiTi)	[214]
	LMD	- ((CoCrFeMnNi) <sub>1-x</sub> (TiAl <sub>6</sub> V <sub>4</sub> ) <sub>x</sub> , 0 < x < 1)	[169]
CoCrFeMnNi + TiAlV	LMD	FCC + TiB <sub>2</sub> (CoCrFeMnNi + 5% TiB <sub>2</sub> )	[206]
CoCrFeMnNi + TiB <sub>2</sub>	LMD	FCC + TiC (CoCrFeMnNi + 1% TiC)	[222]
CoCrFeMnNi + TiC	SLM	FCC + TiC (CoCrFeMnNi + 1% TiC)	[222]
	LMD	FCC + TiC (CoCrFeMnNi + x% TiC, x = 2.5, 5)	[204,223]
CoCrFeMnNi + TiN	SLM	FCC + TiN (CoCrFeMnNi + 5% TiN)	[224,225]
		FCC + TiN (CoCrFeMnNi + 12% TiN)	[226]
CoCrFeMnNi + WC	LMD	FCC + M <sub>23</sub> C <sub>6</sub> (CoCrFeMnNi + x% WC, x = 5, 10)	[204,227]
CoCrFeMnSi	SLM	FCC + HCP (Co <sub>20</sub> Cr <sub>15</sub> Fe <sub>40</sub> Mn <sub>20</sub> Si <sub>5</sub> )	[228]
		FCC + HCP ((Co <sub>10</sub> Cr <sub>10</sub> Fe <sub>50</sub> Mn <sub>30</sub> ) <sub>100-x</sub> Si <sub>x</sub> , x = 1, 3, 5)	[164]
CoCrFeMoNi	LMD	FCC (CoCrFeMo <sub>0.2</sub> Ni)	[229]
CoCrFeMoNiTi	SLM	FCC + HCP (Co <sub>1.5</sub> CrFeMo <sub>0.1</sub> Ni <sub>1.5</sub> Ti <sub>0.5</sub> )	[230]
		FCC (Co <sub>27</sub> Cr <sub>16</sub> Fe <sub>18</sub> Mo <sub>28</sub> Ni <sub>8</sub> Ti <sub>3</sub> )	[231]
	EBM	FCC + Ni <sub>3</sub> Ti (Co <sub>1.5</sub> CrFeMo <sub>0.1</sub> Ni <sub>1.5</sub> Ti <sub>0.5</sub> )	[65,230]
CoCrFeNbNi	LMD	FCC + Laves (CoCrFeNb <sub>x</sub> Ni, x = 0.1, 0.15, 0.2)	[98]
		FCC + Laves + Cubic Nb-rich phase (CoCrFe Nb <sub>0.2</sub> Ni <sub>2.1</sub> )	[232]
CoCrFeNi	SLM	FCC (CoCrFeNi)	[4,106,233-238]
		FCC (CoCr <sub>0.5</sub> FeNi)	[239]
		FCC + BCC + δ (Co <sub>23</sub> Cr <sub>21</sub> Fe <sub>21</sub> Ni <sub>35</sub> )	[240]
		FCC (CoCrFeNi <sub>3</sub> )	[128]
		FCC (Co <sub>15</sub> Cr <sub>10</sub> Fe <sub>60</sub> Ni <sub>15</sub> )	[241]
		- (CoCrFeNi)	[242]
	LMD	FCC (CoCrFeNi)	[98,115,134,243]
		FCC (Co <sub>x1</sub> Cr <sub>x2</sub> Fe <sub>x3</sub> Ni <sub>x4</sub> , x1 = 7-44, x2 = 5-32, x3 = 5-45, x4 = 19-58)	[244]
CoCrFeNi + Al alloy	LMD	- (12 % CoCrFeNi + AA5083 composite)	[245]
CoCrFeNi + C	SLM	FCC (CoCrFeNiC <sub>0.05</sub> )	[246,247]
		FCC + M <sub>23</sub> C <sub>6</sub> (CoCrFeNiC <sub>0.05</sub> )	[248]
CoCrFeNi + N	SLM	FCC (CoCrFeNi + 1.8% N)	[236,249]
CoCrFeNi + Diamond	SLM	FCC + Diamond + Cr <sub>7</sub> C <sub>3</sub> (CoCrFeNi / diamond composite)	[250]
CoCrFeNi + Ti-coated diamond	SLM	FCC + Diamond (CoCrFeNi / Ti-coated diamond composite)	[250]
CoCrFeNiSi	SLM	FCC (CoCrFeNiSi <sub>0.05</sub> )	[251]
CoCrFeNiTiW	SLM	BCC (CoCr <sub>2.5</sub> FeNi <sub>2</sub> TiW <sub>0.5</sub> )	[252]
		BCC + TiN (CoCr <sub>2.5</sub> FeNi <sub>2</sub> TiW <sub>0.5</sub> , under N <sub>2</sub> protective gas)	[252]
CoCrFeNiW	SLM	FCC + W (CoCrFeNiW <sub>0.2</sub> )	[253]
CoFeNiTi	LMD	FCC ((CoFeNi) <sub>100-x</sub> Ti <sub>x</sub> , x = 0, 1, 2, 3, 4)	[244]
CrCuFeNi	SLM	FCC (CrCuFeNi <sub>2</sub> )	[5,151]
CrCuFeTiV	LMD	FCC + BCC (CrCuFeTiV)	[254]
CrFeMnNi	SLM	FCC (CrFeMnNi)	[255]
CrFeMoNiTi	LMD	FCC + σ + Ni <sub>3</sub> Ti + Ti nitride ((CrFeNi) <sub>90</sub> Mo <sub>5</sub> Ti <sub>5</sub> ), σ + C14 Laves + Chi phase + Ni <sub>3</sub> Ti + TiN ((CrFeNi) <sub>80</sub> Mo <sub>10</sub> Ti <sub>10</sub> ),	[256]

Table 1 (continued)

HEAs systems	AM techniques	Phase compositions (Detailed HEA compositions)	Ref.
CrFeNiTiVZr	LMD	FCC + $\sigma$ + C14 Laves + Ni <sub>3</sub> Ti + TiN ((CrFeNi) <sub>80</sub> Mo <sub>15</sub> Ti <sub>5</sub> )	[88]
CrFeNiTiW	SLM	C14 Laves + $\alpha$ Ti-rich phase (CrFeNiTiVZr)	[257]
CuNbNiTiZrFeLaMnNiV	LMDLMD	FCC + Unknown phase (Cr <sub>4</sub> Fe <sub>9</sub> Ni <sub>6</sub> TiW)	[258,259]
		- ((CuNbTiZr) <sub>65</sub> Ni <sub>35</sub> )	[162]
		$\sigma$ + La(Ni,Mn) <sub>5</sub> (Fe <sub>0.2</sub> La <sub>0.03</sub> Mn <sub>0.4</sub> Ni <sub>0.17</sub> V <sub>0.2</sub> , Fe <sub>0.3</sub> La <sub>0.03</sub> Mn <sub>0.2</sub> Ni <sub>0.17</sub> V <sub>0.3</sub> , Fe <sub>0.16</sub> La <sub>0.06</sub> Mn <sub>0.33</sub> Ni <sub>0.28</sub> V <sub>0.16</sub> , Fe <sub>0.2</sub> La <sub>0.07</sub> Mn <sub>0.2</sub> Ni <sub>0.33</sub> V <sub>0.2</sub> ), FCC + La(Ni,Mn) <sub>5</sub> (Fe <sub>0.1</sub> La <sub>0.07</sub> Mn <sub>0.4</sub> Ni <sub>0.33</sub> V <sub>0.1</sub> , Fe <sub>0.1</sub> La <sub>0.1</sub> Mn <sub>0.2</sub> Ni <sub>0.5</sub> V <sub>0.1</sub> )	[260]
		BCC (HfNbTaTiZr)	[94,261]
HfNbTaTiZr	LMD	BCC (HfNbTaTiZr)	[262]
MoNbNiTa	SLM	BCC (MoNbNiTa)	[262]
MoNbNiTaTi	SLM	BCC (MoNbNi <sub>0.5</sub> TaTi <sub>0.5</sub> )	[262]
MoNbTaTi	SLM	BCC (MoNbTaTi)	[262]
MoNbTaTiZr	SLM	BCC (Mo <sub>0.6</sub> Nb <sub>0.6</sub> Ta <sub>0.6</sub> Ti <sub>1.4</sub> Zr <sub>1.4</sub> )	[263]
MoNbTaVW	SLM	BCC (MoNbTaVW)	[264]
MoNbTaW	SLM	BCC (MoNbTaW)	[265,266]
		BCC (MoNbTaW)	[267]
		BCC (MoNbTaW <sub>x</sub> , x = 0, 0.16, 0.33, 0.53)	[268]
		BCC (MoNbTaW, (MoNbTa) <sub>x</sub> W <sub>1-x</sub> , (MoTaW) <sub>x</sub> Nb <sub>1-x</sub> , 0 < x < 0.9)	[57]
		- (MoNbTaW)	[54]
MoNbTaWTi	WAAM	BCC (MoNbTaWTi)	[269]
MoNbTiVZr	LMD	BCC + NbTi <sub>4</sub> -type phase + $\alpha$ Zr-rich phase (MoNbTiVZr)	[270]
NbTaTiZr	LMD	BCC (NbTaTiZr)	[261]
		BCC (Nb <sub>x</sub> Ta <sub>25</sub> Ti <sub>25</sub> Zr <sub>50-x</sub> , 0 ≤ x ≤ 50)	[95]

high crack sensitivity, resulting in much narrower optimum processing window [99,149].

Wang et al. [213] first reported on the relationship between the density of HEA specimens fabricated by EBM techniques and the quality of feedstock powders. The entrapped gas pores existed in the CoCrFeMnNi powders resulted in a high porosity (1.19%) of HEA parts manufactured by EBM. Through careful adjustment and optimization of process parameters, a high-density sample with a value of 99.4% was successfully obtained. It was thus concluded that the granule density of powders rather than the sphericity was the main factor affecting the gas porosities of additive manufactured HEA parts, as the particle pores may directly aggravate to the deposited porosities [268].

For above-mentioned densification of additive manufactured HEAs, it can be concluded that the part density mainly depends on the applied powder quality and energy density. On the one hand, too low energy input will lead to unmelted material and thereby reduced density due to the formation of irregularly shaped voids, while the unstable melting pool tends to form balling and splashing under higher energy input, which renders easier formation of pores originating from the entrapped gas in the melt, leading to a decreased density [44,185,273]. On the other hand, dense and uniform alloys powder is beneficial to increase the relative density of additive manufactured components. Recently, a general and simplified model suitable for various metal materials has been proposed to predict the optimal energy density of SLM-fabricated parts, which has been verified with CoCrFeMnNi HEA [173] and a relative density of 99.9% has been achieved. According to this model, the energy absorption ( $Q_a$ ) of the powder bed should be 3–8 times higher than the energy consumption ( $Q_c$ ) to produce a near-full density parts. The  $Q_c$  during SLM process is mainly due to the heat required for the melting of the powder ( $Q_{\text{melting}}$ ), vaporization of metal powder ( $Q_{\text{vaporization}}$ ) and heat loss caused by heat convection and radiation ( $Q_{\text{heat loss}}$ ). The  $Q_a/Q_c$  ratio is strongly dependent on the material properties including the laser absorptivity, specific heat capacity and melting latent heat. It is shown that oxide layers on the outermost surface of the metal powder and also pores between the powders can significantly enhance the laser absorptivity during SLM process.

### 3.2. Residual stress

Residual stress is the self-equilibrating internal stress that remains in an object even in the absence of external forces or constraints acting on its boundary, which is commonly generated in rapid solidification manufacturing processes [233,274,275]. During the AM process, where the underlying material is reheated and partially remelted by a high-energy-intensity heat source while the subsequent layer is deposited, the dynamic thermal cycles of repeated rapid heating/cooling and high cooling rates in the molten pool can induce the accumulation of residual thermal stress in the solidified layer [198,202,276,277]. Thus, for additively manufactured components, the large thermal gradient along the building direction produces alternating tensile and compressive residual stresses between the underlying and subsequent layers [278]. The large and heterogeneous residual stress distribution inside the components may lead to distortion or crack initiation, thereby significantly deteriorating their performance. Therefore, it is crucial to quantitatively characterize the magnitude, distribution and evolution of residual stress in additive manufactured HEAs [203,279,280].

X-ray diffractometer is a conventional method to measure the residual stress in the top layer of the specimens [198,202]. Tong et al. [198] found that the residual stress state in the LMD-built CoCrFeMnNi HEA specimen had a tensile nature, where the stress initially decreased and then increased with increasing laser power. The as-built specimen fabricated at 600 W laser power had the highest tensile residual stress of ~440 MPa due to its higher cooling rate. When the laser power was increased to 1000 W, more laser energy inputs increased the size of the molten pool and aggravated the volume shrinkage of the solidified layer, resulting in an increase in the tensile residual stress again [198,281]. For SLM-printed CoCrFeNi HEA, Lin et al. [233,234] found that the residual tensile stress at the upper surface of the specimen had a value of 350 MPa. The authors pointed out that the residual stress along the width of the columnar grains was significantly larger than this surface stress, because the orientation distribution of the grains was random and the surface residual stress only represented the component of the stress parallel to the surface.

Neutron diffraction is another method applied for the measurement of residual stress, which provides non-destructively generated three-dimensional residual stress maps by scanning at relatively large depths in engineering materials [203,275,282]. Li et al. [203] applied neutron diffraction and finite element modelling to study the residual stress distribution in LMD-fabricated CoCrFeMnNi HEA, and the results are shown in Fig. 3. The inset in Fig. 3(a) shows the detailed measurement positions along the building direction, from the first deposition layer on the substrate to the position 10 mm below the upper surface. Fig. 3(a) shows the distributions of longitudinal ( $\sigma_L$ ), transverse ( $\sigma_T$ ), and normal ( $\sigma_N$ ) residual stresses for LMDed HEA specimens at different deposition heights. It indicates significant stress gradients, with all the stress components gradually decreasing along the building direction. The simulated contours of residual stress along the longitudinal direction of this LMD-deposited HEA is shown in Fig. 3(b), confirming the formation of a steep stress gradient along the entire deposition thickness. Such a pronounced residual stress gradient was closely related to the interaction of repeated thermal cycles and constraints. To be specific, since the substrate and powder materials were initially at room temperature, the rapid heating and cooling process during the AM process resulted in a steep temperature gradient in the first layer, causing the formation of high residual stress. The first layer was repeatedly expanded and shrunk as the subsequent layers were deposited, consequently, the subsequent layers could not shrink freely when the bulk sample was deposited with increasing its thickness due to the constraints of the previous

layer, resulting in compressive residual stresses in the previous layers close to the substrate and tensile residual stresses in the subsequent layers close to the sample surface, which was confirmed by the thermodynamic simulation (Fig. 3(b)) [283,284]. These findings allow better prediction of residual stresses in additive manufactured parts to optimize the process of fabricating high-performance and integrity components.

The elimination or relaxation of residual stress in additively manufactured materials can improve the mechanical behavior of materials such as tensile and fatigue resistance, thereby extending the service life [285]. It is well known that stress relaxation is mainly attributed to the slip and climb of dislocations at high temperature [286]. In addition to optimizing process parameters and scanning strategies to reduce thermal gradients and internal residual stresses in AM components [198,287], many post-treatment processes have been developed to address this issue, such as annealing, which will be discussed in Section 3.7.

### 3.3. Grain structure, texture and dislocation networks

Irrespective of the element compositions, one of the key advantages of additive manufactured HEAs compared with conventional processing technologies is its fast cooling rate, resulting from the localized heat input and a small amount of molten material, enabling the production of a finer microstructure of the fabricated components [44]. However, metal AM is a dynamic and complex manufacturing process composed of cyclic heating and cooling processes [288]. Consequently, the microstructural evolution of HEAs during AM usually leads to a complex microstructure, involving grains, texture and dislocation networks, which has become one of the focuses in this research field.

The microstructure analysis revealed much finer grains and dendrites produced by SLM in HEAs samples than those observed in as-cast samples [265]. Specifically, hierarchical structures including the molten pool, elongated columnar grains, sub-grain cellular structures and dislocation networks, were often observed in SLM-printed HEAs [158,170]. The inverse pole figure (IPF) map of SLM-printed AlCrFeNiV HEA from side view parallel to the building direction is shown in Fig. 4(a). The dashed white lines indicate the borders of molten pools, and grains indicated with a dominant red color show an FCC columnar structure with  $\langle 001 \rangle$  axis oriented preferably towards the building direction. The image quality map of the structure and superimposed distribution of low angle grain boundaries (LAGBs,  $2\text{--}10^\circ$ ) and high angle grain boundaries (HAGBs,  $> 10^\circ$ ) are presented in Fig. 4(b). The higher fraction of LAGBs was attributed to the cellular sub-grain microstructure of the SLMed HEA, which was composed of boundaries with dislocation walls, as shown in the corresponding transmission electron microscope (TEM) images (Fig. 4(c-e)). A notable heterogeneity of the dislocation distribution can also be noticed in this alloy, as two types of cellular sub-grains, one with few dislocations and the other with high density dislocations, can be found as shown in Fig. 4(d) and 4(e), respectively. While a coexisting cellular and columnar sub-grain structure in the grain interiors of SLM-fabricated C-containing CoCrFeNi HEA was obtained in Wu et al.'s work [248], where the sub-grain boundaries were decorated with entangled dislocation networks, as shown in Fig. 4(f-h). Moreover, an elemental segregation of Cr and Ni was detected at the cell boundaries in ferrous HEA [241], which might beneficially contribute to the generation of high dislocation density to release the strain energy produced by the steep solute concentration gradient at the cell boundaries. The dislocation networks at the walls and clean interiors of the cells are typical features of SLMed material [158,170,186,236,241,248]. It is generally believed that the generation of large thermal residual stress during SLM is associated

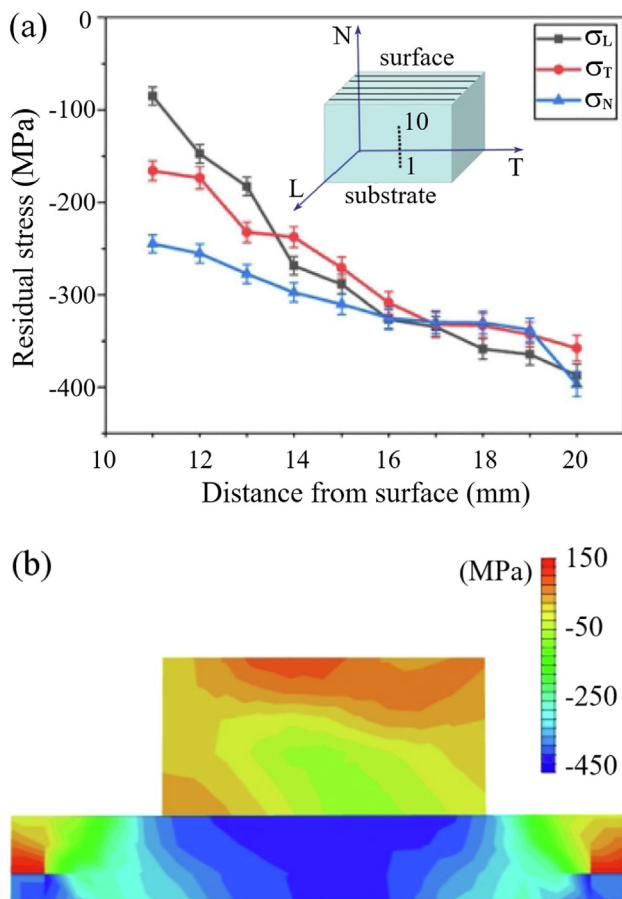


**Fig. 3.** (a) Distribution of residual stress components in the LMDed CoCrFeMnNi HEA specimen. The inset shows the measurement positions along the building direction. (b) Simulated contours of residual stress along the longitudinal direction. Adapted with permission [203]. Copyright 2019 Elsevier.

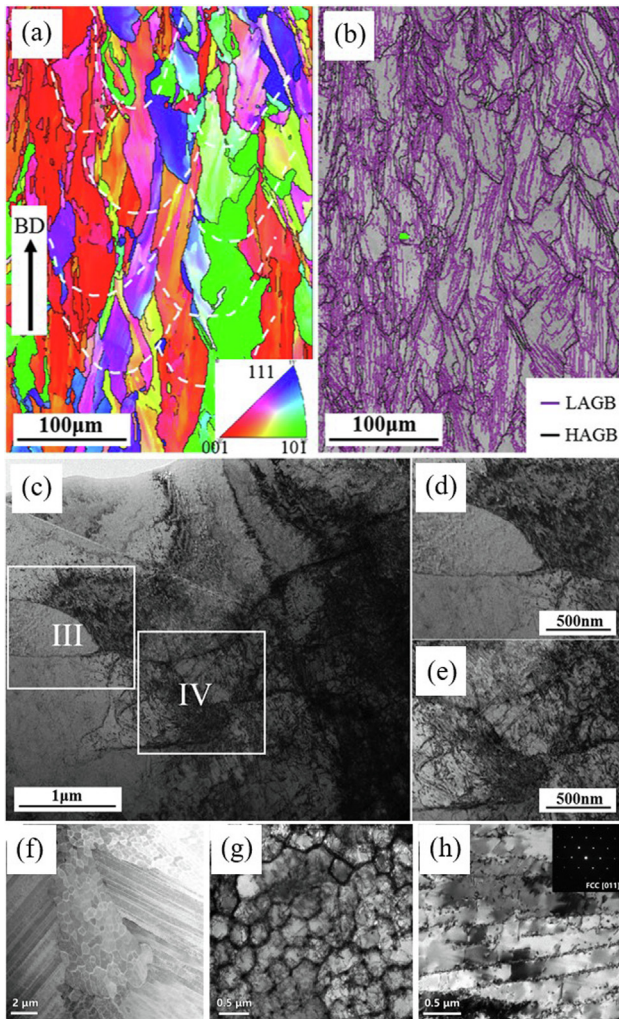


**Fig. 4.** (a) IPF map of SLMed AlCrFeNiV HEA and (b) its corresponding image quality map with superimposed LAGB and HAGB, (c) bright-field TEM images of the cellular sub-grains, (d–e) magnified micrographs of area III and IV indicated in (c). Adapted with permission [158]. Copyright 2019 Elsevier; (f) An HAADF STEM image of the co-existed cellular and columnar subgrains of SLMed C-containing CoCrFeNi HEA, (g) and (h) bright-field TEM images of the cellular and columnar structures, respectively. Adapted with permission [248]. Copyright 2018 Elsevier.

with the increased vacancy concentration and the resulting formation of dislocation networks in sub-grains [158].

According to [289], the mode of solidification is determined by the degree of constitutional undercooling during the metallurgical process. With the increase of constitutional undercooling, the solidification mode changes from planar to cellular, to columnar dendritic, and finally to equiaxed dendritic. The degree of constitutional undercooling for a certain alloy depends on the solidification parameters such as temperature gradient  $G$  and solidification rate  $R$ . For the one-layer deposition in AM process,  $G$  and  $R$  are the highest at the bottom and surface of the molten pool, respectively. The high temperature gradient provides the driving force for columnar grains growing along the gradient direction, leading to columnar grains formed perpendicular to the boundary of the molten pool [19,212]. Meanwhile, the increase of deposition height leads to heat accumulation at the top of the molten pool, resulting in a decrease in the  $G/R$  value, which corresponds to an increase in the degree of constitutional undercooling. As a result, the growth of crystals along the preferential orientation is restrained, leading to the occurrence of columnar to equiaxed transition (CET) [289]. A schematic representation of the microstructure characteristics

in the vertical section of a single melting pool along the building direction during the AM process is shown in Fig. 5 [198]. In addition to the preferentially oriented columnar grains and fine equiaxed grains discussed above, the multi-directional temperature gradients and lower cooling rates in the overlapping area facilitate the growth of columnar grains along multiple directions at the boundaries of the molten pool. The ratio of columnar grains to equiaxed grains can be tuned through changing the laser power and scanning strategies, as the CET is highly dependent upon the temperature gradient and heat flux direction under varying process parameters [19,89,178,199,207,208]. In addition, it was shown that the non-equiatomic composition of HEAs may also facilitate the CET and improve the formability of additive manufactured HEAs, such as the addition of Ni into the AlCrCuFeNi<sub>x</sub> [152] and Nb into the CoCrFeNiNb<sub>x</sub> system [98]. The addition of a non-equiatomic element would increase the degree of under-cooling of the liquid due to its severe partition between the liquid phase and the solid phase. Through fast solidification, crystal nuclei are easily formed in the undercooled melt, which then induces the CET [98]. Interestingly, Sistla et al. [116] found that, when decreasing the ratio of Al/Ni in the AlCoCrFeNi HEA system, the microstructure changed from dendritic structure to equiaxed one, however, without the occurrence of columnar structure. Sun et al. [242] studied the hot crack susceptibility of the SLMed CoCrFeNi HEA and reported poor laser printability for this alloy. The Rappaz-Drezet-Gremaud model [290] was employed to quantify the influence of grain size on the depression pressure in the mushy region caused by solidification shrinkage and mechanical strain. A higher depression pressure and thus, higher susceptibility for hot cracking was reported for this CoCrFeNi HEA compared to other common alloys due to its higher viscosity. According to the model, the fine-grained microstructure with higher fraction of grain boundaries can better withstand the residual stress and minimize hot cracking. Moreover, the formation of fine cellular structure can also induce the production of numerous dislocation tangles, contributing to the improved mechanical properties [198].

Both elongated grain features at the boundary which penetrated through several melting layers and a fine cellular dendrite

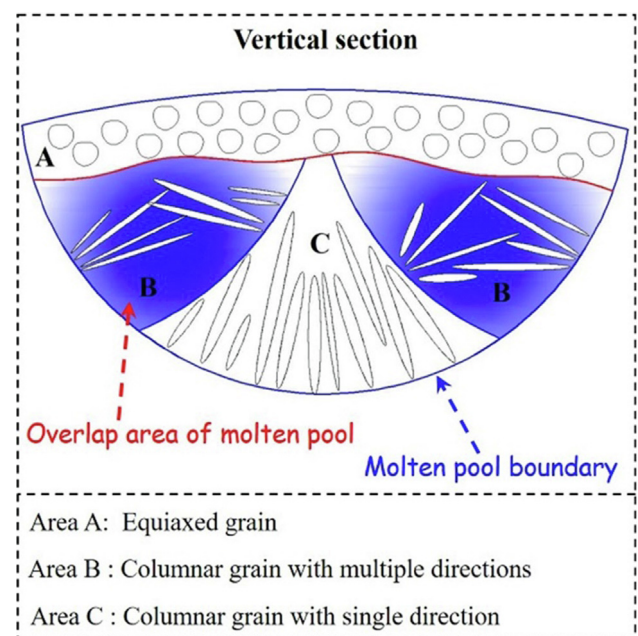


**Fig. 5.** Schematic representation of the microstructure characteristics along the cross section of a single molten pool during AM process. Reproduced with permission [198]. Copyright 2019 Elsevier.

structure within the melt pool with size between 2.9 and 5.2  $\mu\text{m}$  can be observed in LMD-fabricated CoCrFeMnNi HEA [196]. Similar microstructures have been reported repeatedly [149,199,201,210,213,257]. The local solidification and heat transfer conditions in the molten pool determined the morphology and growth direction of the cellular structure. As a result of the geometry of the elliptical molten pool and the partial remelting of the previously deposited layer, the grains were inclined against the laser movement direction and grew preferentially. The inherent high cooling rate of AM process may cause the suppression of equilibrium phases, while the resultant directional solidification favors the formation of pronounced crystallographic textures [44,62,101,171,196], resulting in anisotropic microstructures, where a very strong preferred  $\langle 001 \rangle$  orientation parallel to the building direction is usually observed in AM parts [46,52,142]. Process parameters will significantly affect the shape and thermal gradient of the molten pool and thus the crystallographic texture as the grains are oriented perpendicular to the boundary of the molten pool [107,112,197]. It was found that the crystalline texture of SLMed HEAs is particularly sensitive to the applied VED and scanning strategy [112,181,190]. A strong  $\langle 001 \rangle$  preferred orientation was observed in AlCoCrFeNi HEA when applying low VED, which gradually changed to the  $\langle 111 \rangle$  orientation at higher VED [112]. Whereas the preferred orientation of printed CoCrFeMnNi followed the transition  $\langle 233 \rangle \rightarrow \langle 001 \rangle \rightarrow \langle 203 \rangle \rightarrow \langle 101 \rangle$  with increasing VED [190]. Piglione et al. [46] pointed out that the microstructure evolution in the printed CoCrFeMnNi HEA was governed by the coupling of preferential growth and competitive grain selection after remelting. The grains were aligned with the  $\langle 001 \rangle$  crystallographic orientation induced by the preferential growth direction along the maximum heat flux. While a bi-directional scanning pattern generated an alternating sequence of the columnar grains dominated by two orientations, namely the  $\langle 001 \rangle$  and the  $\langle 011 \rangle$  orientation, respectively. Dovggy et al. [181] found that the  $0^\circ$ - and  $90^\circ$ -rotation scanning strategy led to the strongest  $\langle 100 \rangle$  texture while the  $67^\circ$ -rotation and chessboard scanning resulted in a much weaker texture, as the rotation angle between two consecutive layers can control the extent to which preferential growth can occur and the consequent crystallographic texture.

A compositionally graded AlCrFeMoV HEA system with varying V concentration was manufactured by LMD and it was highlighted that an increased V content would lead to an increment of grain size with regard to the reduced melting point of the HEA system [97]. Dobbstein et al. [95] conducted LMD on NbTaTiZr HEA system and observed that increasing the ratio of Zr to Nb beyond the equiatomic composition would yield a finer and harder microstructure, as shown in Fig. 6. An increased distance from the substrate led to the grains coarsening, which was more influenced by the composition segregation of Ta in Zr-rich zones than the cooling rate during the LMD process. These results demonstrated that the microstructure of HEAs parts manufactured by LMD from the elemental blend powders through in-situ alloying process can be tuned by varying the powder compositions.

The feasibility of fabricating HEAs by EBM was firstly demonstrated in [67], where a duplex microstructure with elongated grains along the building direction was observed. The average grain size of the AlCoCrFeNi sample manufactured by EBM was approximately 10  $\mu\text{m}$ , thirty times finer than that of the as-cast specimen with the same composition (300  $\mu\text{m}$ ), induced by the fast solidification and cooling rates during the EBM process [129]. The effectiveness of applying EBM to CoCrFeNiTi-based HEAs was compared with that of applying SLM [230]. The results show that a much finer uniform microstructure without visible segregation was formed during SLM. In addition, the SLM samples showed weaker crystal anisotropy along the building direction than that of

EBM samples as revealed by electron backscattered diffraction (EBSD) analysis, attributed to the different ratios of the temperature gradient (G) to the solidification rate (R) of the molten pools. It was demonstrated that the lower G/R ratio in the SLM process shows great potential in the generation of equiaxed grain structures. In contrast, the microstructure of WAAM-fabricated AlCoCrFeNi HEAs typically comprised dendrite grains with sizes ranging from 5 to 15  $\mu\text{m}$  and interdendritic regions [131–133], mainly due to the relatively slow cooling rate arising from the use of an electric arc as the heat source.

Different from the commonly observed columnar grain microstructure in previously reported HEAs, the LMD-built AlCoCrFeNiTi<sub>0.5</sub> samples exhibited a completely equiaxed grain structure in a wide range of solidification velocities and temperature gradients, as shown in Fig. 7 [137]. It is elucidated that the predominant microstructure features were B2 proeutectic dendrites structures delineated by lamellar or rod-like B2/A2 eutectic structures, which were frequently fragmented, providing numerous effective nucleation sites to promote the formation of equiaxed grains. A similar fine-grained structure was also observed in the additive manufactured HEA composite, such as the CoCrFeMnNi HEA matrix composite reinforced by nano-sized TiN particles [224–226]. The microstructure was isotropic and was remarkably refined with 90% of the grains having sizes less than 2  $\mu\text{m}$ , whereas without TiN anisotropic coarse grains and a strong texture intensity were observed. Another noticeable research result with regard to the fabrication of HEA matrix composites was the LMD-produced CoCrFeMnNi specimens with different WC concentrations [227]. All specimens showed compact equiaxed grain microstructures without any obvious pores or cracks, and the average grain size decreased significantly with the addition of WC. It is confirmed that the formation of Cr<sub>23</sub>C<sub>6</sub> precipitates led to the refinement of the microstructure and also hampered the propagation of slip bands.

### 3.4. Element distribution

Most HEAs contain more than four constituent elements, where the phases formation after AM process is highly dependent on the homogeneity of these elements.

Haase et al. [196] performed LMD on CoCrFeMnNi HEA from elemental powder blends and the energy dispersive x-ray detector (EDX) element mappings showed that, compared with the same alloy system after conventional casting process where macro segregation usually occurred [291], the distribution of the five constituent elements was significantly more uniform except for the oxides. For SLM-built CoCrFeMnNi HEA parts, the electron probe micro analyzer (EPMA) results confirmed that the Co, Cr, Fe, and Ni elements were uniformly distributed in the whole molten pool, while local enrichment of Mn was observed at the boundary of the molten pool and the specimen surface [185]. It is revealed that the formation of dislocation cells contributed to more significant elemental segregation at the cell walls [186]. Chen et al. [174] fabricated CoCrFeMnNi HEA by SLM in-situ alloying from blends of CoCrFeNi pre-alloyed powder and Mn elemental powder, the energy dispersive spectrum (EDS) mapping highlighted that at a lower VED of 120.4 J·mm<sup>-3</sup>, segregation of CoCrFeNi and blanks of Mn occurred extensively, which changed into uniform distribution as the VED increased to 259.3 J·mm<sup>-3</sup>. By contrast, both Mn and Ni segregation could be detected at the cell networks in C-doped CoCrFeMnNi HEA [217], ascribed to the interstitial carbon as well as the CoCrFe-MnNi solid-liquid two-phase zone arising from the intermediate solidification rate. Similar results have also been observed in EBM-fabricated CoCrFeMnNi HEA via pre-alloyed powders, where Mn and Ni segregated into the interdendrites, while Co, Cr and Fe segregated into the dendrites [213]. EBSD scan

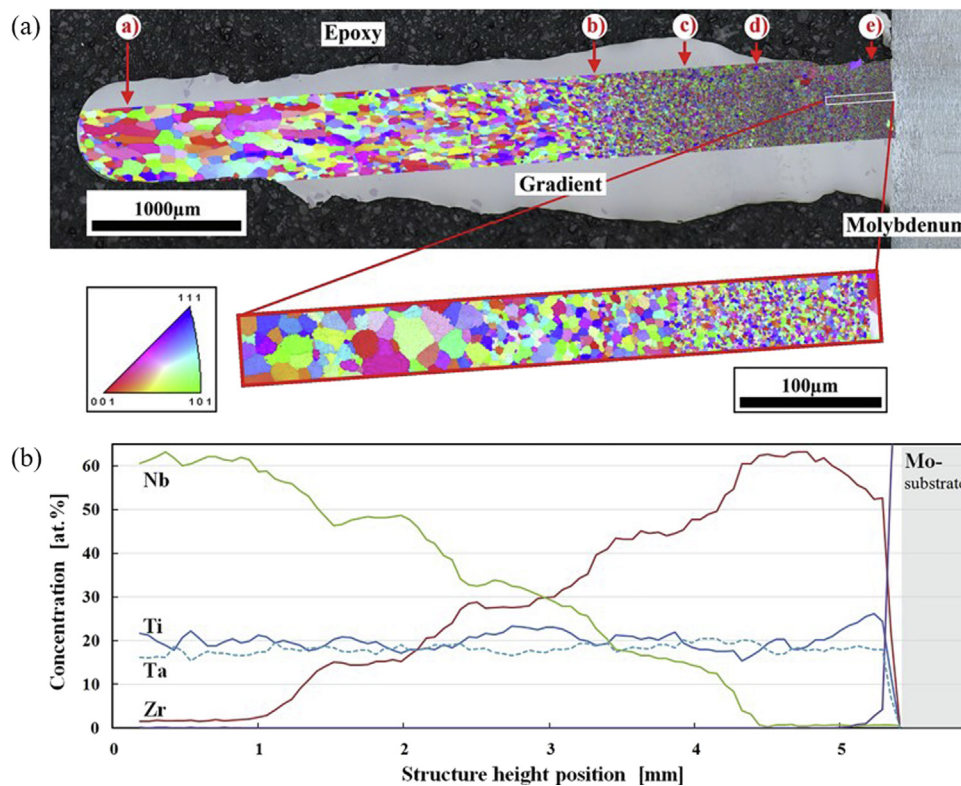


**Fig. 6.** (a) BSE image with overlapping grain orientation map along the cross section and (b) the composition gradient of LMD-built NbTaTiZr wall structure. Adapted with permission [95]. Copyright 2018 The Authors.

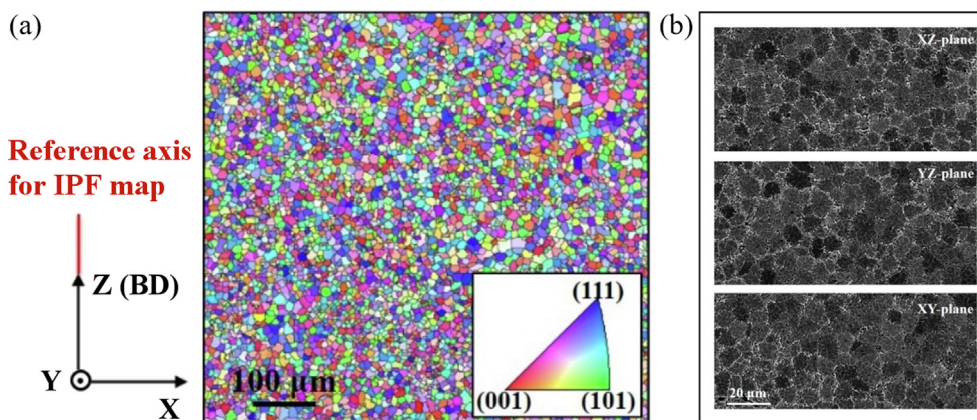


**Fig. 7.** (a) EBSD-IPF map of the XZ-plane and (b) BSE images of XZ-, YZ- and XY-planes of LMD-built AlCoCrFeNiTi<sub>0.5</sub> HEA. Adapted with permission [137]. Copyright 2019 The Authors.

and EDS mapping of the SLM-built dual-phase Al<sub>0.5</sub>CoCrFeNi HEA are shown in Fig. 8(a-c) [106]. It can be found that Fe and Co were enriched in the dendritic regions and partitioned into the parent FCC phase. The Cr concentration remained mostly uniform throughout the whole mapping area, while the remaining elements Ni, Si and Al co-segregated into the interdendritic regions, forming the B2/BCC phase. The APT results in Fig. 8(d-f) show the quantitative chemical composition of different phases within this Al<sub>0.5</sub>-CoCrFeNi HEA. Transition elements, Co, Cr, Fe and Ni, were found to be approximately equiatomicly concentrated in the primary FCC phase, while the coherent ordered B2 and disordered BCC phase were rich in AlNi and Cr elements, respectively.

It is pointed out that the chemical homogeneity of produced HEA parts is significantly dependent on the energy input and the

resultant molten pool size during the AM process [47]. On the one hand, insufficient energy input leads to inhomogeneous elements distribution attributed to partially melted powders with high melting points. On the other hand, the small molten pool size prevents the elements from sufficient flowing and mixing during the solidification process. Moreover, the severity of the segregation is strongly dependent on the cooling rate of the additive manufactured structure, which in turn is also a function of the process parameters. A higher VED leads to a lower cooling rate and as a result to more remarkable elemental segregation. The influence of thermal properties, melting point and vapor pressure of the mixed elements on the deposition process and final chemical composition of the additive manufactured HEAs samples has also been discussed [54]. In general, the lower an element's melting point is,

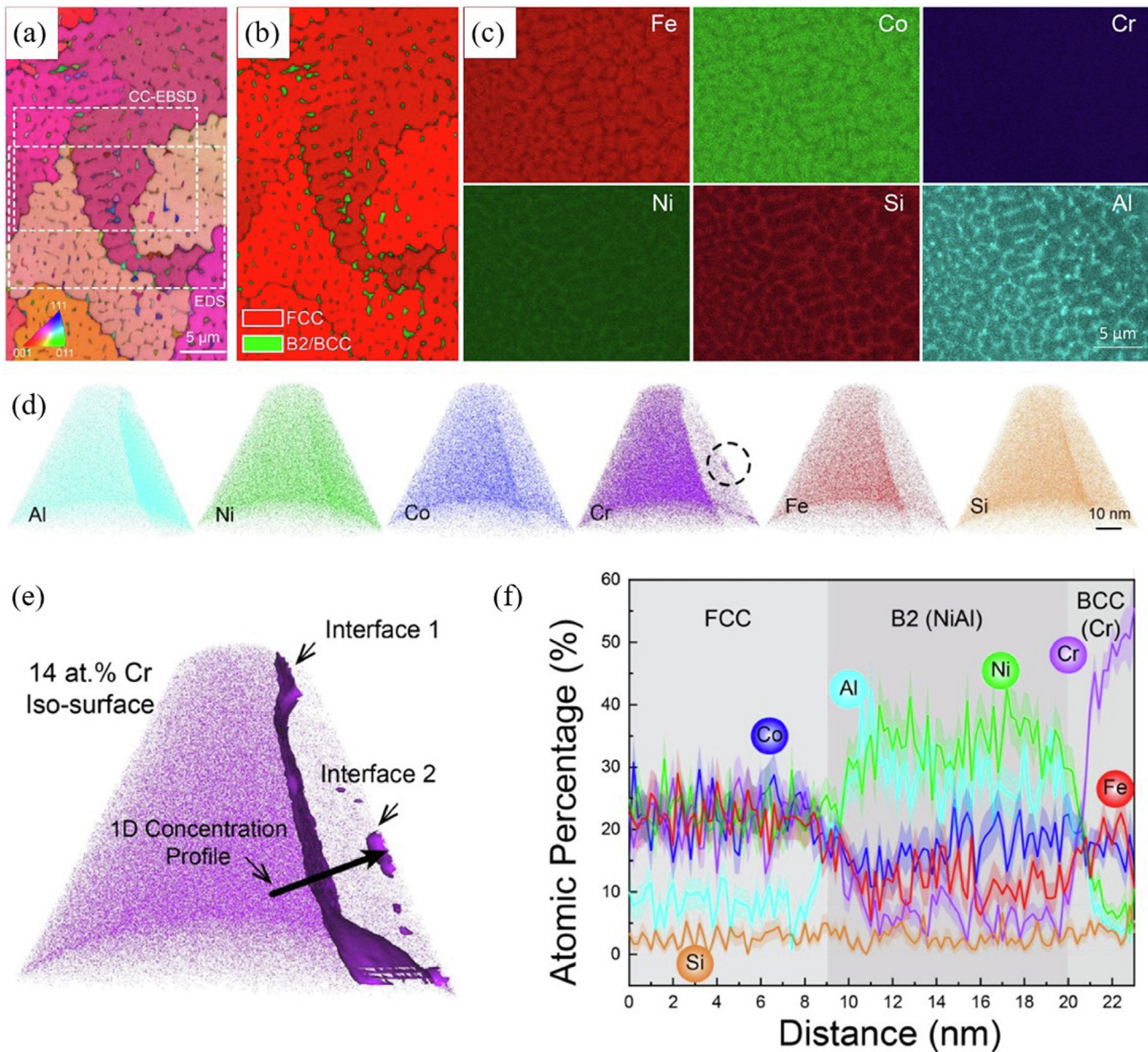


**Fig. 8.** (a) EBSD IPF superimposed by image quality map of SLMed  $\text{Al}_{0.5}\text{CoCrFeNi}$  HEA. (b) Phase map superimposed by image quality map. (c) EDS mapping of all elements within the specified area in (a). Reconstructed APT volumes showing (d) elemental distribution, (e) Iso-surface of 14 at.% Cr and (f) 1D concentration profiles along the line plotted in (e). Adapted with permission [106]. Copyright 2020 Elsevier.

the higher its concentration in the manufactured samples will be. In this sense, it is suggested that in order to control the composition in large structures, the melt pool size and temperature should be measured and a loop control should be established during the AM process. Some researchers proposed that by adding excessive amount of light metal elements to the initial powders mixture to solve the problem of possible evaporation of light metals during the AM process [160]. Recently, Zhang et al. [265,266] carried out systematic studies on SLM-built MoNbTaW HEA, focusing on the effects of the melting point, liquid density, average particle size and laser absorptivity. It is elucidated that the elements (Mo, Nb) with lower melting point and lower liquid density exhibited a negative deviation of the molar ratio ( $\leq 5\%$ ) in the produced HEAs. While both the average particle size and laser energy absorptivity had a similar changing trend as well as a certain casual relationship. However, the observed composition deviation had no effect on the phase constituent of the produced HEAs.

### 3.5. Phase constituent

The phase constituents confirmed by the authors of each investigation on AM HEAs are listed in Table 1. It has been demonstrated that a better balance of the performance of HEAs can be reached for the microstructure composed of a disordered solid solution phase and an ordered multi-component precipitation phase [62].

By varying the percentage of Al in the  $\text{AlCoCrFeNi}$  HEA, three completely different microstructures with LMD technique were obtained in [34,113,114]. With the increase of Al content, the microstructure changed from initial FCC to FCC/BCC then to completely BCC phase. There is a strong similarity between the single-phase FCC and BCC HEAs prepared by arc-melting and LMD, however, the dual-phase FCC/BCC structure was significantly different, arising from the different solidification rates and thermal gradients in the molten pool of these two manufacturing methods. Interestingly, the LMDed dual-phase FCC/BCC microstructure

showed an equiaxed grain morphology along the building direction rather than a typical columnar structure, ascribed to the lower thermal conductivity of the dual-phase HEAs. The  $\text{Al}_x\text{CoCrFeNi}$  HEA produced by SLM with varying Al contents also resulted in different phase constituents [118], that is, single-phase FCC structure for  $x = 0.3$  and dual-phase B2/FCC microstructure for  $x = 0.7$ . The gradually increased feed changing from  $x = 0.3$  to  $x = 0.7$  led to the formation of a transition zone with an intermediate composition and complex microstructure including elongated FCC grains, B2 precipitation along the grain boundaries as well as rudimentary lamellae of FCC and B2. Recently, Borkar et al. [122] carried out a systematic study on the role of Co and Cr in LMD-built  $\text{AlCo}_x\text{Cr}_{1-x}\text{FeNi}$ . The results highlighted that the  $\text{AlCoFeNi}$  ( $x = 1$ ) HEA exhibited equiaxed B2 grains, presenting an early stage of phase separation into Ni-Al enriched and Fe-Co enriched zones within the B2 phase; while for  $x = 0$ , the  $\text{AlCrFeNi}$  HEA exhibited grains with pronounced spinodal decomposition, leading to a BCC + B2 microstructure. While Zhao et al. [126] reported different phase constituents for the same HEA system produced by LMD. In their work, Co element was found to promote the phase transformation from BCC to FCC, where the volume fraction of FCC phase increased from 51.4% to 74.6% with the Co content increased from 36.2 at.% to 40.8 at.%, accompanied by the formation of a large amount of fine needle-like BCC phase in the FCC matrix. Ordered B2 phase distributed between the disordered A2 phase in  $\text{AlCoCrFeNi}$  HEA produced by SLM was reported in [112], which is different from the conventional cast alloy with A2 and FCC phases. It was shown that the formation of B2 phase is the dominant process at higher cooling rates and then is substituted by the formation of A2 phase at lower cooling rates, which results in the successive formation of different phases and thus a specific  $\{100\}_{\text{A2}}\parallel\{100\}_{\text{B2}}$  orientation relationship. Shiratori et al. [129] compared the  $\text{AlCoCrFeNi}$  HEA specimens manufactured by EBM with conventional cast samples. Both were mainly composed of a nano-lamellar mixture of disordered BCC and ordered B2 phases, while the FCC phase was only precipitated at the grain boundaries of the B2/BCC mixture phase in the EBM samples, as shown in Fig. 9. It is believed that preheating during the EBM process contributed to the formation of the FCC structure via a solid-state phase transformation due to the long-

term exposure at a sufficiently high temperature. The fraction of the FCC phase at the specimen bottom (29.7%) was significantly higher than that at the top (7.1%) due to the different exposure time at high temperature (Fig. 9).

A slightly modified  $\text{AlCrCuFeNi}$  HEAs system was studied by Brokar et al. [5], followed by Luo et al. [150-153] and Choudhuri et al. [154]. A single deposition of  $\text{Al}_x\text{CrCuFeNi}_2$  ( $0 < x < 1.5$ ) alloy was fabricated by LMD in [5], which enabled a detailed evaluation of the microstructure transition from predominately FCC structure, to FCC/L1<sub>2</sub>, mixed FCC/L1<sub>2</sub> + BCC/B2 and finally to predominantly BCC/B2 structure with increasing the Al content from 0 to 1.5 (molar fraction) gradually. It has been elucidated that the increase of Al tends to destabilize the close-packed FCC structure through an increasing lattice constant of the alloy. With a lower atomic packing density than FCC and HCP structures, BCC structures can more easily accommodate the large lattice distortions introduced by larger solute atoms like Al. Besides, it was reported by Tang et al. [292] that the electronic configuration of Al ( $[\text{Ne}]3s^23p^1$ ) may cause this element to behave as both metals and non-metals. As a consequence, Al can introduce some covalent bonds and form compounds with ordered BCC structure in the vicinity of transition elements such as Ni and Co with partially filled d-shell. In [154], a microstructure transition from FCC to BCC was found with the change in Al from  $x = 0.8$  to  $x = 1.0$  in the LMD-built  $\text{Al}_x\text{CrCuFeNi}_2$  HEA. The dark-field TEM image in Fig. 10(a) shows the primary solidification FCC phase with L1<sub>2</sub> precipitates and the secondary solidification phase of B2 plates along with the wetting layer of L1<sub>2</sub> around B2 plates in  $x = 0.8$  structure. Inter-dendritic region consisting of a mixture of ordered B2 and disordered BCC phase are shown in Fig. 10(b). The scanning transmission electron microscopy (STEM) and EDS compositional analyses in Fig. 10(c) show that in the inter-dendritic region, the ordered B2 structure was enriched in Al while the disordered BCC region is Cr enriched, indicating a post-solidification solid-state spinodal transformation of BCC to B2 (Al, Ni enriched) and BCC (Cr, Fe enriched). In  $x = 1.0$  alloy, the primary solidification phase changes to ordered B2 and disordered BCC phases with some Cu-rich precipitates, as shown in Fig. 10(d). In this alloy, the secondary solidification FCC phase is formed as an intergranular structure composed of L1<sub>2</sub>

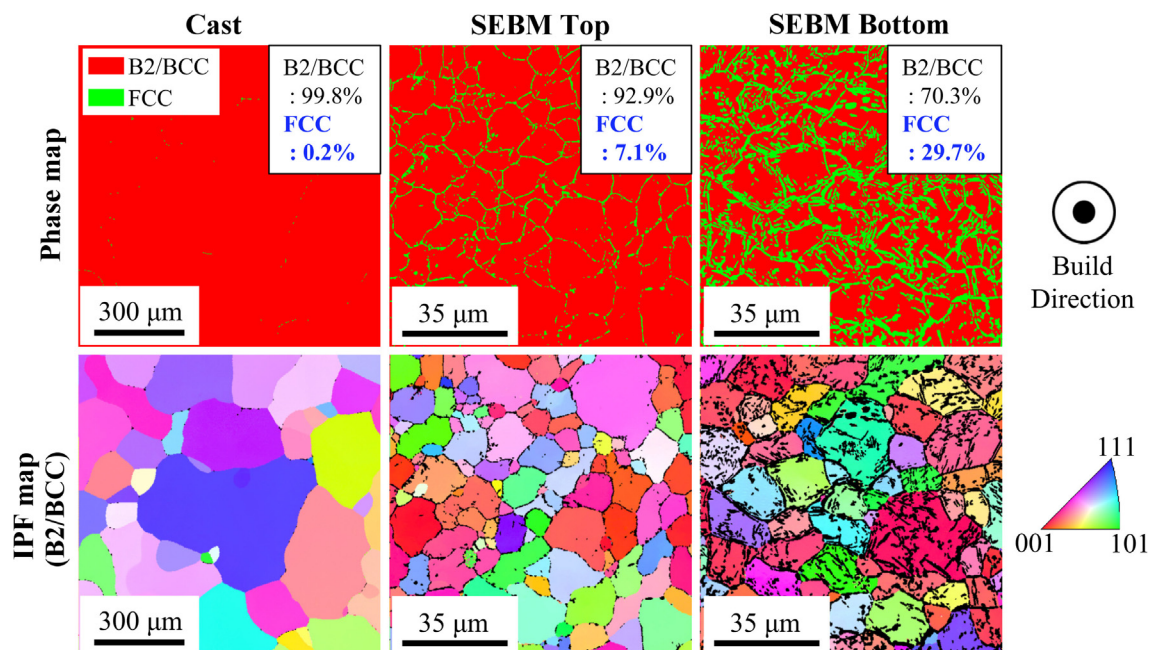
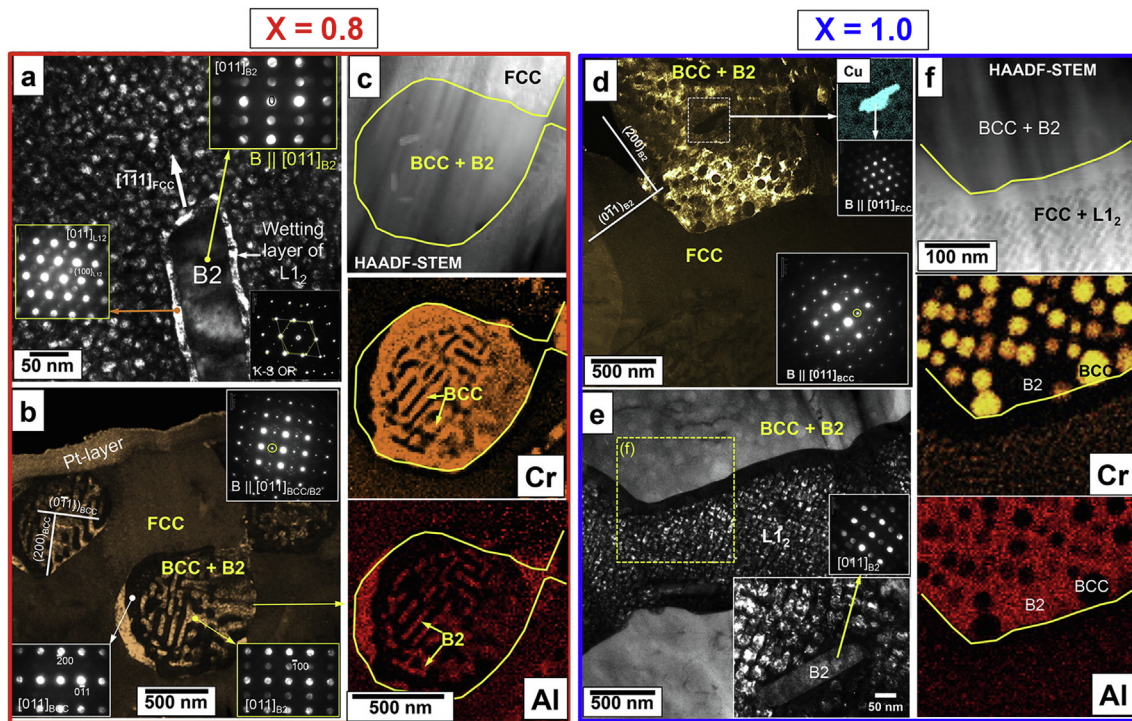


Fig. 9. Phase maps and IPF maps of the cast and the EBM  $\text{AlCoCrFeNi}$  HEAs. Reproduced with permission [129]. Copyright 2016 Elsevier.



**Fig. 10.** Drak-field TEM results of  $\text{Al}_x\text{CrCuFeNi}_2$  ( $x = 0.8$ ) showing (a) primary FCC and secondary BCC phases, (b) ordered B2 and disordered BCC interdendritic pockets and (c) the corresponding STEM-EDS maps of Al and Cr. Drak-field TEM results for  $x = 1$  showing (d) primary BCC and B2 regions alongside interdentritic FCC phase, (e) primary B2 and BCC matrix and (f) STEM-EDS maps of Al and Cr from the marked region in (e). Reproduced with permission [154]. Copyright 2016 Elsevier.

fine-scale precipitation (Fig. 10(e)). Similar to  $x = 0.8$ , the B2 ordered region is Al-enriched while the BCC disordered structure is enriched in Cr (Fig. 10(f)). In addition, FCC and BCC dual-phase HEAs were designed and fabricated based on the BCC  $\text{AlCrCuFeNi}_x$  system [152], firstly achieving the production of dual-phase HEAs by SLM with a minimum Ni content of  $x = 2$ , meanwhile, the deformation induced nano-twins, stacking faults and strain-activated B2-to-FCC phase transitions were found in the BCC phase.

In LMDed  $\text{CoCrFeMnNi}$  [210], it was observed that the fine second BCC phase distributed at the grain boundaries of the FCC matrix, and the morphology of the BCC phase was dominated by the wetting phase transformation of the grain boundary. An in-situ strengthening of  $\text{CoCrFeMnNi}$  HEA with Al addition through LMD was reported in Gao et al.' work [104], the phases changed from single FCC to duplex FCC and BCC with Al content ranging from 5 at.% to 8 at.%. Another interesting work about this  $\text{CoCrFeMnNi}$  HEA was the formation of a localized amorphization structure with nano TiN addition owing to the remelting laser scanning strategy [225]. Recently, a new metastable  $\text{Co}_{20}\text{Cr}_{15}\text{Fe}_{40}\text{Mn}_{20}\text{Si}_5$  HEA was fabricated with SLM, which showed a stabilized  $\epsilon$ -HCP dominated ( $\sim 72\%$ ) dual phase microstructure with 28% retained  $\gamma$ -FCC phase, owing to the fact that simultaneous addition of Cr and Si into Fe-Mn-rich alloy reduces the driving force for the FCC  $\rightarrow$  HCP phase transformation [228]. The deformation-induced FCC to HCP transformation was also found in SLM-printed  $\text{CoCrFeMnNi}$  HEA with the  $\langle -110 \rangle_{\text{FCC}} // \langle 1120 \rangle_{\text{HCP}}$  and  $\{111\}_{\text{FCC}} // \{0001\}_{\text{HCP}}$  orientation relationship [186], which has not been reported in other additive manufactured  $\text{CoCrFeMnNi}$  HEA.

During the LMD of compositionally graded  $\text{NbTaTiZr}$  refractory HEA, it was found that a high Zr concentration favored the formation of dual BCC phases, where the second Ta enriched BCC phase was pinned on the grain boundaries of the Zr enriched BCC matrix, and the volume fraction of the former increased with increasing Zr

concentration [95]. For LMD-fabricated refractory  $\text{MoNbTaW}$  HEA with varying W contents, it was found that the W concentration had no influence on the formation of a single BCC solid solution of this HEA [268]. A recent study by Moorehead et al. [267] applied the calculation of phase diagram (CALPHAD) modeling to map the composition space of LMD-printed  $\text{MoNbTaW}$  alloy at  $300^\circ\text{C}$ , predicting that nearly all printed compositions are composed of a single disordered BCC crystal structure. From the quaternary phase diagram as shown in Fig. 11, it can be noticed that Nb played a crit-

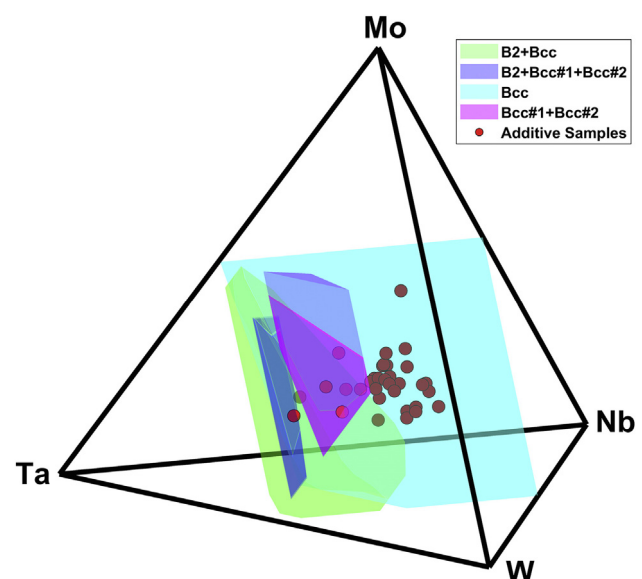


**Fig. 11.** Quaternary phase diagram of  $\text{MoNbTaW}$  system at  $300^\circ\text{C}$  as calculated by CALPHAD. Reproduced with permission [267]. Copyright 2019 The Authors.

ical role in stabilizing the single disordered BCC phase, while Ta destabilized this BCC phase, resulting in the phase separation and the formation of an ordered BCC secondary phase.

### 3.6. Precipitations

The thin-walled  $\text{Al}_x\text{CoCrFeNi}$  samples manufactured by LMD under different laser scanning speeds decomposed into dendrites and interdendrites, both of which contained Fe-Cr enriched BCC precipitates in the Al-Ni enriched B2 matrix [51]. The morphology of the BCC precipitates changed from plate-like and cuboid to elliptic and subspherical. For EBM-processed CoCrFeNiTi-based HEA, it was reported that needle-like  $\text{Ni}_3\text{Ti}$  intermetallic precipitates with basket-weave morphology distributed uniformly in the matrix, differing greatly from the casting specimens, as shown in Fig. 12 [65].

The Cr-C enriched nano-sized precipitates were dispersed along grain boundaries, cellular and columnar sub-grain boundaries in the SLM-produced C-containing CoCrFeNi HEA [248]. These precipitates were entirely spherical with sizes in the range of 10 to 100 nm. 7% volume fraction of  $\text{Mn}_2\text{O}_3$  and MnO particles were found in SLM in-situ alloyed CoCrFeMnNi HEA, most likely originating from the powder feedstock and the printing atmosphere [187], secondary particles of Mn oxides were also detected in [175,176,183,186,192,193,215,219]. For SLM-printed C-containing CoCrFeMnNi HEA [215], nano-sized precipitates, with a nearly spherical shape, distributed along the cellular structure boundaries. The electron energy loss spectroscopy (EELS) mapping indicated that the precipitates were a mixture of Cr enriched carbide and Mn enriched oxide and sulfide, with sizes ranging from 30 to 70 nm. For another nano-TiC particles reinforced CoCrFeMnNi HEA matrix composites [222], it was found that the SLM-synthesized pure HEA and its composites all had uniformly distributed precipitates, but with different compositions and sizes, as shown in Fig. 13(a-e). The precipitates formed in pure CoCrFeMnNi were  $\text{Mn}_2\text{O}_3$  oxides, while those of the composites were  $\text{TiC}_{1-x}$  type carbides, and the precipitate size in pure HEA

(~250 nm) was much larger than that in latter (53.6–105.4 nm). Besides, it can also be found that the size and volume fraction of the precipitates in the HEA composites were strongly affected by the applied VED, as shown in Fig. 13(f). That is, both the average diameter and volume fraction of the precipitates showed an increased trend with the increase of VED. Fig. 13(g) schematically illustrated the formation mechanism of the precipitates under different laser processing parameters. When the VED was set to a low value, corresponding to a high laser scanning speed, the precipitates showed an intercrystalline distribution and were ultrafine in size (Fig. 13(b)). This was due to the relatively short duration of molten pool solidification under this condition, during which the precipitates first nucleated and subsequently the HEA liquid crystallized to form sub-grain boundaries. As the solidification front advanced, precipitates accumulated at the solidified sub-grain boundaries. In addition, the kinetic constraints imposed by the ultrahigh cooling rate might also hinder the precipitation of TiC, resulting in the existence of solute atomic C and Ti in the matrix. With the increase of VED, both intragranular and intergranular precipitates can be observed (Fig. 13(c-e)). Higher VED increased the duration of molten pool to be solidified, allowing more time for the dissolved atomic C and Ti to combine and eventually precipitate inside the substructures. Furthermore, nano-sized Cu enriched precipitates were observed in AlCrCuFeNi HEA fabricated by SLM [149], which exhibited chain-like shapes at HAGBs while they had granular shapes at LAGBs. The difference in the degree of segregation of Cu at the grain boundaries was caused by the larger driving force for the segregation at HAGBs due to their larger lattice distortion. In another work by Luo et al. [152], a high density of Cr-rich nano-sized precipitates was confirmed in the ordered BCC phases, which made the BCC phase distorted severely during tension process, thereby resulting in the formation of deformation-induced nano-twins and stacking faults. Through the LMD of CoCrFeMnNi HEA-based composites with the WC addition, it was found that the WC phases completely dissolved during LMD process, and  $\text{M}_{23}\text{C}_6$  precipitates formed

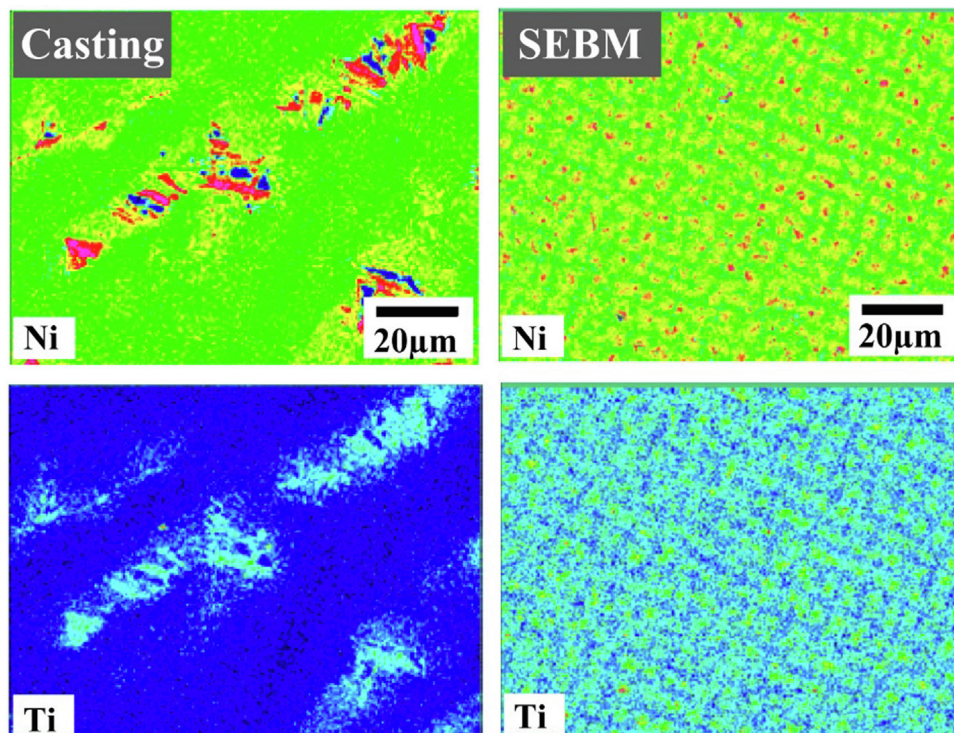
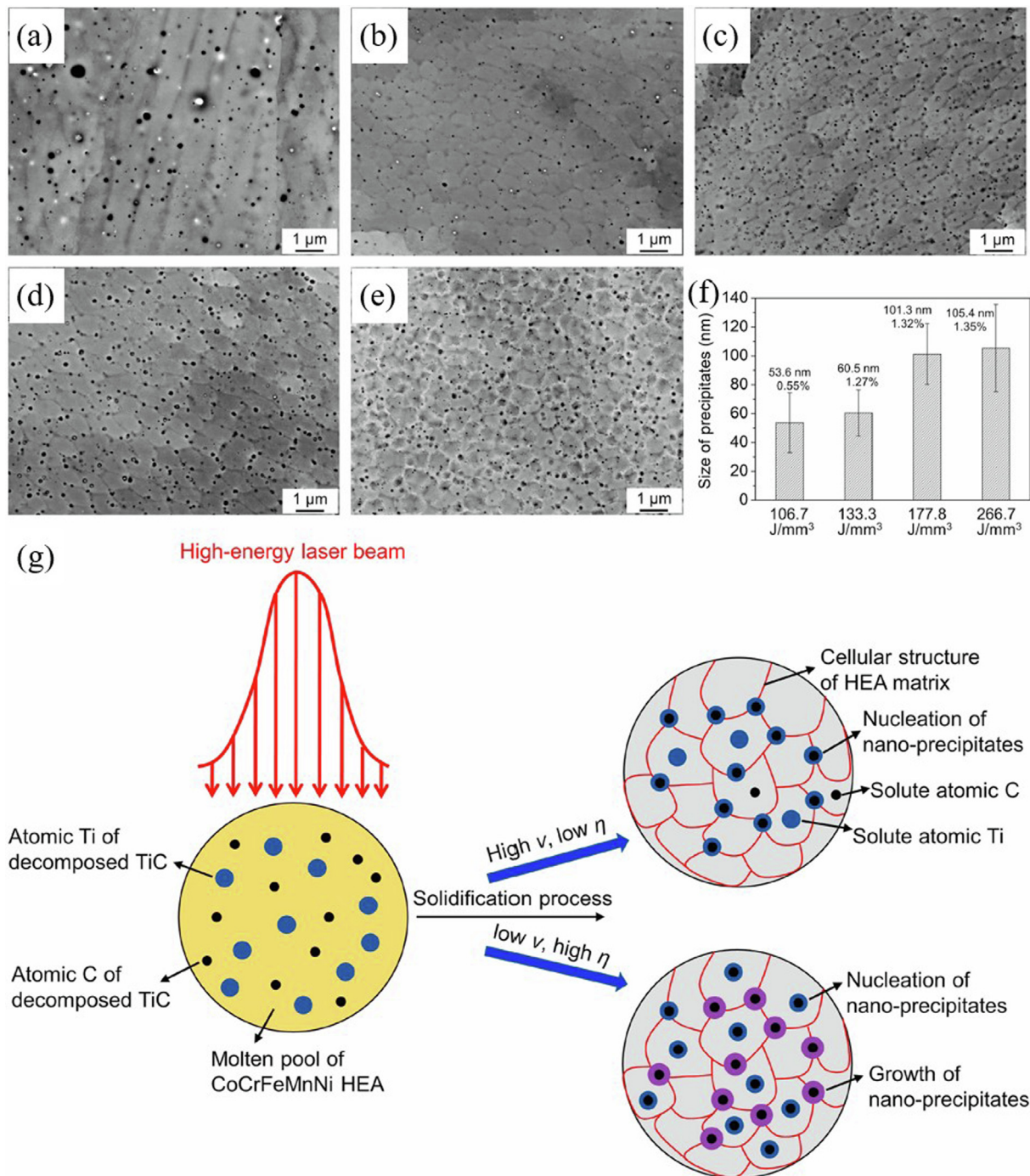


Fig. 12. EPMA elemental mappings of Ni and Ti of casting and EBM CoCrFeNiTi HEA specimens. Adapted with permission [65]. Copyright 2016 Elsevier.



**Fig. 13.** Microstructure of the SLM-built pure CoCrFeMnNi HEA (a) and its TiC particles reinforced composites fabricated at varying VED: (b) 106.7 J/mm<sup>3</sup>, (c) 133.3 J/mm<sup>3</sup>, (d) 177.8 J/mm<sup>3</sup>, (e) 266.7 J/mm<sup>3</sup>. (f) Size and volume fraction of the precipitates in the HEA composites under different VED. (g) Schematic illustration of the formation mechanism of precipitates under different laser processing conditions. Adapted with permission [222]. Copyright 2021 Elsevier.

instead [227]. Such precipitates may function as heterogeneous nucleation sites during solidification, resulting in the finer grain size distributions.

### 3.7. Post-treatment effect

In general, heat treatment, mainly including hot isostatic pressing (HIP), solution treatment and annealing, can be applied for the densification of AM parts through reducing the remaining porosity [185]. However, it also has two negative effects, namely coarsening the microstructure and forming the  $\sigma$  phase [116], which will

always deteriorate the performance of alloys with a high Cr content [49].

HIP, which has been widely used for casting alloys, could help collapse the possible shrinkage defects which occurred during the AM process [49]. Joseph et al. [113] carried out the first work studying the effect of HIP treatment on the LMD-built Al<sub>x</sub>CoCrFeNi alloy. It turned out that the amounts of large pores with a diameter > 5  $\mu$ m decreased and therefore the density of the as-deposited HEAs increased with the coarsening of microstructure and homogenization of the elemental distribution after HIP processing. Moreover, the authors proposed a critical cooling rate of 1 K·s<sup>-1</sup> to inhibit the  $\sigma$  phase formation. Wang et al. [53] studied the microstructure

and phase constitute of the as-deposited AlCoCrFeNi HEA as well as the samples aged at temperatures of 600 °C, 800 °C, 1000 °C and 1200 °C for 168 h. As the back-scattered scanning electron microscope (SEM) images shown in Fig. 14, the as-deposited and the

600 °C aged sample exhibited a single-phase B2 solid solution structure; while after ageing at 800 °C, 1000 °C and 1200 °C, the microstructures changed into intercrystallite needle-like, plate-like and wall-shaped FCC precipitates at grain boundaries,

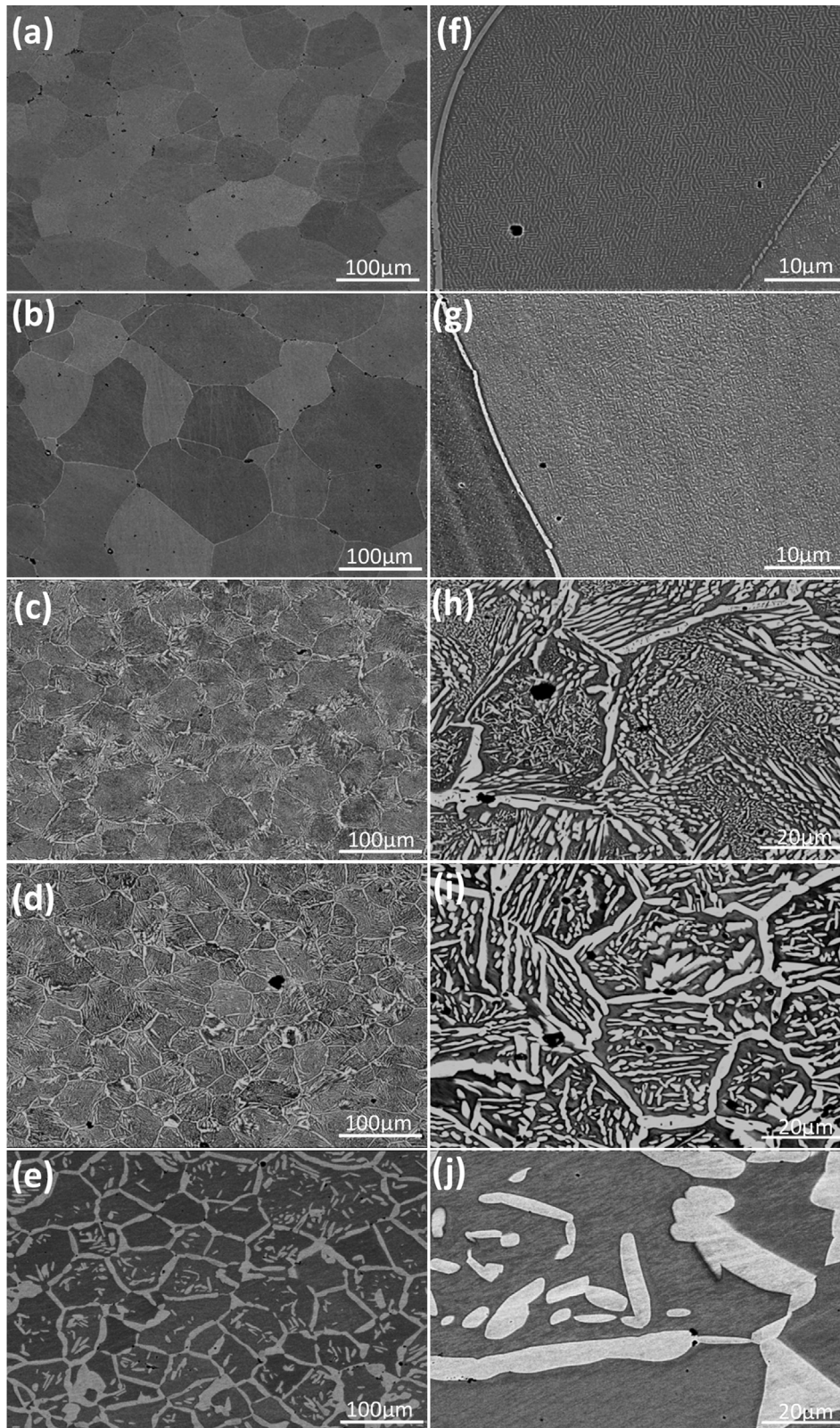


**Fig. 14.** Back-scattered SEM images of AlCoCrFeNi HEA samples obtained with different heat treatment conditions: (a), (b), (c), (d), (e) for as-deposited, aged for 168 h at 600 °C, 800 °C, 1000 °C and 1200 °C, respectively. (f), (g), (h), (i), (j) Higher magnifications of (a), (b), (c), (d), (e). Reproduced with permission [53]. Copyright 2016 Elsevier.

respectively, with Cr and Fe segregated into the FCC phase. Moreover, a necklace of precipitates composing of Al enriched B2 and Cr enriched  $\sigma$  phase was found along grain boundaries in the case of heat-treated  $\text{Al}_{0.3}\text{CoCrFeNi}$  HEA sample fabricated by LMD [119]. The dendrite-like features of SLM-printed  $\text{AlCoCrFeNi}$  samples exhibited a distinct chemical fluctuation at the nanometer scale for Cr during the heat treatment process. It was suggested that the spinodal decomposition results in further segregation of Cr-rich regions [101]. For WAAM-produced  $\text{AlCoCrFeNi}$  HEA, Shen et al. [71] found that a large number of Cr-rich  $\sigma$  phases precipitated in the B2 matrix and nano-sized ordered FCC ( $L_{12}$ ) phase precipitated in the FCC matrix under annealing at 600 °C. With the annealing temperature up to 800 °C,  $\sigma$  phase coarsened and the  $L_{12}$  phase transformed into the rod-like B2 phase precipitated in the FCC matrix. As the annealing temperature further increased to 1000 °C,  $\sigma$  phase dissolved in B2 matrix and the rod-like B2 precipitations were significantly coarsened. The evolution of the microstructures under different heat treatment conditions would greatly affect the corresponding strengthening mechanisms, such as precipitation strengthening and solid solution strengthening, and consequent mechanical response.

Annealing the LMD-deposited  $\text{CoCrFeMnNi}$  samples produced a chemically homogeneous and recrystallized microstructure, with the presence of high-density annealing twins [197]. The high density of dislocation and vacancy typically observed in the as-built microstructure can contribute to higher maximum orientation spread values, while the distribution of maximum orientation spread became much smaller and narrower for the annealed microstructure, indicating a complete recovery and recrystallization. Li et al. [185] discussed the homogenization of the SLM-printed  $\text{CoCrFeMnNi}$  HEA by the annealing treatment above 900 °C. It is observed that the microstructures were chemically homogenized and the dense dislocation substructures were relaxed, while a Cr enriched  $\sigma$  phase was typically formed after a long annealing time. Zhu et al. [170] reported that after heat treatment at 900 °C for 1 h in argon followed by furnace cooling, the cellular structure in the as-deposited  $\text{CoCrFeMnNi}$  HEAs almost disappeared, as the remaining lower dislocation density implied the thermodynamically metastable characteristics of these cellular structures. It is illustrated by Li et al. [185] that the heat treatment leads to no alteration in the texture of SLM-printed  $\text{CoCrFeMnNi}$  sample, as the orientation of the grains in the as-printed sample remained unchanged with  $\langle 001 \rangle$  parallel to the build direction after HIP. It is also found that post-heat treatment could eliminate the Mn segregation at the boundary of the molten pool and the specimen surface, contributing to more homogeneous elemental distribution. The microstructure evolution of the as-built and heat-treated LMDed  $\text{CoCrFeMnNi}$  HEA is shown in Fig. 15 [198]. Apart from the coarsening of the structure with increasing heat treatment temperature, the formation of twins can be seen in the case of the annealed sample at 1100 °C, implying the release of internal residual stress at high annealing temperature. Unlike the SLMed sample in [185], the post-heat treatment in [198] changed the dominant texture of the as-deposited specimen. The as-built sample showed a random distribution of grains with  $\langle 001 \rangle$  and  $\langle 101 \rangle$  parallel to the building direction. Heat treatment at 1100 °C altered the texture by strengthening the  $\langle 111 \rangle$  and  $\langle 101 \rangle$  orientations while weakening the  $\langle 001 \rangle$  orientation.

For other HEA systems, such as in SLM-built  $\text{AlCoCuFeNi}$  HEA [142], heat treatment caused the precipitation of Cu-rich FCC phase from the Al- and Ni-rich metastable BCC matrix, thereby leading to the formation of a dual-phase structure in the heat-treated samples, and an increased volume fraction of the FCC phase can be obtained when applying a higher heat treatment temperature, a similar result was also found in  $\text{AlCrFe}_2\text{Ni}_2$  HEA [153]. For the SLM-fabricated C-containing  $\text{CoCrFeNi}$  HEA, nano-sized  $\text{Cr}_{23}\text{C}_6$ -

type carbides precipitated after the annealing treatment, which mainly distributed along the grain boundaries and cell structures [246]. In the SLM-printed N-doped  $\text{CoCrFeNi}$  HEA [236], hierarchically heterogeneous microstructure consisting of bimodal grain structures, low angle boundaries and dislocation networks was observed after annealing treatment. What is remarkable in this work is the uniform distribution of N atoms, dissolving into the FCC matrix without any nano-clustering. For EBM-built  $\text{AlCr-MoNbTa}$  HEA [160], the microstructural homogenization was improved after the heat treatment conducted in evacuated ampules at different temperatures. However, the heat treatment showed no effect on the residual porosity for this additive manufactured HEA.

An interesting pioneer work on the post machinability of SLM-printed  $\text{CoCrFeMnNi}$  HEA was discussed by Guo et al. [188]. In their study, different machining conditions including mechanical, thermal and electro-chemical processing methods, were applied to the  $\text{CoCrFeNiMn}$  HEA to quantitatively evaluate the surface morphology and subsurface quality. Their research concluded that practically applicable surface quality and dimensional accuracy could be obtained through appropriate process combination. Recently, laser shock peening (LSP) has also been applied to improve the microstructure on the surface layer of LMD-fabricated  $\text{CoCrFeMnNi}$  HEA [59,202]. The results highlighted that the pores in the as-built HEA surface layer were closed due to the LSP-induced severe plastic deformation, and a gradient microstructure containing ultra-fine grains, mechanical twins and dislocations along the depth direction has developed after LSP.

In addition to microstructural modification, post-treatment also plays an important role in releasing the residual stresses generated by AM processes. Annealing, one of the most common post-processing methods after AM, can improve the reliability of in-service parts by effectively releasing residual stresses [233,274,293,294]. Lin et al. [233] investigated the trend by which residual stresses in SLM-printed  $\text{CoCrFeNi}$  HEA varied with different annealing temperatures. It was found that the residual tensile stress gradually decreased with increasing annealing temperature, which was almost completely eliminated when annealed at 1300 °C due to the decomposition of dislocation networks. In another work by Lin et al. [234], it is reported that the residual stress in the cold-deformed  $\text{CoCrFeNi}$  HEA was higher than that in the as-printed samples due to the higher dislocation densities, but after annealing, the residual stress decreased gradually and remained constant above 900 °C annealing temperature.

#### 4. Mechanical properties of additive manufactured HEAs

In general, the mechanical strength of the additive manufactured parts depends on the density and the microstructure. Comparing to the parts produced by conventional routes (e.g. casting), the finer microstructure of AM produced parts contributes to superior mechanical properties than their counterparts [44]. Up to now, mechanical properties of AM HEAs have been studied in terms of hardness, tensile and compressive testing, etc. The post-treatment, such as HIP, solution treatment and ageing, can further improve the performance by eliminating the existing metallurgical defects and residual stress in the additive manufactured metallic materials [60,295].

##### 4.1. Microhardness

A summary of hardness, tensile and compressive properties of additive manufactured HEAs is listed in Table S1 (see appendix A). Fig. 16 summarizes the microhardness data of different HEAs systems processed by different AM techniques. It can be seen that

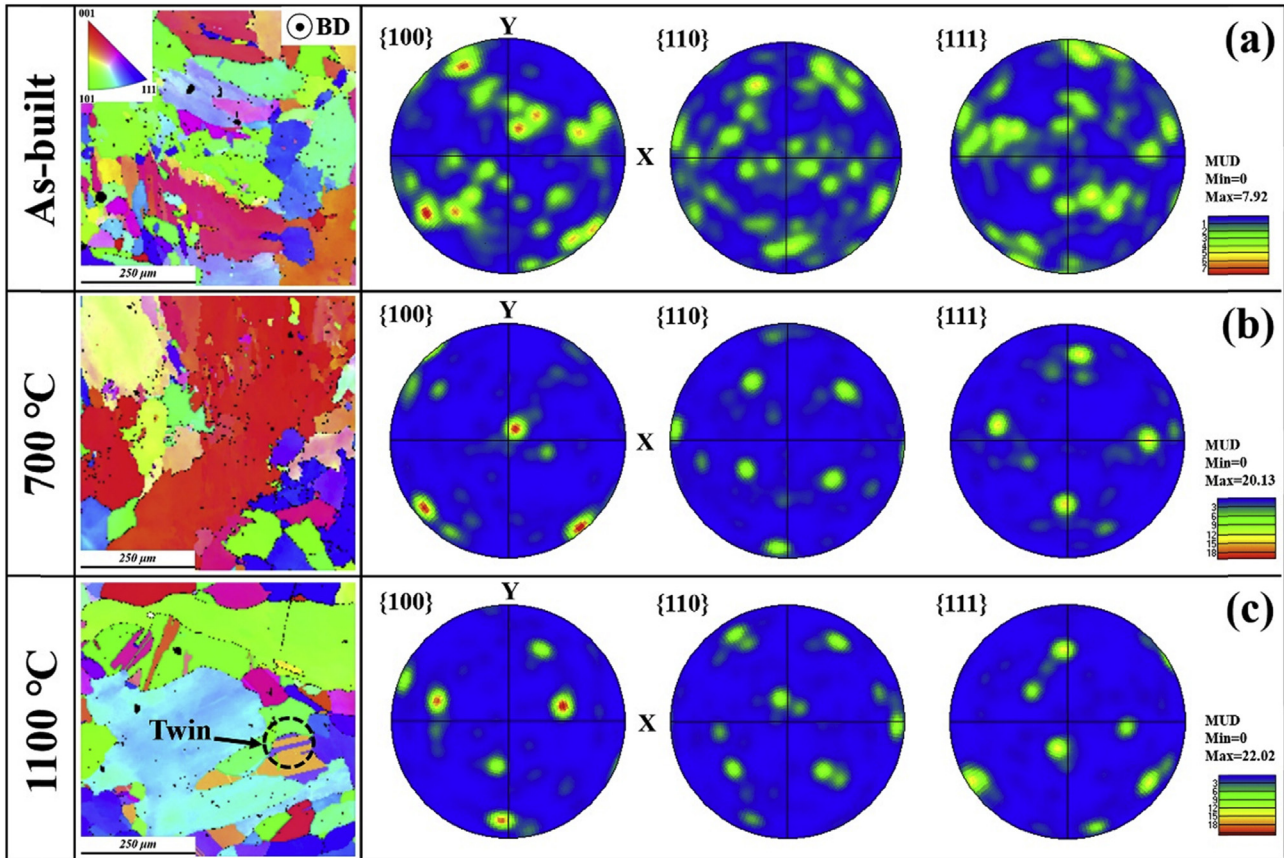


Fig. 15. IPF maps and PF of the as-built and heat treated CoCrFeMnNi HEAs on horizontal cross-section. Reproduced with permission [198]. Copyright 2019 Elsevier.

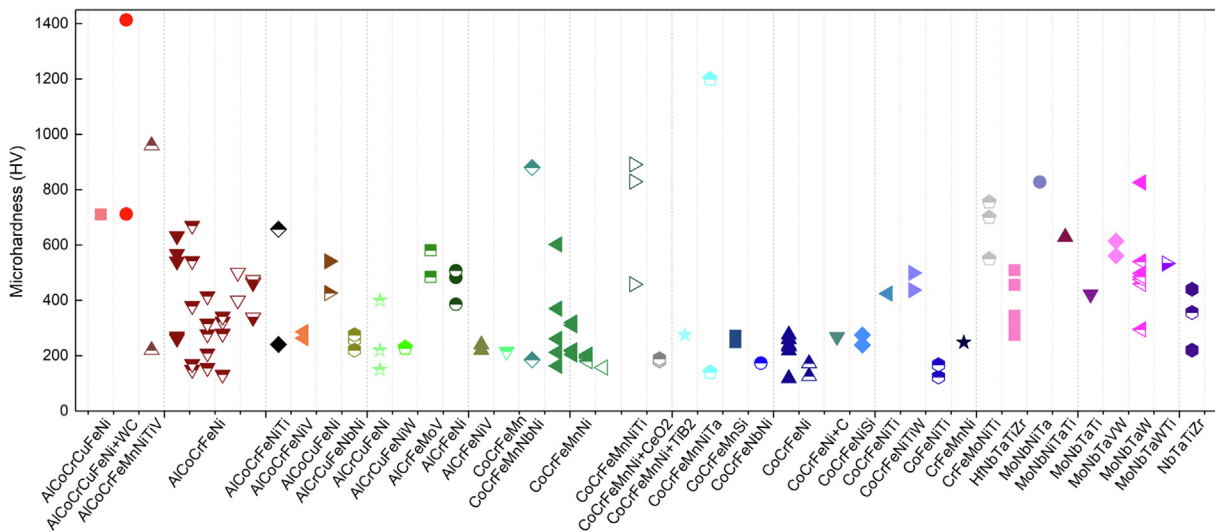


Fig. 16. Microhardness data of AM HEAs collected from the references. (The solid, top half-solid, open and bottom half-solid symbols represent HEAs fabricated by SLM, LMD, EBM and WAAM, respectively. Only considering the as-fabricated state).

the hardness even in the same HEA system varies in a wide range depending on the processing technology and alloy element ratio. In general, the hardness of HEAs with BCC phase structure (e.g. MoNbTaW) is higher than that of HEAs with FCC phase (e.g. CoCrFeNi). The higher solid solution hardening of the BCC phase in HEAs originates from the larger lattice distortion compared to the FCC phase. Wang [296] calculated the distribution of the shortest distances

between the same-element atoms at the nearest lattice position in the BCC and FCC structures using the principle of maximum entropy and Monte Carlo simulation method. It was found that for the BCC alloying systems with five or more principle elements, nearest neighbor atoms of the same element (like pairs) can all be avoided, whereas there are still a higher proportion of same elements in the first shell of quaternary (74.3%) and quinary (47.3%)

FCC HEAs. Thus, the larger proportion of unlike nearest neighbor pairs in the BCC phase results in larger distortion and consequently higher solution hardening.

With increasing Al content, the microhardness of LMD-deposited graded  $\text{Al}_x\text{CrCuFeNi}_2$  HEA increased gradually as a result of the increased proportion of BCC/B2 phase to FCC/ $\text{L1}_2$  phase [5], suggesting a much harder BCC/B2 structure comparing to the FCC/ $\text{L1}_2$  structure, consistent with previously reported  $\text{Al}_x\text{CoCrFeNi}$  fabricated by conventional arc melting and casting methods [297,298]. The hardness of EBM-fabricated  $\text{AlCoCrFeNi}$  HEA gradually decreased when approaching the bottom part of the samples, resulting from the increased portion of FCC phase [129]. A similar trend of changing hardness was also observed for compositionally graded  $\text{AlCoCrFeNi}$  HEA fabricated by LMD with varying Al concentrations [118]. A hardness reduction from 670 HV to 149 HV was reported for SLM-printed  $\text{AlCoCrFeNi}$  HEA with the Al/Ni ratio decreased due to the microstructure changing gradually from dendritic to columnar grains [116]. Note that the hardness among SLM, LMD, EBM and WAAM fabricated  $\text{AlCoCrFeNi}$  HEAs shows no significant difference. Chen et al. [145] fabricated  $\text{Al}_x\text{CoCu}_{1-x}\text{FeNi}$  HEA by LMD with varying Al and Cu contents. The highest hardness values for the produced three HEAs ( $x = 0.25, 0.5, 0.75$ ) were obtained at the top regions of the specimens, with the average values of 426.3 HV, 519.4 HV and 541.1 HV, respectively. For LMD-built compositionally graded  $\text{NbTaTiZr}$  HEA [95], the Nb-rich region exhibited the lowest hardness of 220  $\text{HV}_{0.1}$ , while the hardness was found to increase to 400  $\text{HV}_{0.1}$  with increased Zr concentration and then remained roughly constant for Zr-rich compositions. The microhardness of LMD-manufactured  $\text{MoNbTaW}_x$  HEA also showed an increasing tendency with increasing content of W [268]. Recently, the enhanced hardness due to the V addition was reported in LMD-built  $\text{AlCrFeMoV}$  HEA system [97], which increased from 485 HV to 581 HV when increasing the V content from 0.3 at.% to 18.5 at.%, attributed to the solid solution strengthening mechanism.

The relationship between the input energy and the hardness of SLM-manufactured  $\text{CoCrFeNi}$  was studied in [240]. It was observed that the hardness firstly increased from 247 HV to 276 HV with the input energy in the range of  $100 \sim 750 \text{ J}\cdot\text{mm}^{-3}$ , followed by a decrease to 233 HV with further increasing input energy, due to the impact of enhanced porosity. Zhou et al. [247] prepared  $\text{CoCrFeNiCo}_{0.05}$  HEA by SLM and tested the hardness of different phases. The results showed that the newly-formed carbide phase in the obtained HEA samples possessed a substantially higher hardness (1157 HV) than that of the FCC matrix (440 HV), which was generally considered to enhance the mechanical strength. Pegues et al. [169] carried out a systematic composition-hardness study on LMD-manufactured compositionally graded  $\text{CoCrFeMnNi}$  HEA with different refractory metals and alloy (Nb, Ta and Ti-6Al-4V). Generally, each HEA system showed a rather gradual increase in hardness with the addition of the respective refractory metal until approximately equiatomic compositions, afterwards the hardness increased significantly due to the presence of intermetallic phases.

#### 4.2. Tensile properties

Fig. 17 provides a summary of the relationship between the ultimate tensile strength and fracture elongation for different HEAs systems processed by AM techniques. It can be seen that the tensile properties vary strongly within the same HEA system, such as  $\text{AlCoCrFeNi}$ , depending on the obtained microstructure by different AM technologies and the chosen processing parameters [44]. As mentioned in Section 3.3, the anisotropic microstructure of AM produced HEA specimens with respect to the build direction usually exhibits an obvious texture. Consequently, anisotropic

tensile properties can be obtained and are significantly dependent on the grain orientation [216,242,258].

During tensile tests of LMD-fabricated  $\text{CoCrFeMnNi}$  HEA, ductile fracture occurred with dimple initiation related to nano-sized oxide particles, exhibiting higher yield strength and ductility compared with other AM and casting processes of the same HEA system [197]. Xiang et al. [19] proposed that the mechanical properties of  $\text{CoCrFeMnNi}$  specimens could be tuned through varying laser power and scanning strategy, arising from the modification of the microstructure. They reported that with the laser power increased from 1000 to 1400 W, the dominant  $\langle 001 \rangle$  texture transformed to a random texture, leading to a weaker anisotropy of the structure and better mechanical performance even compared to the as-cast alloy. In another work of Xiang et al. [199], strong anisotropy of plastic deformation between the scanning direction and deposition direction for single-direction deposited 1000 W and 1200 W specimens was observed, which was associated with the strong texture along the heat flux direction of the coarse columnar grains at the bottom region of the specimen. In contrast, isotropic plastic deformation for both scanning and deposition direction of the 1400 W specimen was observed due to the fine columnar grains and equiaxed grains, which showed no obvious preferred grain orientation.

Regarding the dependence of yield strength on the average grain size of a polycrystalline material, it is found that additive manufactured HEAs follow the Hall-Petch relation, as reported in [4,119,198]. Combined with the avoidance of brittle intermetallic compounds or second phases, the SLM-printed  $\text{CoCrFeNi}$  HEA possessed both high strength and good ductility. It is worth mentioning that the yield strength tripled compared to its cast equivalent [4]. In Zhou et al.'s work [98], among the LMD-deposited  $\text{CoCrFeNiNb}_x$  HEAs, the elongation of the  $\text{CoCrFeNi}$  ( $x = 0$ ) sample was as high as 92.5%, achieving the highest value of all additive manufactured HEAs reported so far. Meanwhile, compared with the as-cast counterpart, the  $\text{CoCrFeNiNb}_{0.1}$  sample exhibited both strength and ductility enhancement. From the fractured morphologies of the tensile specimens, numerous deep dimples can be observed in the as-deposited  $\text{CoCrFeNi}$  ( $x = 0$ ) HEA, suggesting a typical ductile fracture. While a hybrid fracture mode consisting of both dimples and raised edges was observed with the Nb addition, arising from the formation of ordered Laves phase.

Guan et al. [200] found that the tensile deformation process of the LMD-deposited  $\text{CoCrFeMnNi}$  HEA was mainly accompanied by dislocation activities with the assistance of deformation twins, resulting in comparable tensile strength to that of finer-grained wrought-annealed counterparts. Fig. 18 compares the true stress/work hardening rate (WHR) curves as a function of logarithmic strain for the additive manufactured and wrought-annealed samples. The additive manufactured sample showed a more rapid drop in WHR during straining and earlier intersection of WHR with true stress/logarithmic strain curve, proving earlier strain localization and lower work hardenability of additive manufactured alloy. It is discussed that the twinning has negligible influence on the strain hardening of additive manufactured alloy as its onset is very close to the necking instability point, where the uniform plastic deformability is already exhausted. The lower elongation of additive manufactured alloy was due to the increase in dynamic dislocation recovery rate during straining, which weakened the work hardening ability. For SLM-fabricated  $\text{Co}_{20}\text{Cr}_{15}\text{Cu}_{1.5}\text{Fe}_{38.5}\text{Mn}_{20}\text{Si}_5$  HEA, despite containing 1.5 vol% microcracks and pores, the sample exhibited an excellent strength-ductility synergy (1235 MPa and 17.2%, respectively) due to the sustained WHR arising from the deformation induced phase transformation [163]. A systematic study on mechanical properties of SLM-manufactured fine-grained  $\text{Cr}_4\text{Fe}_9\text{Ni}_6\text{TiW}$  HEA was conducted in [258,259]. It was found that the nano-sized particles dispersed in the grain interiors and at

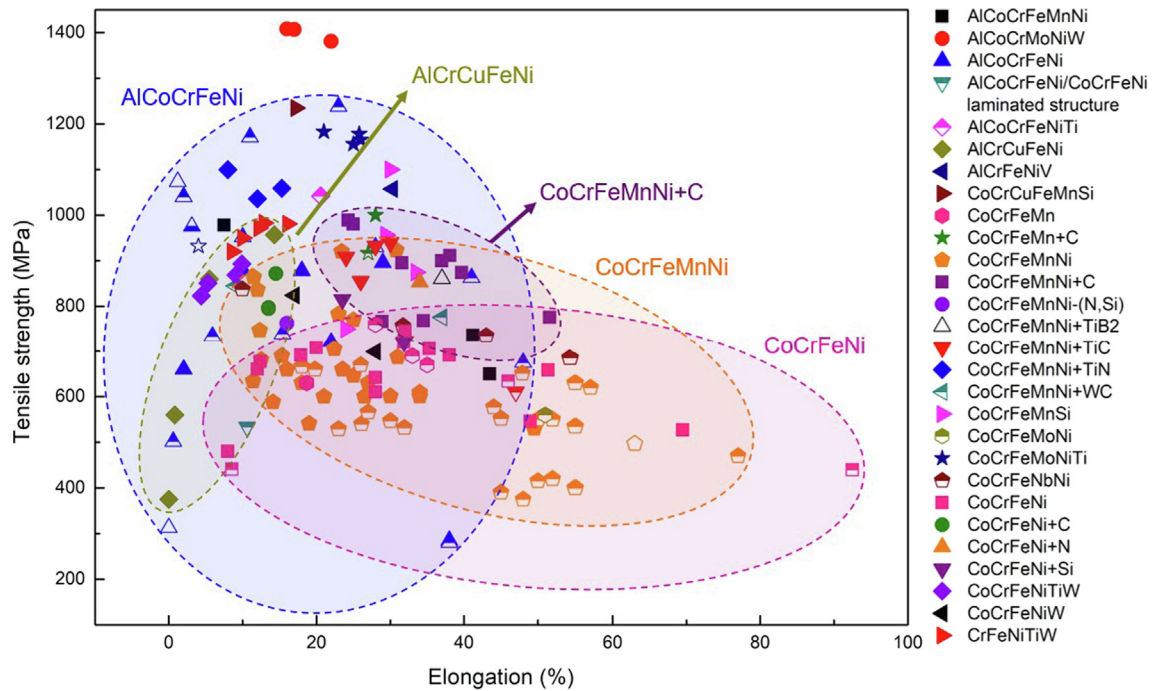


Fig. 17. Ultimate tensile strength vs. fracture elongation of different AMed HEAs. The solid, top half-solid, open and bottom half-solid symbols represent HEAs fabricated by SLM, LMD, EBM and WAAM, respectively (only considering the as-fabricated state).

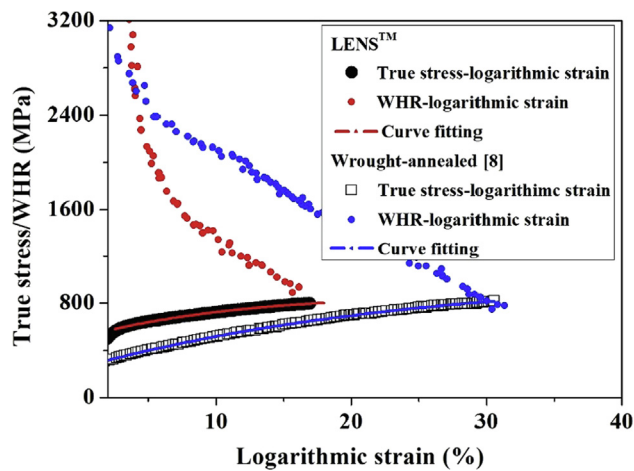


Fig. 18. True stress/WHR versus logarithmic strain for LMDed and wrought-annealed CoCrFeMnNi HEA. Reproduced with permission [200]. Copyright 2019 Elsevier.

the grain boundary served the dual purposes of blocking dislocations and storing dislocations, which alleviated the propensity for intergranular fracture and thus increased the total elongation before failure [259].

Some researchers have attempted to add interstitial elements to prepare HEAs composites to improve their strength. LMD-fabricated CoCrFeMnNi-based HEA with certain enhanced mechanical property was obtained by controlling the amount of the TiC addition [223]. With 5 wt.% TiC addition, the alloy exhibited a tensile strength and strain of 723 MPa and 32%, respectively, compared to 550 MPa and 50% of the sample without addition of TiC. Similarly, by adding TiN and WC, both increased tensile strength and reduced ductility of the CoCrFeMnNi HEA were obtained in [224] and [227], respectively. An exceptional strength-ductility synergy of an interstitial solute strengthened CoCrFeMn HEA was reported in [167], which surpassed that of most SLM-printed

conventional alloys by combinational effects of dislocation slip, deformation twinning and phase transformation. Park et al. [215–217] reported a high strength-ductility combination of SLM-printed C-doped CoCrFeMnNi HEAs through nano-scale solute heterogeneities in the matrix, as shown in Fig. 17, with the tensile strength and elongation in the range of 768–989 MPa and 24.3–51.6 %, respectively. The doping of interstitial N atoms to this CoCrFeMnNi HEAs also resulted in simultaneously enhanced strength and ductility due to the formation of ordered nitrogen complexes [179]. Furthermore, Si addition was also found to be beneficial for the improvement of the mechanical properties of additive manufactured HEAs. Hou et al. [164] added Si powders to the metastable Fe<sub>50</sub>Mn<sub>30</sub>Co<sub>10</sub>Cr<sub>10</sub> powders during SLM. The results showed that the strength of Si-containing metastable HEAs gradually increased with increasing Si, and the total elongation could still reach 30% above. This strength-ductility trade-off was because that Si increased the metastability of the FCC phase in the Fe<sub>50</sub>Mn<sub>30</sub>Co<sub>10</sub>Cr<sub>10</sub> HEA, promoting the phase transformation-induced plasticity to tune the twinning strain during the tensile deformation process.

Another metastable HEA, namely Fe<sub>60</sub>Co<sub>15</sub>Ni<sub>15</sub>Cr<sub>10</sub>, showed a much higher elongation of 69.5% than other SLM-fabricated HEAs, while with acceptable strength [241]. Fig. 19(a) shows the local strain rate distributions of the additive manufactured HEA under different global strains during tensile deformation process. It is worth noting that after the first necking at ~14.84% engineering strain, the strain-localized areas gradually moved to the end-side of the gage region during further deformation process, contributing to the steady hardening behavior and resultant increased elongation of the samples. The deformed microstructures under different local strains of the tensile-fractured sample analyzed by EBSD are shown Fig. 19(d-h). It can be clearly observed that with increasing local strain, the area fraction of the BCC phase gradually increased. At the end-side of the fractured sample, the local strain was 48.65% and the BCC phase fraction was around 51%, indicating that the extraordinary strain hardening after the first necking can be attributed to the

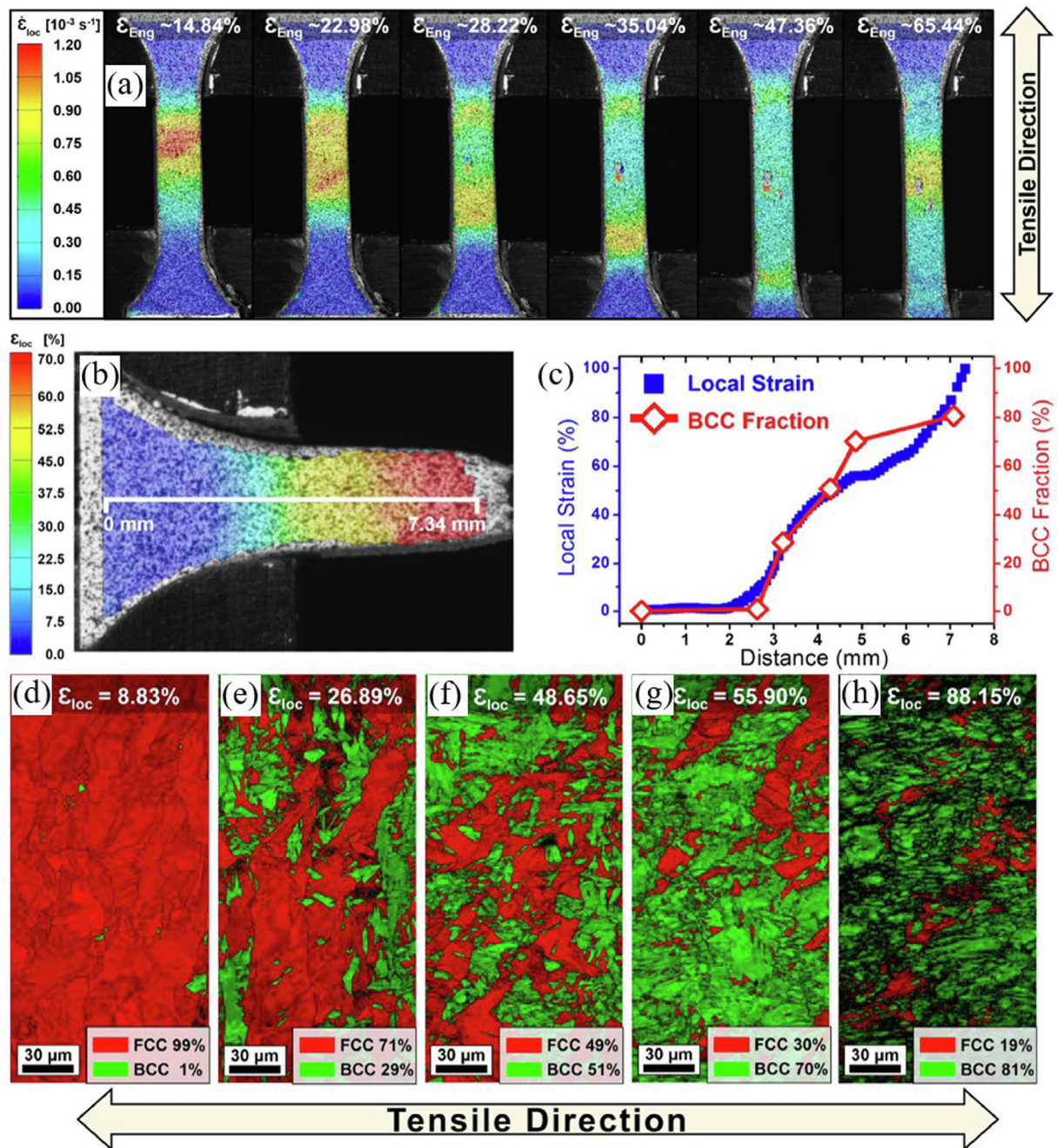


**Fig. 19.** (a) Local strain rate distributions of the SLMed Fe<sub>60</sub>Co<sub>15</sub>Ni<sub>15</sub>Cr<sub>10</sub> HEA under different global strains during tensile deformation process. (b) Local strain distribution maps on the fractured sample. (c) Evolutions of local strain and BCC phase fraction along the fractured region in (b). (d-h) EBSD phase maps superimposed by the image quality maps showing the deformed microstructures under different local strains. Adapted with permission [241]. Copyright 2021 Elsevier.

stable spreading of the strain-induced martensitic transformation into the end-side at the strain localized regions. Recently, eutectic HEAs have also been fabricated using different AM techniques [105,124,125,127]. Due to the ultrafine eutectic lamellar spacing and lamellar colony, the SLM-printed Al<sub>18</sub>Co<sub>30</sub>Cr<sub>10</sub>Mo<sub>1</sub>Ni<sub>30</sub>W<sub>1</sub> eutectic HEA exhibited excellent mechanical properties, with the room temperature yield and ultimate tensile strength, uniform elongation around 1000 MPa, 1400 MPa and 20%, respectively, reaching the highest strength among all additive manufactured HEAs (as shown in Fig. 17), indicating that eutectic HEAs have great application prospects in the field of AM [105].

#### 4.3. Compressive properties

Fig. 20 shows the data obtained from compression tests of different AM produced HEAs reported in the literature. Compared with the tensile properties, there are fewer studies of the compression properties.

Fujieda et al. [67] developed a study wherein compressive properties of AlCoCrFeNi HEA fabricated by EBM were compared parallel and perpendicular to the building direction. The best properties were obtained in the growth direction of the additive manufactured HEA, with a value of 1668 MPa. The EBM sample showed much higher plastic deformability than the cast counterpart during

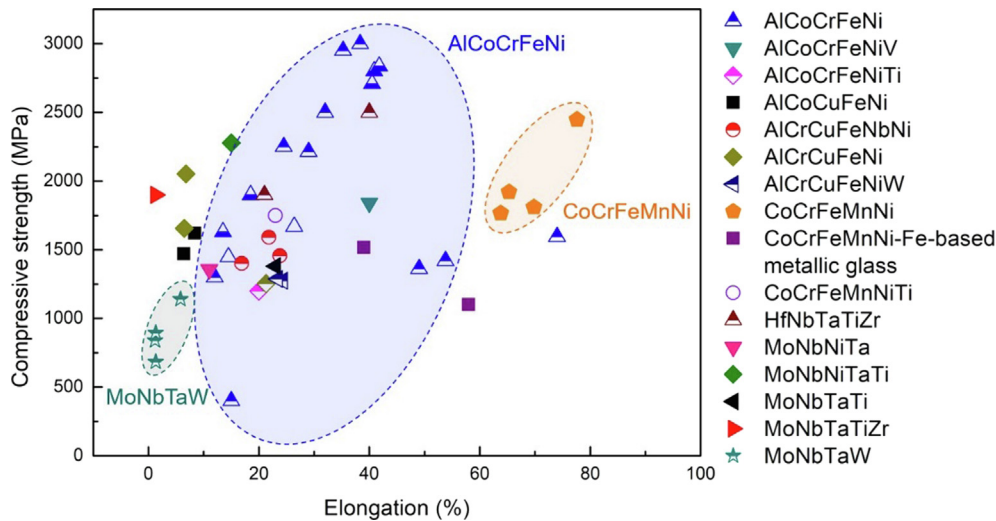


**Fig. 20.** Compressive strength and fracture elongation of different AMed HEAs. The solid, top half-solid, open and bottom half-solid symbols represent HEAs fabricated by SLM, LMD, EBM and WAAM, respectively (only considering the as-fabricated state).

the compressive tests, without significant loss of strength, which was attributed to the finer grains and more ductile FCC phases of the EBM samples [129]. On the other hand, the cast sample was almost entirely composed of a mixture of B2 and BCC phases, lacking the slip system, and thus triggering brittle fracture during the compressive test. The compressive strength of LMD-fabricated  $\text{Al}_x\text{CoCrFeNi}$  HEAs was observed to increase with increasing Al concentration, but at the expense of reduced ductility [113,114]. The  $\text{Al}_{0.3}\text{CoCrFeNi}$  sample showed a high and sustained WHR rate until the compressive test was stopped at a strain of 1.0, with the strength surpassing 1300 MPa. By contrast, a higher strength and a lower elongation of 2250 MPa and 24.5%, respectively, of the BCC alloy with  $x = 0.85$  was observed, induced by the high-volume fraction of spinodal second phase particles. A significant difference in the WHR and ductility between tension and compression was found during mechanical testing of LMDed  $\text{Al}_{0.3}\text{CoCrFeNi}$  [52], which was a direct consequence of the LMD fabrication technique. The exceptional high work hardening ability during compression test was due to the formation of twins induced by deformation, which were absent in the tension samples, as the critical stress required for the starting of twinning could not be reached before the final fracture. Anisotropy in mechanical property referring to the yield strength, flow stress and WHR was reported in SLM-printed  $\text{CoCrFeMnNi}$  HEA, which resulted from the difference in the grain size and Taylor factors for each loading axis affecting the critical stress of twinning [171]. For the compression tests along the loading axis of the scanning and the transverse directions, deformation on the plane along the building direction was accommodated by dislocation slip, while deformation twins occurred on the plane perpendicular to the building direction. It was found that the geometrically necessary dislocation (GND) density on each plane parallel to the loading axis differed about 2.5 times after the compression test. Moreover, a new yield strength prediction model regarding the Taylor factor, grain size and nano-sized oxides was proposed in this work, and the results agreed well with the experimentally measured yield strength. Anisotropy in compression properties of LMD-fabricated  $\text{AlCoCrFeNi}_{2.1}$  and SLM-built  $\text{AlCrCuFeNi}$  was also reported in [125] and [149], respectively. Fracture analysis indicated that the  $0^\circ$  specimen whose compression axis was parallel to the building direction exhibited quasi-cleavage fracture, while the  $90^\circ$  specimen whose compression axis was perpendicular to the building direction showed intergranular fracture, owing to the  $\langle 100 \rangle$  preferential

orientation of BCC grains, grain boundary strengthening effect and the existing microcracks [149].

In the LMD-deposited  $\text{MoNbTaW}$  HEA with varying W contents [268], it was found that the  $\text{MoNbTa}$  ( $W = 0$ ) alloy showed yield strength, compressive strength and elongation of 874 MPa, 1140 MPa and 5.8%, respectively. Compared to the vacuum arc melted  $\text{MoNbTaW}$  HEAs, 1.5% enhancement in the compressive strain was reported for the LMDed HEA, suggesting that the  $\text{MoNbTa}$  had appreciable machinability at room temperature [299]. Recently, a  $\text{AlCoCrFeNiTi/CoCrFeMnNi}$  laminated HEA with alternating  $\text{AlCoCrFeNiTi}$  and  $\text{CoCrFeMnNi}$  layers was manufactured by LMD technique [140]. Typical compressive stress–strain curves corresponding to two different loading directions of this laminated HEA are shown in Fig. 21, which exhibited enhanced synergy of strength and plasticity compared to the monolithic bulk HEAs, with yield strength up to 990 MPa and no complete fracture until 80% strain, demonstrating a feasible and flexible way to fabricate HEAs with superior mechanical properties through AM techniques.

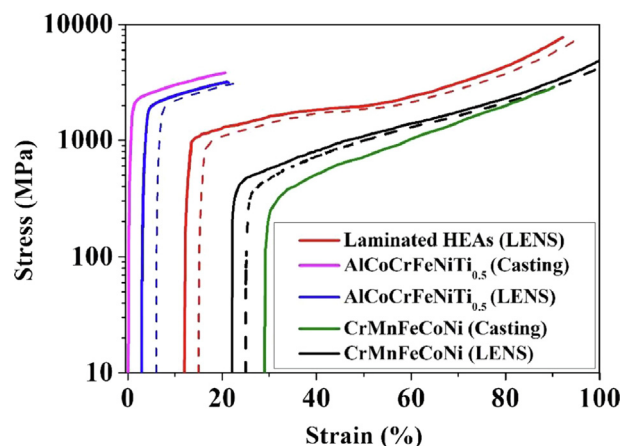


**Fig. 21.** Typical compressive stress–strain curves of the LMD-fabricated  $\text{AlCoCrFeNiTi/CoCrFeMnNi}$  laminated HEA, compared to those of LMD-fabricated and as-casted monolithic HEAs. Solid and dashed curves corresponded to the compressive tests with the load axis parallel and normal to the XY-plane, respectively. The compressive tests of  $\text{AlCoCrFeNiTi/CoCrFeMnNi}$  laminated HEA and the monolithic  $\text{CoCrFeMnNi}$  HEA were interrupted. Reproduced with permission [140]. Copyright 2020 Elsevier.

#### 4.4. Cryogenic and high-temperature properties

The cryogenic and high-temperature mechanical properties of additive manufactured HEAs are also highlighted by some researchers, and the specific values are listed in appendix A, with the CoCrFeMnNi HEA system being the most studied one.

Qiu et al. [18] conducted tensile tests on the LMD-built CoCrFeMnNi at  $-196\text{ }^{\circ}\text{C}$  to study the properties at cryogenic temperature. Both enhanced yield strength and ductility were obtained with decreasing the temperature from  $25\text{ }^{\circ}\text{C}$  to  $-196\text{ }^{\circ}\text{C}$ . A dominant deformation mechanism consisting of large initial dislocation density and dislocation motion was revealed by the EBSD and X-ray diffraction (XRD) analysis. Additionally, deformation-induced twinning at large strain levels under cryogenic deformation conditions played an important role in enhancing both the strength and ductility of HEA. Excellent cryogenic properties of the same HEA systems were also reported in [19]. As the testing temperature decreased from  $20\text{ }^{\circ}\text{C}$  to  $-196\text{ }^{\circ}\text{C}$ , the yield strength, tensile strength and elongation increased from 290 MPa, 535 MPa and 55% to 402 MPa, 878 MPa and 95%, respectively. Fig. 22 shows the microstructure evolution of LMD-produced CoCrFeMnNi after tensile test at  $25\text{ }^{\circ}\text{C}$  and  $-130\text{ }^{\circ}\text{C}$ , respectively [212]. An increasing Kernel average misorientation (KAM) value reflects the increasing dislocation density, indicating that the dislocation movement contributes part of the deformation behavior. The KAM value of the specimen fractured at  $-130\text{ }^{\circ}\text{C}$  became as high as 3, suggesting that there was an obvious dislocation trapping. In addition, the specimen deformed at  $-130\text{ }^{\circ}\text{C}$  showed multiple deformation-induced twins when compared with the specimen deformed at  $25\text{ }^{\circ}\text{C}$ , as the red lines presented in Fig. 22(f), which made the HEA at cryogenic conditions behaved in a similar way to the twinning-induced plastic steel [300], contributing to the enhanced cryogenic strength and ductility at the same time. Furthermore, an ultra-strong cryogenic strength of 1450 MPa was observed in the SLM-manufactured in-situ nano oxide reinforced CoCrFeMnNi HEA, which was mainly attributed to the formation of a relatively large number of deformation twins at cryogenic temperature [183].

With respect to the high-temperature properties of the same HEA system, Li et al. [227] reported that, at  $600\text{ }^{\circ}\text{C}$ , the LMD-manufactured CoCrFeMnNi HEA with 5 wt.% WC addition exhibited enhanced tensile strength from 280 MPa to 405 MPa, with reduced ductility from 57% to 45%, comparing to the WC-free sample. For SLM-printed equiatomic CoCrFeMnNi HEA, exceptional mechanical properties up to  $700\text{ }^{\circ}\text{C}$  (with a compressive yield strength of 545.8 MPa) were reported in [176], which surpassed that of the CoCrFeMnNi HEA fabricated by other manufacturing processes. Overall, the performance of additively fabricated CoCrFeMnNi HEAs at low temperature is significantly better than that at room temperature and high temperature, which is attributed to the activation of multiple deformation and strengthening mechanisms at low temperature.

There are also some promising results from other AM produced HEA systems in terms of cryogenic and high-temperature properties. For example, in LMD-fabricated  $\text{Co}_{10}\text{-Cr}_{10}\text{Fe}_{49.5}\text{Mn}_{30}\text{C}_{0.5}$  interstitial HEA [168], superior tensile strength of 1041 MPa and 1267 MPa were obtained at  $-40\text{ }^{\circ}\text{C}$  and  $-130\text{ }^{\circ}\text{C}$ , respectively. Compared to the tensile sample at room temperature, where both twinning- and transformation-induced plasticity were activated, almost no twinning was detected in the samples tested at cryogenic temperatures. Instead, a much higher fraction of strain-induced HCP phase transformation was observed. The mechanical properties of LMD-fabricated CoCrFeMo<sub>0.2</sub>Ni HEA were remarkably improved from room temperature to  $-196\text{ }^{\circ}\text{C}$ , with the tensile strength and ductility

increased by 70% and 28% (from 560 MPa and 51% to 928 MPa and 60%), respectively. The high-temperature compressive performance of LMD-deposited MoNbTaW HEA was investigated in [268], it was found that the W-free MoNbTa alloy exhibited excellent mechanical properties of yield strength, compressive strength and elongation at  $1000\text{ }^{\circ}\text{C}$  with values of 530 MPa, 684 MPa and 8.5%, respectively, reflecting a better performance than traditional refractory alloys and presenting potential applications in the aerospace industry.

#### 4.5. Fatigue properties

In-depth understanding of fatigue behavior of engineering materials is crucial for structural applications, as the fatigue properties are found to be responsible for most of catastrophic failures in mechanical and structural systems [8,301-303]. Considering the HEAs' great potential for future structural applications, Jin et al. [192] studied the cyclic plasticity and fatigue damage of SLM-printed CoCrFeMnNi HEA by different scanning strategies, the maximum tensile stress responses during the cyclic loading test were shown in Fig. 23. It can be observed that all samples showed a short cyclic hardening during the first five cycles, followed by a cyclic softening behavior. The scanning strategies appeared to have noticeable effect on the plastic deformation behavior of printed HEAs samples in terms of fatigue crack propagation, but little influence on the fatigue life. The surface condition, however, appeared to have a significant effect on the fatigue performance, as the fatigue life of the machined sample was enhanced by about 20%. This was attributed to the removal of sub-surface key-hole porosity of as-printed HEAs, which delayed the initiation of fatigue cracks. The microstructure analysis revealed that the dislocation slip was the single dominant mechanism for cyclic plasticity of printed CoCrFeMnNi HEA, which was different from the plastic deformation under monotonic loading, where both dislocation slip and deformation twinning mechanism were identified. Similarly, the dislocation slip dominated deformation mechanism at cycling loading was also reported in additive manufactured CoCrFeNi HEA [237]. In contrast, Kim et al. [180] detected the formation of deformation twins in high-cycle fatigue testing of SLM-built CoCrFeMnNi HEA, which together with the unique microstructure contributed to the much higher fatigue resistance than homogeneous HEAs.

#### 4.6. Creep behavior

HEAs have been reported to have good creep resistance due to sluggish atomic diffusion and large lattice distortion [304,305]. However, the creep properties of additive manufactured HEAs can be different from that of HEAs manufactured by conventional methods, as the AM processes usually lead to high dislocation density and smaller grain size [295]. Kim et al. [175] investigated the high-temperature compressive creep behavior of SLM-printed CoCrFeMnNi HEA, which revealed an excellent creep resistance at  $600\text{ }^{\circ}\text{C}$ , with stress exponents  $n$  of 3.45 and 6.45 for low stress region and high stress region, respectively, suggesting different creep mechanisms at these two regions, namely viscous glide and dislocation climb, respectively. Xu et al. [172] studied the influence of the peak holding load on the nanoindentation creep deformation behavior of SLM-printed CoCrFeMnNi HEA using a Berkovich indenter. Fig. 24(a) shows the typical load-displacement curves of varying peak loads recorded during the indentation creep tests. It can be observed that the plastic deformation occurred at the beginning of the holding stage, and the displacement increased gradually during the holding process, then, the creep appeared. The creep displacement increased with increasing maximum holding

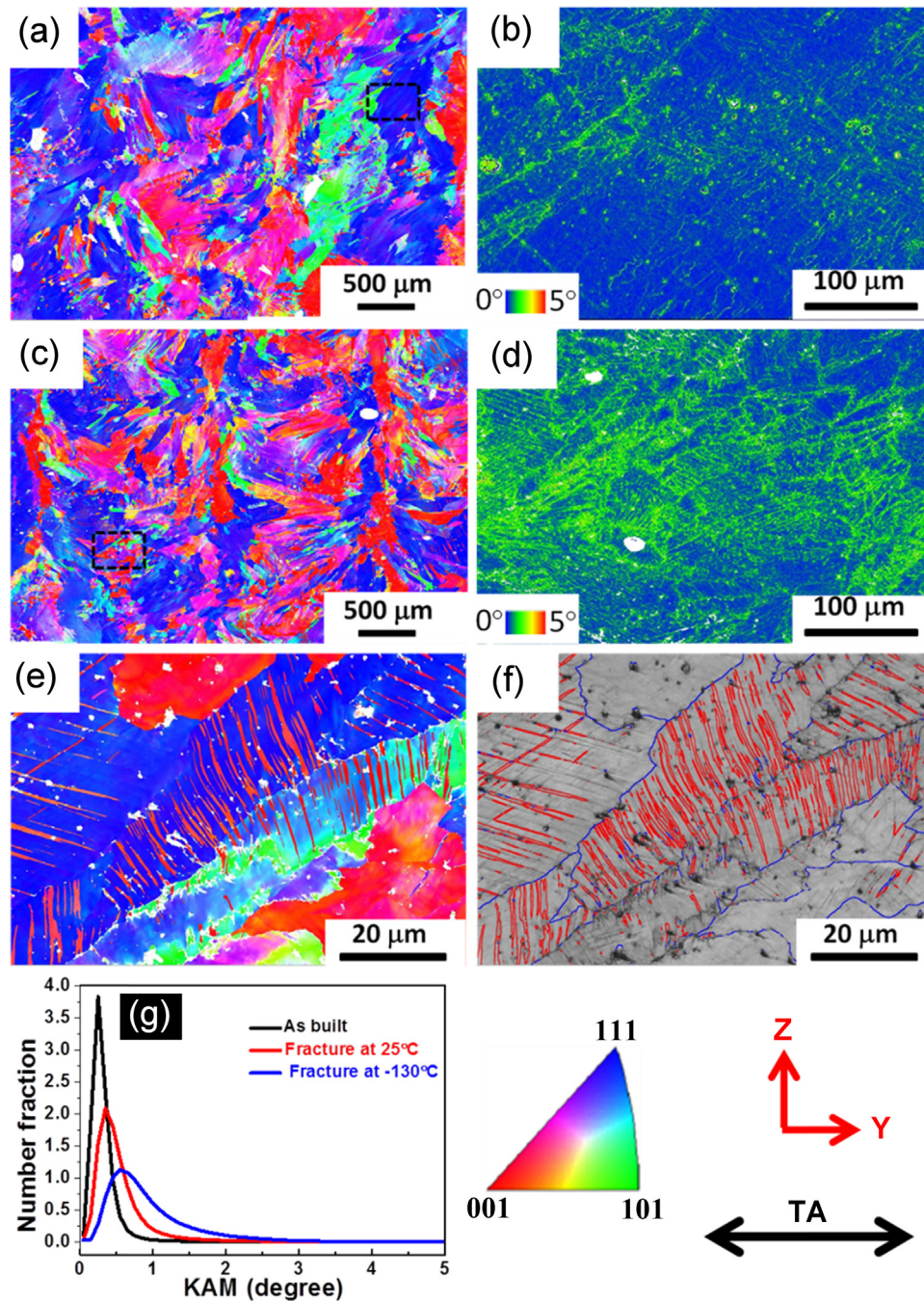


**Fig. 22.** (a) and (c) EBSD IPF map of the LMD-produced CoCrFeMnNi HEA fractured at 25 °C and –130 °C, respectively. (b) and (d) KAM map of the corresponding rectangular area in (a) and (c), respectively. (e) and (f) EBSD IPF and grain boundary map of the specimen fractured at –130 °C. (g) KAM distribution of as-built, fractured specimens at 25 °C, and –130 °C, respectively. Reproduced with permission [212]. Copyright 2018 Elsevier.

load, and the deformation was not fully recovered and remained unchanged after unloading, confirming that the observed dimensional changes were owing to creep mainly arising from dislocation motion, rather than just elastic plus plastic deformation. The nanoindentation-based measurement was also applied to study the nanoscale creep deformation mechanism of additive manufactured  $\text{Al}_4(\text{CoCrFeNi})_{94}\text{Ti}_2$  HEA [138]. The crystallographic orientation dependent creep properties were also observed in this work, where the {101} grain showed the greatest creep resistance with the lattice diffusion dominant creep mechanism. It was also revealed that heat treatment could eliminate the nanoscale creep anisotropy but reduce the creep resistance; however, the reasons remained unclear and further study was still needed.

#### 4.7. Post-treatment effect

Post-treatment plays an important role in removing various metallurgical defects as well as releasing the residual stress in AM fabricated HEAs, which has a significant effect on the improvement of the mechanical properties [60,236].

The effect of annealing temperatures on the mechanical properties of SLM-built CoCrFeNi HEA was investigated in [233]. Almost unchanged tensile strength was observed during the whole range of annealing temperature from 500 °C to 1300 °C due to the reduction of residual stress (< 900 °C) and the formation of twins and dislocations networks (> 1100 °C). However, a significantly increased ductility along with decreased yield strength and

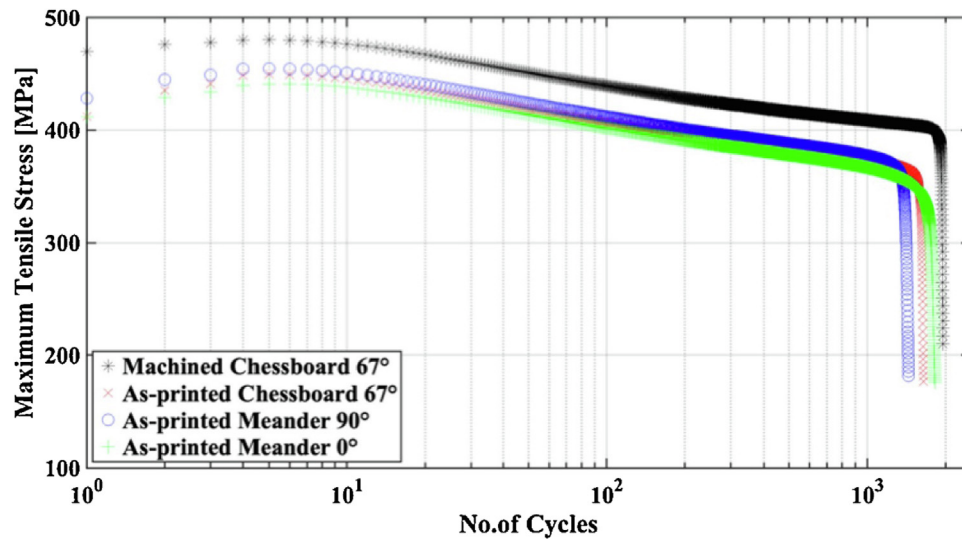


Fig. 23. Cyclic plastic deformation response of SLM-printed CoCrFeMnNi HEA using different scanning strategies and surface conditions. Reproduced with permission [192]. Copyright 2020 Elsevier.

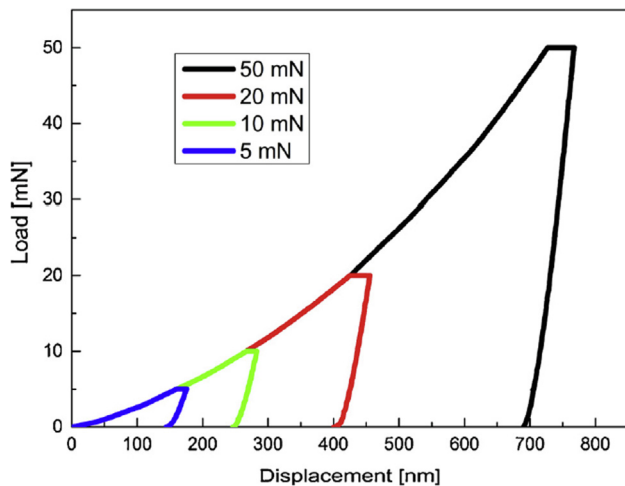


Fig. 24. Representative load–displacement curves at different maximum holding loads of SLM-printed CoCrFeMnNi HEA. Reproduced with permission [172]. Copyright 2019 Elsevier.

hardness was also observed with the increasing annealing temperature. Sistla et al. [116] reported that annealing at high temperature resulted in the formation of  $\sigma$  phase in some compositions of SLM-printed AlCoCrFeNi HEA, which combined with solid solution strengthening accounted for the good compromise between hardness and strength of the heat-treated samples. For LMD-fabricated AlCoCrFeNi, ageing led to the formation of soft FCC phase and consequently reduced compressive strength and improved ductility [53]. A typical cleavage fracture was observed except for the 800 °C and 1000 °C aged specimens, which showed a combination of cleavage and quasi-cleavage fracture due to the presence of FCC precipitates in the B2 grains. With proper cooling rate, HIP can be applied to improve the mechanical properties of FCC HEA, while it degraded the tensile properties of the dual-phase Al<sub>0.3</sub>CoCrFeNi HEA due to the coarsening of hard precipitates along the BCC grain boundaries, leading to brittle fracture during the tensile tests [113]. It is worth mentioning that for the single-phase FCC Al<sub>0.3</sub>CoCrFeNi HEA in this study, a high and sustained WHR was observed during the compression process, where the test was stopped at a true strain of 1.0 without the specimens' failure.

Consequently, fine mechanical twins were found throughout the microstructure after compression as the required high stress for the activation of twins was achieved for this FCC HEA. Meanwhile, both the ductility and WHR during the tensile test were improved compared with the as-deposited condition after HIP treatment due to the effective dissolution of grain boundary particles. Li et al. [185] found that the Mn segregation observed in as-built CoCrFeMnNi disappeared after HIP, leading to improved densification and tensile strength but reduced elongation.

Fujieda et al. [65] studied the influence of solution treatment with different cooling rates (water-quenched and air-cooled) on the EBM-fabricated CoCrFeNiTi-based HEA. The results are presented in Fig. 25. Improved tensile properties (strength and elongation) can be observed, notably when water quenching is applied, as shown in Fig. 25(a), due to the homogeneous precipitation of fine ordered particles with Ni and Ti enrichment (Fig. 25(b)). It was demonstrated that the yield strength of the heat-treated samples was proportional to the square root of the product of the volume fraction and radius of ordered particles. For LMD-deposited CoCrFeMnNi, the microhardness reduced after heat treatment at higher temperature due to the grains coarsening. It was shown that the relaxation of tensile residual stress, mainly induced by the dislocation gliding and climbing at high temperature, was beneficial for the enhancement of both tensile strength and ductility [198]. Decreased microhardness was also observed in SLM-produced AlCoCuFeNi [142] and AlCrFe<sub>2</sub>Ni<sub>2</sub> HEA [156] during the heat treatment process due to the precipitation of the softer FCC phase and the coarsening of the microstructures. However, the compressive properties of AlCoCuFeNi were significantly improved, as the 1000 °C heat-treated sample exhibited fracture strength and plastic strain of 1600 MPa and 13.1%, respectively, arising from the effective combination of BCC and FCC phases [142].

An interesting work investigating the effect of LSP on LMD-fabricated CoCrFeMnNi HEAs was conducted in [53,202], where both the strength and ductility of the as-built HEAs were significantly enhanced from 531.7 MPa and 31.9% to 639.9 MPa and 61%, respectively. The fracture mode transformed from the combination of brittle and ductile fracture to single ductile fracture after multiple LSP treatment due to the resulting compressive stress state, pores closure as well as the formation of a sandwich structure (nanograins hardened surface layer and softened core).

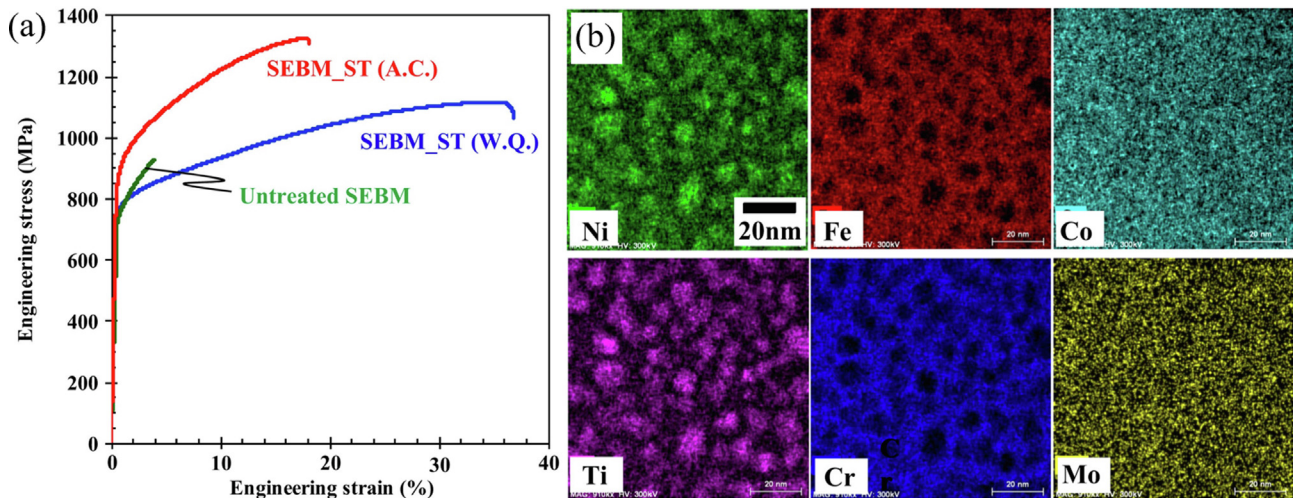


**Fig. 25.** (a) Tensile engineering stress–strain curves of untreated and solution-treated  $\text{Co}_{1.5}\text{CrFeNi}_{1.5}\text{Ti}_{0.5}\text{Mo}_{0.1}$  HEA specimens. (b) STEM-EDX elemental mapping of EBM specimen by water quenching after solution treatment. Adapted with permission [65]. Copyright 2016 Elsevier.

#### 4.8. Strengthening mechanisms

Up to now, researchers have proposed a variety of strengthening mechanisms for AM processed HEAs, such as grain refinement [67,119,185,212,227,235], solid solution strengthening [236,246–248,251], dislocation network strengthening [107,153,167,170,200,213,235] and precipitation hardening [96,136,153,210,227], which will be summarized in detail in this part.

In the EBM-fabricated AlCoCrFeNi specimen, the enhancement in plasticity was due to the grain refinement and the presence of the FCC phase [67]. Zhang et al. [142] also found that the strength-ductility trade-off was associated with the FCC phase precipitation in SLM-built AlCoCuFeNi HEA, which toughened the brittle HEA and led to significant strain hardening and higher ductility. Deformation mechanism of EBM-produced CoCrFeMnNi HEA was dominated by the dislocation movement with limited contribution from mechanical twins [213]. Experimental results revealed that the cellular structure did not promote the mechanical strength without the existence of surrounding dislocation networks. The formation of the  $\sigma$  phase and ultra-fine grains during the SLM process accounted for the improvement of mechanical properties compared to conventionally solidified CoCrFeMnNi HEA [185]. Zhu et al. [170] reported that the excellent ductility associated with steady strain hardening of SLM-printed CoCrFeMnNi was controlled by the dislocation trapping and retention mechanism within the cellular structures, as revealed by TEM analysis. Generally, the deformation process is controlled by the hierarchical dislocation activities, while the deformation twins make an additional contribution to the plastic flow behavior. Dislocation activity and deformation twins are two common deformation characteristics of FCC HEAs with low stacking fault energy. Besides, quantitative analysis showed that the cellular structures significantly contributed to the enhancement of strength by dislocation hardening instead of cellular boundary strengthening, as proposed in [212] for the LMD-manufactured HEA with the same composition.

Yao et al. [158] reported that the sub-grains in SLMed AlCrFeNiV with FCC phase significantly contributed to the enhancement of strength through dislocation hardening, and the excellent ductility was related to the progressive work hardening mechanism controlled by the heterogeneous distribution of  $\text{L}_{12}$  nanophase within the sub-grains. The schematic diagram of the dislocation formation and movement is shown in Fig. 26. Dislocations firstly appear in

the subgrains with low dislocation density. However, their movement is obstructed by the  $\text{L}_{12}$  nanophase and also pre-existing dislocations. The  $\text{L}_{12}$  nanophase acts as a strong diffuse attractive barrier, which can trap the dislocations movement and form anti-phase boundaries as it is being sheared by the dislocations. Besides, the coherent interface of FCC– $\text{L}_{12}$  phases with low misfit can lead to a minimized elastic strain accumulation and thus lower susceptibility for the crack initiation at the interfaces. The strength of the material is further enhanced via the interaction between the newly-formed and pre-existing dislocations.

The addition of carbon in SLM-processed CoCrFeNi-based HEA contributed to better mechanical properties by combining solid solution strengthening, dislocation network strengthening and nano-sized carbides strengthening [215,246–248]. Zhu et al. [167] reported the combined activation of multiple deformation mechanisms including the phase transformation, dislocation slip and deformation twins could maintain a stable work hardening behavior under high stress levels, contributing to enhanced ductility of SLM-built C-containing CoCrFeMn HEA. The as-built structure was mainly FCC and at the early stage of deformation, there was a small fraction of deformation induced HCP martensite and few deformation twins (Fig. 27). The increase in deformation strain was accompanied by a larger fraction of HCP martensite and substantial activation of deformation twinning. The KAM map associated with each deformation stage implied that the density of GNDs increased with increasing strain. The addition of interstitial atoms like carbon to the composition of CoCrFeMn HEA increased the stacking fault energy and thus the phase stability. Accurate tuning of the carbon composition can trigger twinning-induced plasticity while maintaining transformation-induced plasticity, resulting in further enhancement of the strain hardening ability. Moreover, carbon addition may contribute to the strength of the HEA through interstitial strengthening [306]. Recently, a novel strengthening mechanism in view of the interactions between dislocation loops and dislocations was proposed for SLM-fabricated Si-containing CoCrFeNi HEA [251], where the strengthening contribution to the enhanced yield strength was quantitatively analyzed. It was also shown that the improvement in the mechanical properties of LMDed CoCrFeMnNi HEA with TiC addition was induced by the introduction of micron-sized TiC as secondary reinforcement phase [223], which was anticipated to hinder the propagation of slip bands. In SLM-processed CoCrFeMnNi HEA matrix composite with TiN particles [224–226], it was found that the ceramic

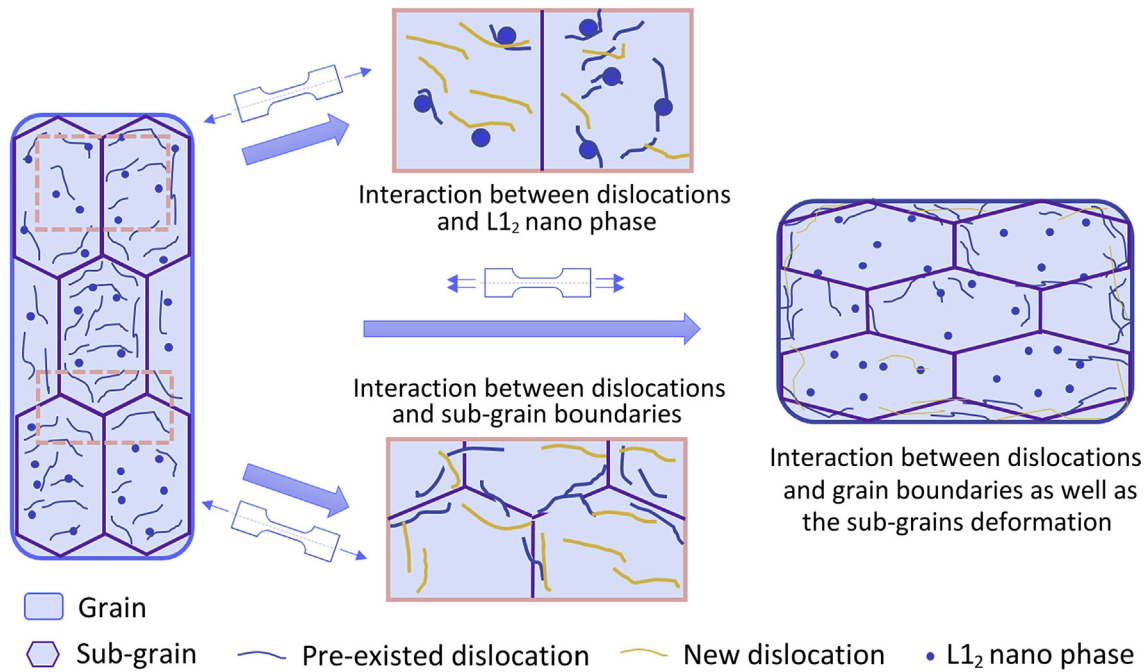


Fig. 26. Schematic diagram of the interaction between dislocations and obstacles during the tension process. Adapted with permission [158]. Copyright 2019 Elsevier.

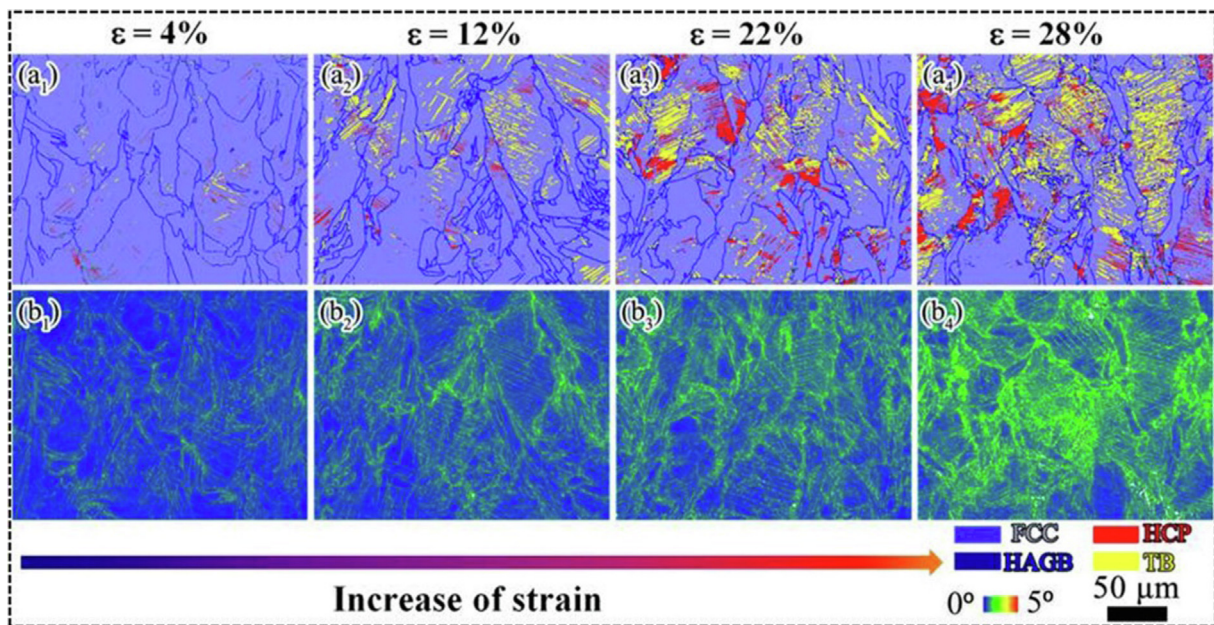


Fig. 27. EBSD phase and grain boundary maps showing microstructural evolution at different strain levels (top row) and corresponding KAM maps (bottom row) of SLM-processed C-doped CoCrFeMn. Reproduced with permission [167]. Copyright 2019 The Authors.

reinforcements, which were uniformly distributed at the grain boundaries, contributed to the pinning effects for strengthening. With 5 wt.% WC addition, the improvement in mechanical properties of LMD-deposited CoCrFeMnNi could be attributed to the formation of Cr<sub>23</sub>C<sub>6</sub> precipitations [227], which promoted the heterogeneous nucleation of grains, and consequently blocked the dislocation motion and enhanced the hardening effect of the AM specimens.

In a novel AlCrFeMoV alloy system, the high solubility of V was found to offer a wide range of solid solution strengthening for BCC matrix with complex composition but simple structure [97]. The solute atoms increased the frictional resistance to the dislocation

movement during the deformation process, thereby enhancing the strength of the alloy. Sarswat et al. [96] proposed that precipitation hardening was the major strengthening mechanism for compositionally complex AlCoFeNiSmTiVZr alloys and especially, Al was among the key elements for such precipitate phase formation. Furthermore, Nartu et al. [119] reported that the enhanced yield strength of LMD-fabricated Al<sub>0.3</sub>CoCrFeNi HEA was associated with the nano-sized Al-Ni enriched solute clusters, and a simple cluster-dislocation interaction model containing the coherent strain field of these clusters has been established. It was concluded that these clusters acted as strain centers which interacted with the dislocations during plastic deformation process and led to

enhanced yield strength. In particular, Yang et al. [258] reported that the control of grain orientation was an effective approach to enhance the strength and simultaneously improve the ductility of SLMed CrFeNiTiW alloys, as grains with different orientations can hinder the propagation of pre-existed cracks, and increase the crack expansion route, which would absorb more fracture energy and improve the crack tolerance significantly. Five strengthening mechanisms including lattice friction stress, grain boundary strengthening, solid solution strengthening, dislocation strengthening and Orowan strengthening related to nano-sized oxides in the matrix for the additive manufactured equiatomic CoCrFeMnNi HEA were proposed in [171,183]. Quantitative calculation of various contributions to the total strength demonstrated the most important role was played by the Orowan strengthening with a value of 44%.

## 5. Functional properties of additive manufactured HEAs

### 5.1. Corrosion resistance of additive manufactured HEAs

The corrosion characteristics of HEAs depend on the interaction between the service environment and materials, which for the latter is usually determined by the alloying elements, phase transformation and phase segregation. Some recent research works considering the corrosion resistance of AM processed HEAs will be discussed in this part.

Wang et al. [53] found that the corrosion behavior of the AlCoCrFeNi HEA manufactured by LMD was less competitive than that of 304 L stainless steel. Pitting corrosion occurred after the breakdown of the passivation film. The Al-Ni enriched B2 matrix was corroded severely, which was attributed to galvanic coupling effects with Cr-Fe enriched FCC precipitates at micro scale, where the FCC precipitates acted as the cathode while the B2 matrix acted as the anode. As a result, an electric potential existed when the sample was placed in the electrolyte solution, which offered a strong driving force for the corrosion of the Cr-poor B2 matrix. The electrochemical measurement in artificial sea water revealed that the corrosion behavior of EBM-processed AlCoCrFeNi sample (0.112 V vs. Ag/AgCl) was inferior to that of the cast counterpart (0.178 V vs. Ag/AgCl) [64]. The corrosion resistance of SLM-built AlCoCrFeNi HEA was improved with the increase of VED, as reflected by the increasing corrosion potential [112]. It was concluded that the increase of B2 phase content resulting from increasing VED, in combination with the lack of anode and cathode active surfaces, helped reduce the corrosion susceptibility and further improve the corrosion resistance of the SLM HEA, which revealed a different corrosion mechanism compared to [53]. The as-built CoCrFeMnNi by LMD [197] exhibited a lower re-passivation potential and tortuous pit morphology due to the selective attack on the intercellular regions, suggesting a higher susceptibility to local corrosion. A Cr-depleted passivation oxide film with substantial incorporation of Mn cations was proposed as the primary mechanism for the local corrosion susceptibility of this additive manufactured HEA. Similarly, a Cr-depleted oxide film ((Mn,Co,Ni)Fe<sub>2</sub>O<sub>4</sub>) was also observed in CoCrFeMnNi HEA after the exposure testing in molten NaNO<sub>3</sub>-KNO<sub>3</sub> mixture [58].

Ren et al. [189] systematically studied the corrosion resistance of SLM-printed and as-cast CoCrFeMnNi HEA in 3.5 wt.% NaCl solution, and the results are shown in Fig. 28. Both the alloys showed multiple small spikes in open circuit potential (Fig. 28(a)), suggesting breakdown and re-passivating prior to the stabilization of the open circuit potential after ~6000 s. As observed from Fig. 28(b), the values of corrosion potential and current density were similar for both alloys. However, the SLM-printed HEA exhibited a wider passive region of ~386 mV compared to the as-cast HEA

(~200 mV). The Nyquist plots obtained from electrochemical impedance spectroscopy and the equivalent circuit (Fig. 28(c) and (d)) revealed a higher polarization resistance of the SLM-printed HEA due to the extensive metastable pitting arising from the high density of micropores in the as-cast counterpart, where the micro-segregation regions also functioned as active sites for the initiation of corrosion, which is consistent with the reported results in [194]. However, another opposite result was reported in [177], where the cast sample exhibited a better corrosion resistance than the SLM-built CoCrFeMnNi HEA, as a higher density of defects (dislocations, pores and cracks) existed in the SLM sample. Furthermore, different corrosion resistance was found between the planes perpendicular and parallel to the building direction for the SLM sample, owing to different grain orientations, grain sizes and surface characteristics.

A comparable analysis of corrosion resistance on SLM and EBM CoCrFeNiTi specimen in a 3.5 wt.% NaCl solution was carried out in [65,230], and a higher pitting potential was measured for the SLMed HEA than that of EBM, with values of  $0.88 \pm 0.03$  V and  $0.50 \pm 0.04$  V vs. Ag/AgCl, respectively. The pitting-corrosion resistance was further improved to  $1.00 \pm 0.01$  V and  $0.90 \pm 0.01$  V vs. Ag/AgCl for SLM and EBM specimens, respectively, by water quenching after solution treatment. The obtained properties exceed those of conventional high corrosion resistance alloys such as Ni-based super alloys and super duplex stainless steels used in harsh corrosive environments. It was reported that the pitting potentials of the solution-treated samples were inversely proportional to the volume fraction and radius of the formed ordered particles, which had a stronger resistance to pitting corrosion. Recently, it was shown that two novel HEAs (AlCoFeNiSm<sub>0.1</sub>TiV<sub>0.9</sub> and AlCoFeNiSm<sub>0.1</sub>V<sub>0.9</sub>) fabricated by SLM also exhibit excellent corrosion resistance as revealed by potentiodynamic polarization tests and electrochemical impedance spectroscopy analysis [96]. High-temperature corrosion behaviors of these two HEAs were also studied by Sarkar et al. [146], which was tested in corrosive syngas (CO<sub>2</sub>, CO, H<sub>2</sub>, CH<sub>4</sub>, H<sub>2</sub>S) to explore their applicability in such harsh environments. The results showed that there were neither major surface cracks nor Kirkendall porosity across the cross section of the HEA sample after enduring corrosion atmospheres, while globule-like deposits of Ti-rich phases were observed, indicating the likelihood of the formation of Laves phases.

### 5.2. Oxidation behaviors of additive manufactured HEAs

Additive manufactured HEAs, especially the HEAs with refractory metal elements, can be potentially applied in various high temperature environments, where the oxidation behavior of the HEAs becomes very important. Cyclic oxidation studies of the LMDed AlCoCrFeNi HEA with different Al concentrations were performed at a temperature of 1100 °C for 200 h by Mohanty et al. [117]. Both the Al<sub>0.3</sub>CoCrFeNi and Al<sub>0.7</sub>CoCrFeNi HEAs displayed a parabolic oxide growth after the initial transition stage. A higher mass gain for Al<sub>0.3</sub>CoCrFeNi than that for Al<sub>0.7</sub>CoCrFeNi was observed over the entire duration. An external Cr<sub>2</sub>O<sub>3</sub> scale with Al<sub>2</sub>O<sub>3</sub> subscale beneath was formed on each oxidized HEA sample, while the thickness and continuity of the oxide layer varied with the Al content. A continuous Al<sub>2</sub>O<sub>3</sub> scale was formed on the Al<sub>0.7</sub>CoCrFeNi sample, and the thickness increased with the extension of the oxidation duration, thus led to enhanced oxidation resistance. The oxidation kinetics of LMD-built CoCrFeMnNi HEA followed the parabolic growth law within the 800–1000 °C temperature range, where an increased mass gain was observed with increased temperature [201]. Different oxide scale compositions were detected after different oxidation temperatures, namely

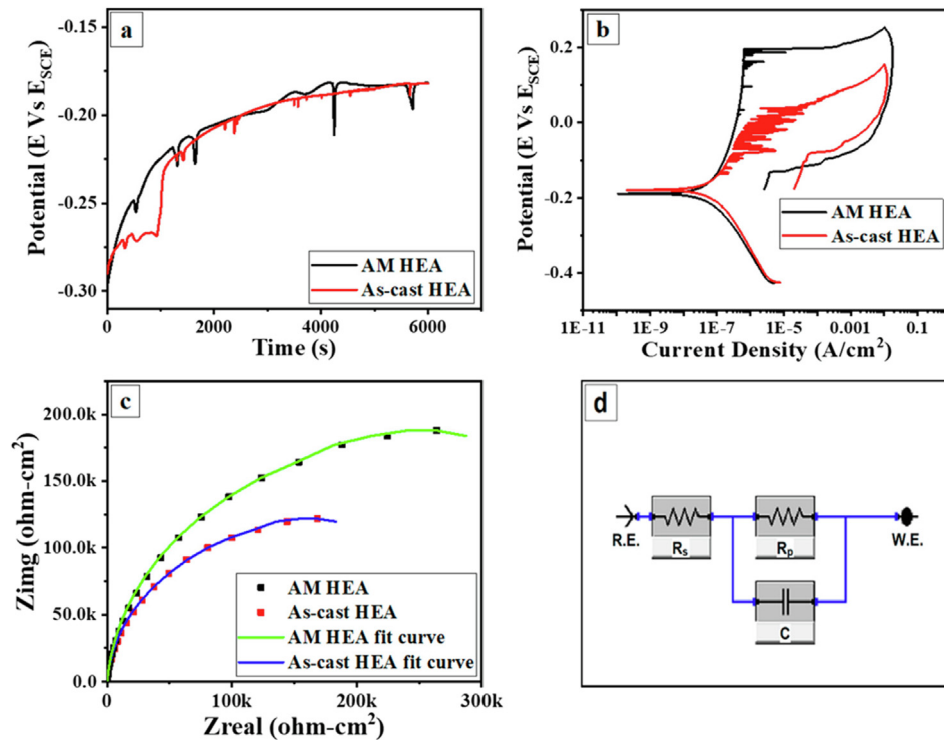


**Fig. 28.** Electrochemical corrosion behavior of SLM and as-cast HEA: (a) Open-circuit potential, (b) cyclic potentiodynamic polarization curves, (c) Nyquist plot and (d) the equivalent circuit used for fitting experimental data. Reproduced with permission [189]. Copyright 2019 The Authors.

$\text{Mn}_2\text{O}_3$  and  $\text{Cr}_2\text{O}_3$  at  $800\text{ }^\circ\text{C}$  while  $\text{Mn}_3\text{O}_4$  and  $(\text{Mn,Cr})_3\text{O}_4$  at  $900\text{ }^\circ\text{C}$  and  $1000\text{ }^\circ\text{C}$ . Based on the experimental results, the authors established the high-temperature oxidation mechanisms of this LMD HEA at different temperatures, and the corresponding schematic diagrams are shown in Fig. 29. It was concluded that the rapid outward diffusion of Mn and Cr along the dendrite grain boundaries with the inward diffusion of oxygen significantly affected the high-temperature oxidation behaviors of this additive manufactured HEA.

### 5.3. Magnetic properties of additive manufactured HEAs

It has been expected that HEAs may possess outstanding magnetic properties, which can be strongly affected by the element composition. Borkar et al. [5] studied the magnetic properties of  $\text{Al}_x\text{CrCuFeNi}_2$  ( $0 < x < 1.5$ ) HEAs fabricated by LMD, as shown in Fig. 30. It was found that the FCC/ $L1_2$  regions with low Al contents were weakly ferromagnetic, while the Al-rich BCC/B2 regions were ferromagnetic with high saturation magnetization, but being relatively soft with low coercivity. When  $x = 1.3$ , the saturation magnetization and coercivity reached the maximum values, suggesting that the magnetic properties in this HEAs system can be tuned by a paramagnetic element. In another work by Borkar et al. [122], the magnetic properties of  $\text{AlCo}_x\text{Cr}_{1-x}\text{FeNi}$  ( $0 < x < 1$ ) HEAs were investigated. The results showed that the saturation magnetization monotonically increased 6 times from  $18.48\text{ emu}\cdot\text{g}^{-1}$  of  $\text{AlCrFeNi}$  ( $x = 0$ ) to  $117.8\text{ emu}\cdot\text{g}^{-1}$  of  $\text{AlCoFeNi}$  ( $x = 1$ ), while the change in coercivity was non-monotonic, increasing by 7 times from  $\text{AlCrFeNi}$  ( $x = 0$ ) to  $\text{AlCo}_{0.4}\text{Cr}_{0.6}\text{FeNi}$  ( $x = 0.4$ ), and then decreasing by 14 times from  $\text{AlCo}_{0.4}\text{Cr}_{0.6}\text{FeNi}$  ( $x = 0.4$ ) to  $\text{AlCoFeNi}$  ( $x = 1$ ). The magnetic phase transition temperature for these HEAs showed a monotonic increasing trend with the increase of the Co content, and a secondary phase transition occurred in the composition range between  $x = 0.6$  to  $x = 0.8$ .

### 5.4. Hydrogen storage in additive manufactured HEAs

Hydrogen is regarded as a renewable and sustainable solution to reduce fossil fuels consumption. However, its possible applications are still limited by the development of suitable storage materials [49]. Some works have demonstrated that the Laves phase related BCC solid solution alloys exhibit a large hydrogen capacity and fast hydrogen absorption and desorption kinetics at room temperature, which opens a new research field on hydrogen storage materials [307,308]. Many HEAs systems can ensure the BCC solid solution structure by properly combining the alloying elements, thus providing a broad opportunity for the discovery of new metal hydrides with excellent hydrogen storage properties [49,88,309,310].

Kunce et al. [88,270] applied LMD to synthesize  $\text{CrFeNiTiVZr}$  and  $\text{MoNbTiVZr}$  HEAs from elemental powders for hydrogen storage purposes through pressure-composition-temperature tests. The compositions were selected based on their ability to form intermetallic phases, which were steady when exposed to hydrogen. The results showed that both HEAs could absorb and desorb hydrogen and the obtained maximum hydrogen capacity was 1.56 wt.% and 2.3 wt.%, respectively. The structure of these HEAs changed a lot after hydrogenation. A BCC  $\text{NbH}_{\sim 0.4}$ -type phase, an FCC  $\delta\text{TiH}_x$ -type phase and an  $\alpha\text{Zr}$  enriched phase for  $\text{MoNbTiVZr}$  HEA system could be observed, suggesting that Ti and Nb had absorbed the hydrogen [270]. However, in the context of this experiment device, the fabricated HEAs were unable to completely desorb hydrogen due to its low equilibrium pressure. The hydrogen absorption/desorption isotherms for LMD-produced  $\text{FeLaMnNiV}$  HEA are presented in Fig. 31, where the increase in the sample number corresponds to an increase in the La content in the sample. The maximum hydrogen capacity was found to be proportional to the atomic content of La element, as La is able to form  $\text{La}(\text{Ni,Mn})_5$  phase which exhibited very low equilibrium hydrogen desorption pressure [260]. Still, HEAs are typically not solely based

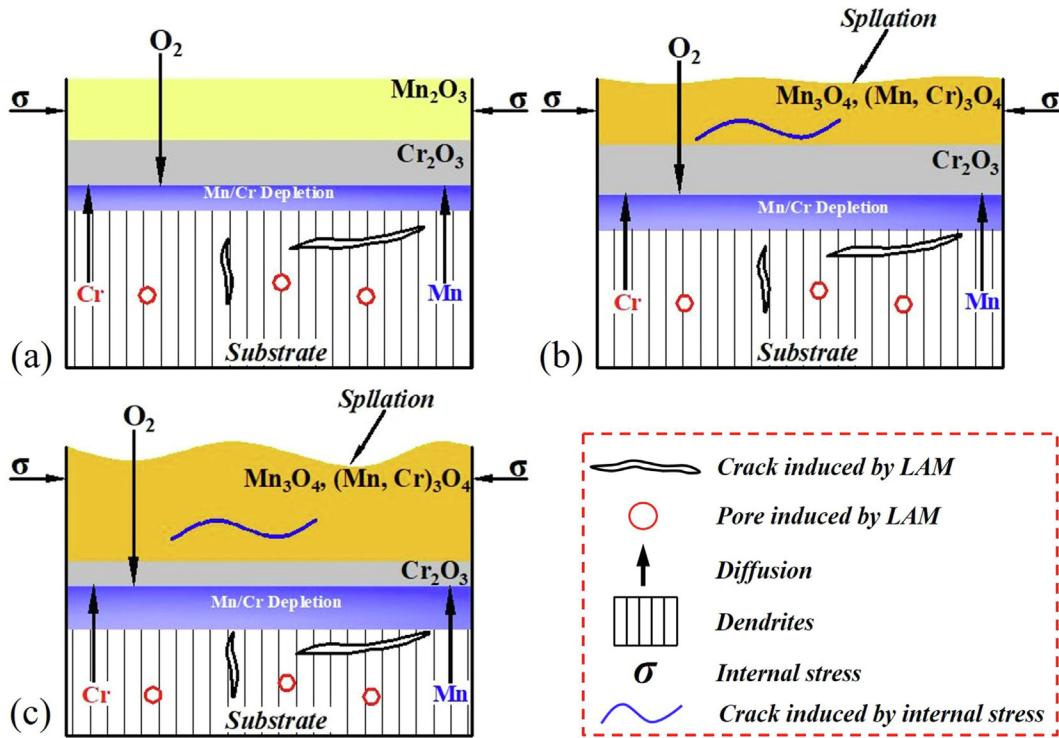


**Fig. 29.** Schematic diagrams of the high-temperature oxidation mechanisms of LMD-built CoCrFeMnNi HEA at different temperatures: (a) 800 °C, (b) 900 °C and (c) 1000 °C. Reproduced with permission [201]. Copyright 2020 Elsevier.

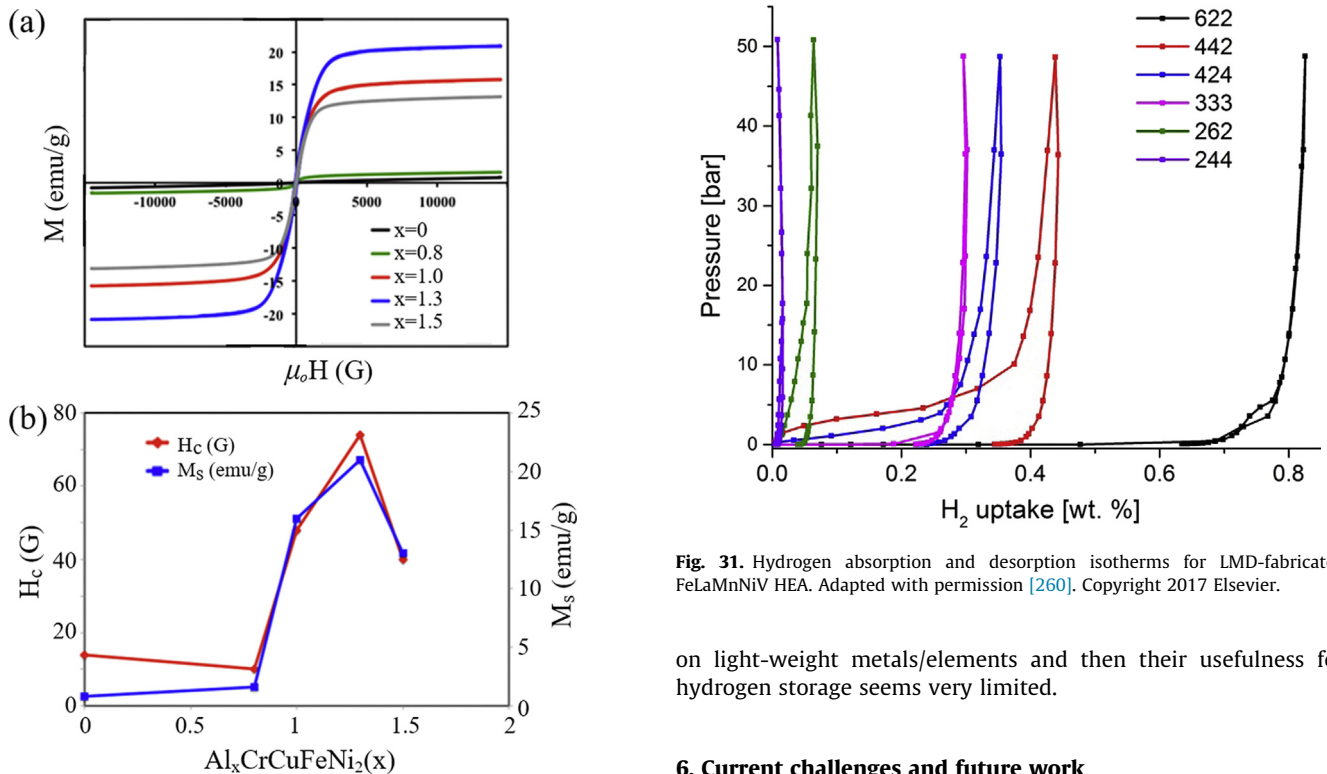


**Fig. 30.** Magnetic properties of LMD-fabricated  $Al_xCrCuFeNi_2(x)$  HEA: (a) Magnetizations (M)-magnetic field (H) curves, (b) coercivity ( $H_c$ ) and saturation magnetization ( $M_s$ ). Adapted with permission [5]. Copyright 2016 Elsevier.

**Fig. 31.** Hydrogen absorption and desorption isotherms for LMD-fabricated FeLaMnNiV HEA. Adapted with permission [260]. Copyright 2017 Elsevier.

on light-weight metals/elements and then their usefulness for hydrogen storage seems very limited.

**6. Current challenges and future work**

Up to now, many studies have been conducted on AM HEAs, however, there are still some challenges in this field, such as the

densification, cracks and residual stresses, dimensional accuracy and surface finish, chemical homogeneity, crystallization and microstructure control, performance anisotropy, etc. Therefore, further work should be carried out to broaden the knowledge of this new family of metallic materials through AM techniques. In this section, some ideas will be introduced to provide some possible research lines for the improvement and innovation in AM HEAs.

### 6.1. New HEAs

From the previous analysis, it can be seen that the HEA systems currently applied in the field of AM are limited, mainly the powder materials with the similar compositions for conventional manufacturing technologies. Thus, it is important and necessary to design and develop new HEAs systems especially for this advanced manufacturing technology [36]. Multiple factors need to be considered in the design of such alloy in order to obtain the desired properties of the AM processed parts, such as the laser absorptivity, melting temperature, flowability, vapor pressure, thermal stability and resistance towards crack formation of each element. It has been demonstrated that promising HEAs with unequal molar components generally have better performance [5]. The low availability of pre-alloyed powders for new perspective HEAs is one of the factors severely limiting the development of powder bed AM, especially refractory metallic materials [160]. Instead, materials research and development of compositional gradients and in-situ alloying, which potentially allow the use of elemental powder mixtures as raw materials for producing HEAs, not only save costs but also maximize the flexibility of tuning chemical composition. The fabrication of compositionally graded materials also allows the content of one or more elements to be varied within the same HEA system for efficient testing and screening. The initial properties of the powder have an important influence on the built parts during the AM processes. Therefore, it is crucial to investigate effective methods for blending the powders to reduce agglomeration and enhance homogeneity. It is also essential to develop substitutional elements and interstitial elements by extending the thermodynamic database and high-throughput screening of bulk specimens, which could be a guideline for selecting a suitable set of reinforcement compositions and designing AM products suitable for complex service environments [47,60,68,196]. Moreover, some subsets of the HEAs, like CoCrNi and CoNiV, which can be categorized into medium entropy alloys (MEAs), have also exhibited superior properties [311–318], indicating a promising research direction for AM techniques with high performance as well as cost-saving manufacturing of alloy powders.

### 6.2. Process development and optimization

In order to obtain the optimized structure and performance, the AM process of HEA can be further improved in the following ways. In-depth understanding of the synthesis principle and forming process, the control of residual stress and distortion during the manufacturing process, the reproducibility of the microstructure and properties of the processed alloys, the investigation of fracture toughness and fatigue properties, the need for reducing the anisotropy, the prevention of the metallurgical defects within the fabricated components, non-destructive tests for the components as well as the standard preparation protocols of the additive manufactured HEAs [38,292]. Especially in the case of non-destructive tests of the additive manufactured parts, it is necessary to explore in-situ monitoring systems to perform non-destructive evaluation during the AM process, so that defects can be detected early. Furthermore, the materials-related parameters, such as particle shape and size, phase formation, flowability and surface state of powders are important factors for the AM process and properties of the pro-

duced parts and, therefore, the influence of powder characteristics remains to be sufficiently explored [62]. Overall, it is essential to develop common metrology, process feedback and control procedures into the AM of HEAs to comply with the industrial specifications.

### 6.3. Thermodynamic modeling

Most of the current research on AM of HEAs is essentially a trial-and-error process, which is time-consuming and expensive. Only a few studies have used some kind of thermodynamical calculations, such as Thermo-Calc in the CoCrFeMnNi [186] and AlxCoCrFeNi HEA system [64], CALPHAD thermodynamic simulations in AlCrMnNbTa HEA [161], the combination of equilibrium CALPHAD simulation and non-equilibrium Scheil calculation in CoCrFeMnNi system [196], and an integrated computational materials engineering framework coupled with thermo-kinetic simulations in CoCrFeNiW [253], to predict the microstructure evolution during the AM process. For AM process of HEA, information about the particle size of the fabricated parts and the detailed phase compositions of desired phases such as a specific BCC or FCC phase, or undesired phases such as  $\sigma$  phase, carbides or intermetallic compounds, the kinetics of the phase transformations, the melting point of any HEAs system, the dimensional behavior with temperature and the possibly undesirable oxidation process are all necessary to be studied and analyzed with thermodynamic analysis technologies before investigating them experimentally [49]. It is crucial to compile a trustworthy database thoroughly for modelling the thermodynamics of the phase diagram, in order to accurately predict the appearing phase constituents and thereby control the microstructures [196]. This will allow us to work with comprehensive thermodynamic data as well as expand and improve the database in the future, advancing the design science of additive manufactured HEAs materials. In addition, considering that most of the AM techniques feature a very small interaction volume between the heat source and powders within a very short time, combined with a variety of parameters related to material properties and metallurgical processes, making the observation and characterization of different regions within the molten pool very difficult based on current experimental technologies. In order to solve this problem, comprehensive analysis and numerical simulation methods involving computational materials engineering, machine learning techniques and artificial intelligence, computer vision and data mining should be considered and introduced into this promising research field [36,48,319,320].

### 6.4. Innovative AM technique for HEAs

Except for the AM techniques mentioned above, 3D ink-extrusion AM, a non-beam approach, has also been recently applied to fabricate CoCrFeNi HEA micro-lattices by a blend of oxide nanopowders as shown in Fig. 32 [321], and the produced sample showed excellent mechanical properties at both ambient temperature and cryogenic temperature. By combining thermal sintering, Peng et al. [322] also applied this ink-extrusion method to fabricate a 3D-architected CoCrFeMnNi HEA, which exhibited exceptional energy absorption capacity. Besides, the binder jetting followed by sintering has also been applied to successfully synthesize the CoCrFeMnNi [323] and AlCoCrFeNi HEA [324]. The latter had a porosity of only about 1% [324]. Annealing experiments showed that higher annealing temperature generated an increase in the yield and fracture strength from 1203 MPa and 1996 MPa to 1461 MPa and 2272 MPa, respectively, attributed to the finer microstructure and higher elastic compatibility between BCC/B2 phases. Furthermore, powder plasma arc AM and powder-bed arc AM, another two promising arc-based AM methods were also

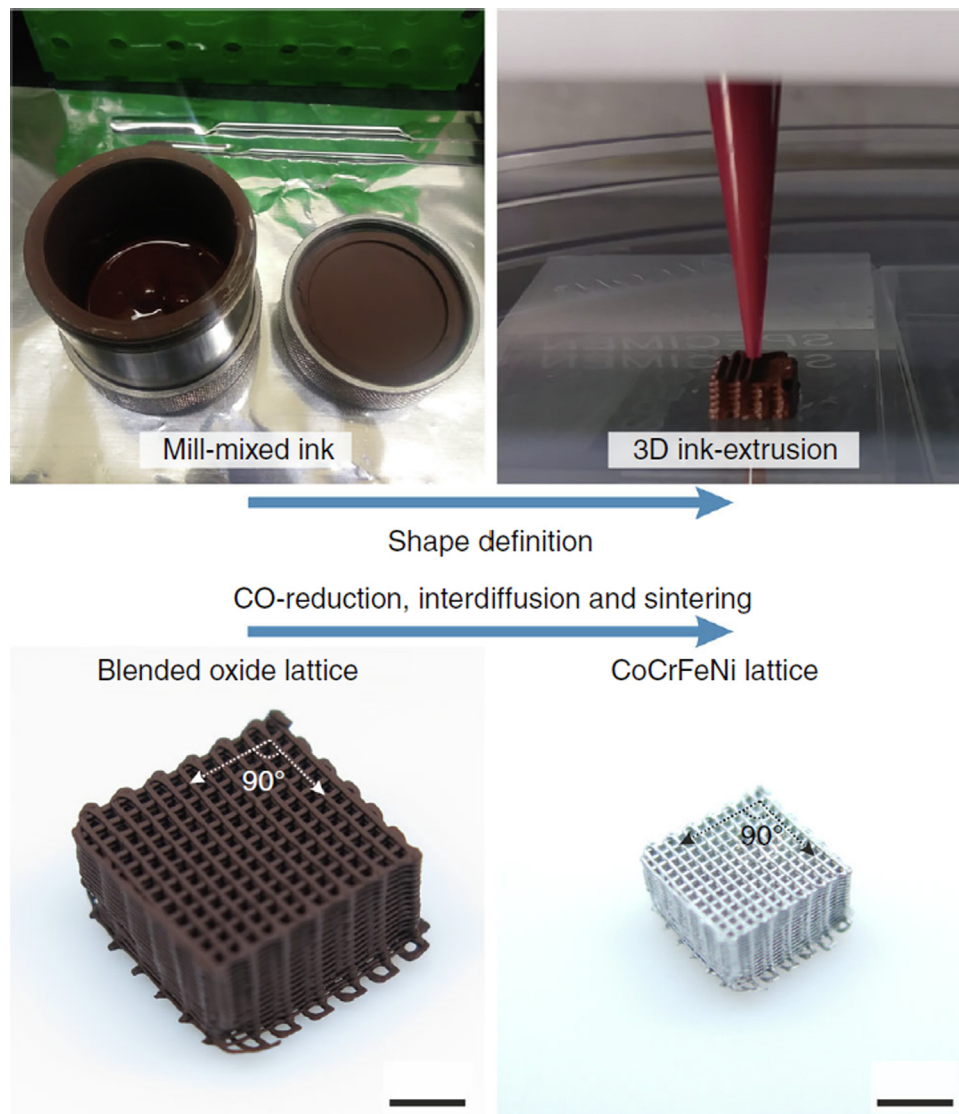


**Fig. 32.** The processing route of CoCrFeNi HEA micro-lattices by 3D ink-extrusion AM technique (scale bars are 3 mm). Adapted with permission [321]. Copyright 2019 The Authors.

applied recently to build HEAs [325–328]. These studies mentioned above suggested that novel AM methods could be used for fabricating HEAs in the future to explore potential superior microstructure and properties, which will further release the potential of AM technique itself for mass production in various industries.

## 7. Summary

A review on the current state of AM processed HEAs has been presented, focusing on microstructure characteristics and the related properties obtained by different AM processes. The large temperature gradients and rapid solidification rates involved in AM process usually result in fine-grained microstructures with superior properties. However, since the thermal conduction is anisotropic during AM processes with a notably higher value along the building direction, anisotropic microstructures with elongated grains are usually observed which consequently result in anisotropic properties. Both the microstructure and properties of the as-fabricated components can be tuned over a wide range by post-heat treatment. This review shows that the potential of AM HEAs is vast, and the obtained properties of the built HEAs derived from literatures are highly competitive with the cast or wrought

counterparts. Furthermore, this review also suggests that considerable further work, including new HEAs systems, process development and optimization, thermodynamic modeling and innovative AM techniques, still needs to be conducted to solve a series of scientific, technical and engineering problems, promoting the application of AM techniques in HEAs field.

### *CRediT authorship contribution statement*

**Wei Zhang:** Funding acquisition, Conceptualization, Methodology, Investigation, Data curation, Formal analysis, Visualization, Validation, Writing – original draft. **A. Chabok:** Writing – review & editing. **Bart J. Kooi:** Supervision, Writing – review & editing. **Yutao Pei:** Funding acquisition, Conceptualization, Methodology, Supervision, Writing – review & editing.

### **Declaration of Competing Interest**

The authors declare that they have no known competing financial interests or personal relationships that could have appeared to influence the work reported in this paper.

## Acknowledgement

Wei Zhang greatly thanks the China Scholarship Council (CSC, No. 201906250212) for her PhD Scholarship. This work was partially carried out under project number P16-46 Project 6 / S17024o in the framework of the Perspective Program of the Netherlands Organization for Scientific Research ([www.nwo.nl](http://www.nwo.nl)) and the Materials innovation institute M2i ([www.m2i.nl](http://www.m2i.nl)).

## Appendix A. Supplementary material

Supplementary data to this article can be found online at <https://doi.org/10.1016/j.matdes.2022.110875>.

## References

- J.W. Yeh, S.K. Chen, S.J. Lin, J.Y. Gan, T.S. Chin, T.T. Shun, S.H. Tsau, S.Y. Chang, Nanostructured high-entropy alloys with multiple principal elements: novel alloy design concepts and outcomes, *Adv. Eng. Mater.* 6 (2004) 299–303.
- B. Cantor, I.T.H. Chang, P. Knight, A.J.B. Vincent, Microstructural development in equiatomic multicomponent alloys, *Mater. Sci. Eng., A* 375–377 (2004) 213–218.
- Z. Wu, H. Bei, G.M. Pharr, E.P. George, Temperature dependence of the mechanical properties of equiatomic solid solution alloys with face-centered cubic crystal structures, *Acta Mater.* 81 (2014) 428–441.
- Y. Brif, M. Thomas, I. Todd, The use of high-entropy alloys in additive manufacturing, *Scr. Mater.* 99 (2015) 93–96.
- T. Borkar, B. Gwalani, D. Choudhuri, C.V. Mikler, C.J. Yannetta, X. Chen, R.V. Ramanujan, M.J. Styles, M.A. Gibson, R. Banerjee, A combinatorial assessment of  $\text{Al}_x\text{CrCuFeNi}_2$  ( $0 < x < 1.5$ ) complex concentrated alloys: microstructure, microhardness, and magnetic properties, *Acta Mater.* 116 (2016) 63–76.
- S.Y. Chen, Y. Tong, K.K. Tseng, J.W. Yeh, J.D. Poplawsky, J.G. Wen, M.C. Gao, G. Kim, W. Chen, Y. Ren, R. Feng, W.D. Li, P.K. Liaw, Phase transformations of HfNbTaTiZr high-entropy alloy at intermediate temperatures, *Scr. Mater.* 158 (2019) 50–56.
- R. Wang, Y. Tang, Z. Lei, Y. Ai, Z. Tong, S. Li, Y. Ye, S. Bai, Achieving high strength and ductility in nitrogen-doped refractory high-entropy alloys, *Mater. Des.* 213 (2022) 110356.
- K.V.S. Thurston, B. Gludovatz, A. Hohenwarter, G. Laplanche, E.P. George, R.O. Ritchie, Effect of temperature on the fatigue-crack growth behavior of the high-entropy alloy CrMnFeCoNi, *Intermetallics* 88 (2017) 65–72.
- D.G. Kim, Y.H. Jo, J.M. Park, W.M. Choi, H.S. Kim, B.J. Lee, S.S. Sohn, S. Lee, Effects of annealing temperature on microstructures and tensile properties of a single FCC phase CoCuMnNi high-entropy alloy, *J. Alloy Compd.* 812 (2020) 152111.
- M. Feuerbacher, M. Heidelmann, C. Thomas, Hexagonal high-entropy alloys, *Mater. Res. Lett.* 3 (1) (2015) 1–6.
- K.M. Youssef, A.J. Zaddach, C. Niu, D.L. Irving, C.C. Koch, A novel low-density, high-hardness, high-entropy alloy with close-packed single-phase nanocrystalline structures, *Mater. Res. Lett.* 3 (2) (2015) 95–99.
- M.C. Gao, B. Zhang, S.M. Guo, J.W. Qiao, J.A. Hawk, High-entropy alloys in hexagonal close-packed structure, *Metall. Mater. Trans. A* 47 (7) (2016) 3322–3332.
- Y. Zhang, T.T. Zuo, Z. Tang, M.C. Gao, K.A. Dahmen, P.K. Liaw, Z.P. Lu, Microstructures and properties of high-entropy alloys, *Prog. Mater. Sci.* 61 (2014) 1–93.
- D.B. Miracle, O.N. Senkov, A critical review of high entropy alloys and related concepts, *Acta Mater.* 122 (2017) 448–511.
- Y.J. Zhou, Y. Zhang, Y.L. Wang, G.L. Chen, Microstructure and compressive properties of multicomponent  $\text{Al}_x(\text{TiVCrMnFeCoNiCu})_{100-x}$  high-entropy alloys, *Mater. Sci. Eng., A* 454–455 (2007) 260–265.
- S.S. Nene, M. Frank, P. Agrawal, S. Sinha, K. Liu, S. Shukla, R.S. Mishra, B.A. McWilliams, K.C. Cho, Microstructurally flexible high entropy alloys: Linkages between alloy design and deformation behavior, *Mater. Des.* 194 (2020) 108968.
- P. Agrawal, S. Gupta, S. Shukla, S.S. Nene, S. Thapliyal, M.P. Toll, R.S. Mishra, Role of Cu addition in enhancing strength-ductility synergy in transforming high entropy alloy, *Mater. Des.* 215 (2022) 110487.
- Z. Qiu, C. Yao, K. Feng, Z. Li, P.K. Chu, Cryogenic deformation mechanism of CrMnFeCoNi high-entropy alloy fabricated by laser additive manufacturing process, *Int. J. Lightweight Mater. Manuf.* 1 (1) (2018) 33–39.
- S. Xiang, H. Luan, J. Wu, K.F. Yao, J. Li, X. Liu, Y. Tian, W. Mao, H. Bai, G. Le, Q. Li, Microstructures and mechanical properties of CrMnFeCoNi high entropy alloys fabricated using laser metal deposition technique, *J. Alloy Compd.* 773 (2019) 387–392.
- A.M. Giwa, Z.H. Aitken, P.K. Liaw, Y.W. Zhang, J.R. Greer, Effect of temperature on small-scale deformation of individual face-centered-cubic and body-centered-cubic phases of an  $\text{Al}_{0.7}\text{CoCrFeNi}$  high-entropy alloy, *Mater. Des.* 191 (2020) 108611.
- O.N. Senkov, J.M. Scott, S.V. Senkova, F. Meisenkothen, D.B. Miracle, C.F. Woodward, Microstructure and elevated temperature properties of a refractory TaNbHfZrTi alloy, *J. Mater. Sci.* 47 (9) (2012) 4062–4074.
- C. Lee, G. Song, M.C. Gao, R. Feng, P. Chen, J. Brechtel, Y. Chen, K. An, W. Guo, J. D. Poplawsky, S. Li, A.T. Samaei, W. Chen, A. Hu, H. Choo, P.K. Liaw, Lattice distortion in a strong and ductile refractory high-entropy alloy, *Acta Mater.* 160 (2018) 158–172.
- L.L. Xiao, Z.Q. Zheng, S.W. Guo, P. Huang, F. Wang, Ultra-strong nanostructured CrMnFeCoNi high entropy alloys, *Mater. Des.* 194 (2020) 108895.
- B.X. Cao, T. Yang, L. Fan, J.H. Luan, Z.B. Jiao, C.T. Liu, Refractory alloying additions on the thermal stability and mechanical properties of high-entropy alloys, *Mater. Sci. Eng., A* 797 (2020) 140020.
- Y. Shi, B. Yang, X. Xie, J. Brechtel, K.A. Dahmen, P.K. Liaw, Corrosion of  $\text{Al}_x\text{CoCrFeNi}$  high-entropy alloys: Al-content and potential scan-rate dependent pitting behavior, *Corros. Sci.* 119 (2017) 33–45.
- Y. Shi, B. Yang, P.D. Rack, S. Guo, P.K. Liaw, Y. Zhao, High-throughput synthesis and corrosion behavior of sputter-deposited nanocrystalline  $\text{Al}_x(\text{CoCrFeNi})_{100-x}$  combinatorial high-entropy alloys, *Mater. Des.* 195 (2020) 109018.
- W. Kai, F.P. Cheng, C.Y. Liao, C.C. Li, R.T. Huang, J.J. Kai, The oxidation behavior of the quinary FeCoNiCrSi $_x$  high-entropy alloys, *Mater. Chem. Phys.* 210 (2018) 362–369.
- B. Gorr, M. Azim, H.J. Christ, T. Mueller, D. Schliephake, M. Heilmair, Phase equilibria, microstructure, and high temperature oxidation resistance of novel refractory high-entropy alloys, *J. Alloy Compd.* 624 (2015) 270–278.
- M.H. Chuang, M.H. Tsai, W.R. Wang, S.J. Lin, J.W. Yeh, Microstructure and wear behavior of  $\text{Al}_x\text{Co}_{1.5}\text{CrFeNi}_{1.5}\text{Ti}_y$  high-entropy alloys, *Acta Mater.* 59 (16) (2011) 6308–6317.
- J. Wang, Y. Chen, Y. Zhang, W. Dai, Q. Xu, W. Li, Y. Liu, Corrosion and slurry erosion wear performances of coaxial direct laser deposited CoCrFeNiCu $_1$ -xMox high-entropy coatings by modulating the second-phase precipitation, *Mater. Des.* 212 (2021) 110277.
- M.A. Hemphill, T. Yuan, G.Y. Wang, J.W. Yeh, C.W. Tsai, A. Chuang, P.K. Liaw, Fatigue behavior of  $\text{Al}_{0.5}\text{CoCrCuFeNi}$  high entropy alloys, *Acta Mater.* 60 (16) (2012) 5723–5734.
- Z. Tang, T. Yuan, C.W. Tsai, J.W. Yeh, C.D. Lundin, P.K. Liaw, Fatigue behavior of a wrought  $\text{Al}_{0.5}\text{CoCrCuFeNi}$  two-phase high-entropy alloy, *Acta Mater.* 99 (2015) 247–258.
- K. Liu, M. Komarasamy, B. Gwalani, S. Shukla, R.S. Mishra, Fatigue behavior of ultrafine grained triplex  $\text{Al}_{0.3}\text{CoCrFeNi}$  high entropy alloy, *Scr. Mater.* 158 (2019) 116–120.
- J. Joseph, T. Jarvis, X. Wu, N. Stanford, P. Hodgson, D.M. Fabijanic, Comparative study of the microstructures and mechanical properties of direct laser fabricated and arc-melted  $\text{Al}_x\text{CoCrFeNi}$  high entropy alloys, *Mater. Sci. Eng., A* 633 (2015) 184–193.
- C. Yang, H. Bian, K. Aoyagi, Y. Hayasaka, K. Yamanaka, A. Chiba, Synergetic strengthening in HfMoNbTaTi refractory high-entropy alloy via disordered nanoscale phase and semicoherent refractory particle, *Mater. Des.* 212 (2021) 110248.
- X. Li, Additive manufacturing of advanced multi-component alloys: bulk metallic glasses and high entropy alloys, *Adv. Eng. Mater.* 20 (5) (2018) 1700874.
- C.M. Lin, H.L. Tsai, Evolution of microstructure, hardness, and corrosion properties of high-entropy  $\text{Al}_{0.5}\text{CoCrFeNi}$  alloy, *Intermetallics* 19 (3) (2011) 288–294.
- N. Li, S. Huang, G. Zhang, R. Qin, W. Liu, H. Xiong, G. Shi, J. Blackburn, Progress in additive manufacturing on new materials: a review, *J. Mater. Sci. Technol.* 35 (2) (2019) 242–269.
- P.E.J. Rivera-Diaz-del-Castillo, H. Fu, Strengthening mechanisms in high-entropy alloys: perspectives for alloy design, *J. Mater. Res.* 33 (19) (2018) 2970–2982.
- P.K. Gokuldoss, S. Kolla, J. Eckert, Additive manufacturing processes: selective laser melting, electron beam melting and binder jetting-selection guidelines, *Materials* 10 (6) (2017) 672.
- J.H. Martin, B.D. Yahata, J.M. Hundley, J.A. Mayer, T.A. Schaedler, T.M. Pollock, 3D printing of high-strength aluminium alloys, *Nature* 549 (7672) (2017) 365–369.
- G. Sander, J. Tan, P. Balan, O. Gharbi, D.R. Feenstra, L. Singer, S. Thomas, R.G. Kelly, J.R. Scully, N. Birbilis, Corrosion of additively manufactured alloys: a review, *Corrosion* 74 (12) (2018) 1318–1350.
- B. Wu, Z. Pan, D. Ding, D. Cuiuri, H. Li, J. Xu, J. Norrish, A review of the wire arc additive manufacturing of metals: properties, defects and quality improvement, *J. Manuf. Processes* 35 (2018) 127–139.
- D. Herzog, V. Seyda, E. Wycisk, C. Emmelmann, Additive manufacturing of metals, *Acta Mater.* 117 (2016) 371–392.
- M. Opprecht, J.P. Garandet, G. Roux, C. Flament, M. Soulier, A solution to the hot cracking problem for aluminium alloys manufactured by laser beam melting, *Acta Mater.* 197 (2020) 40–53.
- A. Piglione, B. Dovggy, C. Liu, C.M. Gourlay, P.A. Hooper, M.S. Pham, Printability and microstructure of the CoCrFeMnNi high-entropy alloy fabricated by laser powder bed fusion, *Mater. Lett.* 224 (2018) 22–25.
- S. Ewald, F. Kies, S. Hermsen, M. Voshage, C. Haase, J.H. Schlieffenbaum, Rapid alloy development of extremely high-alloyed metals using powder blends in laser powder bed fusion, *Materials* 12 (10) (2019) 1706.
- S.L. Sing, W.Y. Yeong, Laser powder bed fusion for metal additive manufacturing: perspectives on recent developments, *Virtual Phys. Prototyping* 15 (3) (2020) 359–370.

- [49] J.M. Torralba, P. Alvaredo, A. García-Junceda, High-entropy alloys fabricated via powder metallurgy. A critical review, *Powder Metall.* 62 (2) (2019) 84–114.
- [50] B.A. Welk, R.E.A. Williams, G.B. Viswanathan, M.A. Gibson, P.K. Liaw, H.L. Fraser, Nature of the interfaces between the constituent phases in the high entropy alloy CoCrCuFeNiAl, *Ultramicroscopy* 134 (2013) 193–199.
- [51] I. Kuncce, M. Polanski, K. Karczewski, T. Plocinski, K.J. Kurzydowski, Microstructural characterisation of high-entropy alloy AlCoCrFeNi fabricated by laser engineered net shaping, *J. Alloy Compd.* 648 (2015) 751–758.
- [52] J. Joseph, N. Stanford, P. Hodgson, D.M. Fabijanic, Tension/compression asymmetry in additive manufactured face centered cubic high entropy alloy, *Scr. Mater.* 129 (2017) 30–34.
- [53] R. Wang, K. Zhang, C. Davies, X. Wu, Evolution of microstructure, mechanical and corrosion properties of AlCoCrFeNi high-entropy alloy prepared by direct laser fabrication, *J. Alloy Compd.* 694 (2017) 971–981.
- [54] H. Dobbelsstein, M. Thiele, E.L. Gurevich, E.P. George, A. Ostendorf, Direct metal deposition of refractory high entropy alloy MoNbTaW, *Physics Procedia* 83 (2016) 624–633.
- [55] V. Ocelik, N. Janssen, S.N. Smith, J.T.M. De Hosson, Additive manufacturing of high-entropy alloys by laser processing, *JOM* 68 (7) (2016) 1810–1818.
- [56] S.M. Thompson, L. Bian, N. Shamsaei, A. Yadollahi, An overview of direct laser deposition for additive manufacturing; part I: transport phenomena, modeling and diagnostics, *Addit. Manuf.* 8 (2015) 36–62.
- [57] M.A. Melia, S.R. Whetten, R. Puckett, M. Jones, M.J. Heiden, N. Argibay, A.B. Kustas, High-throughput additive manufacturing and characterization of refractory high entropy alloys, *Appl. Mater. Today* 19 (2020) 100560.
- [58] J.T. Moon, E.J. Schindelholz, M.A. Melia, A.B. Kustas, D. Chidambaram, Corrosion of additively manufactured CoCrFeMnNi high entropy alloy in molten NaNO<sub>3</sub>-KNO<sub>3</sub>, *J. Electrochem. Soc.* 167 (8) (2020) 081509.
- [59] Z. Tong, H. Liu, J. Jiao, W. Zhou, Y. Yang, X. Ren, Improving the strength and ductility of laser directed energy deposited CrMnFeCoNi high-entropy alloy by laser shock peening, *Addit. Manuf.* 35 (2020) 101417.
- [60] S. Chen, Y. Tong, P. Liaw, Additive manufacturing of high-entropy alloys: a review, *Entropy* 20 (12) (2018) 937.
- [61] V. Pejaković, L.M. Berger, S. Thiele, H. Rojacz, M.R. Ripoll, Fine grained titanium carbonitride reinforcements for laser deposition processes of 316L boost tribocorrosion resistance in marine environments, *Mater. Des.* 207 (2021) 109847.
- [62] S. Gorsse, C. Hutchinson, M. Goune, R. Banerjee, Additive manufacturing of metals: a brief review of the characteristic microstructures and properties of steels, Ti-6Al-4V and high-entropy alloys, *Sci. Technol. Adv. Mater.* 18 (1) (2017) 584–610.
- [63] H. Knoll, S. Ocylok, A. Weisheit, H. Springer, E. Jäggle, D. Raabe, Combinatorial alloy design by laser additive manufacturing, *Steel Res. Int.* 88 (8) (2017) 1600416.
- [64] K. Kuwabara, H. Shiratori, T. Fujieda, K. Yamanaka, Y. Koizumi, A. Chiba, Mechanical and corrosion properties of AlCoCrFeNi high-entropy alloy fabricated with selective electron beam melting, *Addit. Manuf.* 23 (2018) 264–271.
- [65] T. Fujieda, H. Shiratori, K. Kuwabara, M. Hirota, T. Kato, K. Yamanaka, Y. Koizumi, A. Chiba, S. Watanabe, CoCrFeNiTi-based high-entropy alloy with superior tensile strength and corrosion resistance achieved by a combination of additive manufacturing using selective electron beam melting and solution treatment, *Mater. Lett.* 189 (2017) 148–151.
- [66] F. Xiong, C. Huang, O.L. Kafka, Y. Lian, W. Yan, M. Chen, D. Fang, Grain growth prediction in selective electron beam melting of Ti-6Al-4V with a cellular automaton method, *Mater. Des.* 199 (2021) 109410.
- [67] T. Fujieda, H. Shiratori, K. Kuwabara, T. Kato, K. Yamanaka, Y. Koizumi, A. Chiba, First demonstration of promising selective electron beam melting method for utilizing high-entropy alloys as engineering materials, *Mater. Lett.* 159 (2015) 12–15.
- [68] R. Piticescu, A. Katz-Demyanetz, V.V. Popov, A. Kovalevsky, D. Safranchik, A. Koptug, I. Vlaicu, Powder-bed additive manufacturing for aerospace application: techniques, metallic and metal/ceramic composite materials and trends, *Manuf. Rev.* 6 (2019) 5.
- [69] D. Jafari, T.H.J. Vaneker, I. Gibson, Wire and arc additive manufacturing: Opportunities and challenges to control the quality and accuracy of manufactured parts, *Mater. Des.* 202 (2021) 109471.
- [70] X.Z. Chen, C.C. Su, Y.F. Wang, A.N. Siddiquee, K. Sergey, S. Jayalakshmi, R.A. Singh, Cold metal transfer (CMT) based wire and arc additive manufacture (WAAM) system, *Journal of Surface Investigation: X-ray, Synchrotron and Neutron, Techniques* 12 (2018) 1278–1284.
- [71] Q. Shen, X. Kong, X. Chen, Significant transitions of microstructure and mechanical properties in additively manufactured Al-Co-Cr-Fe-Ni high-entropy alloy under heat treatment, *Mater. Sci. Eng., A* 815 (2021) 141257.
- [72] Q. Shen, X. Kong, X. Chen, Fabrication of bulk Al-Co-Cr-Fe-Ni high-entropy alloy using combined cable wire arc additive manufacturing (CCW-AAM): Microstructure and mechanical properties, *J. Mater. Sci. Technol.* 74 (2021) 136–142.
- [73] Z. Lin, K. Song, X. Yu, A review on wire and arc additive manufacturing of titanium alloy, *J. Manuf. Processes* 70 (2021) 24–45.
- [74] N.A. Rosli, M.R. Alkahari, F.R. Ramli, S. Mat, A.A. Yusof, Influence of process parameters on dimensional accuracy in GMAW based additive manufacturing, *Proc. Mech. Eng. Res. Day* 2019 (2019) 7–9.
- [75] D. Ding, Z. Pan, D. Cuiuri, H. Li, A practical path planning methodology for wire and arc additive manufacturing of thin-walled structures, *Robot. Comput.-Int. Manuf.* 34 (2015) 8–19.
- [76] F. Leijon, S. Wachter, Z. Fu, C. Körner, S. Skjervold, J. Moverare, A novel rapid alloy development method towards powder bed additive manufacturing, demonstrated for binary Al-Ti, -Zr and -Nb alloys, *Mater. Des.* 211 (2021) 110129.
- [77] R.S. Mishra, S. Thapliyal, Design approaches for printability-performance synergy in Al alloys for laser-powder bed additive manufacturing, *Mater. Des.* 204 (2021) 109640.
- [78] Q. Chao, T. Guo, T. Jarvis, X. Wu, P. Hodgson, D. Fabijanic, Direct laser deposition cladding of Al<sub>x</sub>CoCrFeNi high entropy alloys on a high-temperature stainless steel, *Surf. Coat. Technol.* 332 (2017) 440–451.
- [79] H. Zhang, Y.Z. He, Y. Pan, Y.S. He, K.S. Shin, Synthesis and characterization of NiCoFeCrAl<sub>3</sub> high entropy alloy coating by laser cladding, *Adv. Mater. Res.* 97–101 (2010) 1408–1411.
- [80] X. Ye, M. Ma, W. Liu, L. Li, M. Zhong, Y. Liu, Q. Wu, Synthesis and characterization of high-entropy alloy FeCoNiCuCr by laser cladding, *Adv. Mater. Sci. Eng.* 2011 (2011) 1–7.
- [81] X. Ye, M. Ma, Y. Cao, W. Liu, X. Ye, Y. Gu, The property research on high-entropy alloy Al<sub>x</sub>FeCoNiCuCr coating by laser cladding, *Physics Procedia* 12 (2011) 303–312.
- [82] W. Cui, W. Li, W.T. Chen, F. Liou, Laser metal deposition of an AlCoCrFeNiTi<sub>0.5</sub> high-entropy alloy coating on a Ti6Al4V substrate: microstructure and oxidation behavior, *Crystals* 10 (8) (2020) 638.
- [83] N. Malatji, A.P.I. Popoola, T. Lengopeng, S. Pityana, Tribological and corrosion properties of laser additive manufactured AlCrFeNiCu high entropy alloy, *Mater. Today: Proc.* 28 (2020) 944–948.
- [84] G. Prabu, M. Duraiselvam, N. Jayaprakash, C.H. Yang, Microstructural evolution and wear behavior of AlCoCrCuFeNi high entropy alloy on Ti-6Al-4V through laser surface alloying, *Met. Mater. Int.* 27 (2021) 2328–2340.
- [85] S. Yang, Z. Liu, J. Pi, Microstructure and wear behavior of the AlCrFeCoNi high-entropy alloy fabricated by additive manufacturing, *Mater. Lett.* 261 (2020) 127004.
- [86] J. Li, W. Craeghs, C. Jing, S. Gong, F. Shan, Microstructure and physical performance of laser-induction nanocrystals modified high-entropy alloy composites on titanium alloy, *Mater. Des.* 117 (2017) 363–370.
- [87] Y. Guo, X. Li, Q. Liu, A novel biomedical high-entropy alloy and its laser-clad coating designed by a cluster-plus-glue-atom model, *Mater. Design* (196) (2020) 109085.
- [88] I. Kuncce, M. Polanski, J. Bystrycki, Structure and hydrogen storage properties of a high entropy ZrTiVCrFeNi alloy synthesized using laser engineered net shaping (LENS), *Int. J. Hydrogen Energy* 38 (27) (2013) 12180–12189.
- [89] J. Kim, A. Wakai, A. Moridi, Materials and manufacturing renaissance: additive manufacturing of high-entropy alloys, *J. Mater. Res.* 35 (15) (2020) 1963–1983.
- [90] A.O. Moghaddam, N.A. Shaburova, M.N. Samodurova, A. Abdollahzadeh, E.A. Trofimov, Additive manufacturing of high entropy alloys: a practical review, *J. Mater. Sci. Technol.* 77 (2020) 131–162.
- [91] C. Zhang, J. Zhu, H. Zheng, H. Li, S. Liu, G.J. Cheng, A review on microstructures and properties of high entropy alloys manufactured by selective laser melting, *Int. J. Extreme Manuf.* 2 (3) (2020) 032003.
- [92] J.M. Torralba, M. Campos, High entropy alloys manufactured by additive manufacturing, *Metals* 10 (5) (2020) 639.
- [93] C. Han, Q. Fang, Y. Shi, S.B. Tor, C.K. Chua, K. Zhou, Recent advances on high-entropy alloys for 3D printing, *Adv. Mater.* 32 (26) (2020) 1903855.
- [94] H. Dobbelsstein, E.L. Gurevich, E.P. George, A. Ostendorf, G. Laplanche, Laser metal deposition of a refractory TiZrNbHfTa high-entropy alloy, *Addit. Manuf.* 24 (2018) 386–390.
- [95] H. Dobbelsstein, E.L. Gurevich, E.P. George, A. Ostendorf, G. Laplanche, Laser metal deposition of compositionally graded TiZrNbTa refractory high-entropy alloys using elemental powder blends, *Addit. Manuf.* 25 (2019) 252–262.
- [96] P.K. Sarswat, S. Sarkar, A. Murali, W. Huang, W. Tan, M.L. Free, Additive manufactured new hybrid high entropy alloys derived from the AlCoFeNiSmTiVZr system, *Appl. Surf. Sci.* 476 (2019) 242–258.
- [97] B. Gwalani, V. Soni, O.A. Waseem, S.A. Mantri, R. Banerjee, Laser additive manufacturing of compositionally graded AlCrFeMoV<sub>x</sub> (x = 0 to 1) high-entropy alloy system, *Opt. Laser Technol.* 113 (2019) 330–337.
- [98] K. Zhou, J. Li, L. Wang, H. Yang, Z. Wang, J. Wang, Direct laser deposited bulk CoCrFeNiNb<sub>x</sub> high entropy alloys, *Intermetallics* 114 (2019) 106592.
- [99] Y. Wang, R. Li, P. Niu, Z. Zhang, T. Yuan, J. Yuan, K. Li, Microstructures and properties of equimolar AlCoCrCuFeNi high-entropy alloy additively manufactured by selective laser melting, *Intermetallics* 120 (2020) 106746.
- [100] M. Dada, P. Popoola, N. Mathe, S. Pityana, S. Adeosun, O. Aramide, The comparative study of the microstructural and corrosion behaviour of laser-deposited high entropy alloys, *J. Alloy Compd.* 866 (2021) 158777.
- [101] D. Choudhuri, T. Alam, T. Borkar, B. Gwalani, A.S. Mantri, S.G. Srinivasan, M.A. Gibson, R. Banerjee, Formation of a Huesler-like L21 phase in a CoCrCuFeNiAlTi high-entropy alloy, *Scr. Mater.* 100 (2015) 36–39.
- [102] C.W. Li, K.C. Chang, A.C. Yeh, On the microstructure and properties of an advanced cemented carbide system processed by selective laser melting, *J. Alloy Compd.* 782 (2019) 440–450.
- [103] P. Sarswat, T. Smith, S. Sarkar, A. Murali, M. Free, Design and fabrication of new high entropy alloys for evaluating titanium replacements in additive manufacturing, *Materials* 13 (2020) 3001.

- [104] X. Gao, Z. Yu, W. Hu, Y. Lu, Z. Zhu, Y. Ji, Y. Lu, Z. Qin, X. Lu, In situ strengthening of CrMnFeCoNi high-entropy alloy with Al realized by laser additive manufacturing, *J. Alloy Compd.* 847 (2020) 156563.
- [105] F. Yang, L. Wang, Z. Wang, Q. Wu, K. Zhou, X. Lin, W. Huang, Ultra strong and ductile eutectic high entropy alloy fabricated by selective laser melting, *J. Mater. Sci. Technol.* 106 (2022) 128–132.
- [106] Z. Sun, X. Tan, C. Wang, M. Descroins, D. Mangelinck, S.B. Tor, E.A. Jäggle, S. Zaefferer, D. Raabe, Reducing hot tearing by grain boundary segregation engineering in additive manufacturing: example of an Al<sub>x</sub>CoCrFeNi high-entropy alloy, *Acta Mater.* 204 (2021) 116505.
- [107] F. Peyrouzet, D. Hachet, R. Soulas, C. Navone, S. Godet, S. Gorsse, Selective laser melting of Al<sub>0.3</sub>CoCrFeNi high-entropy alloy: printability, microstructure, and mechanical properties, *JOM* 71 (10) (2019) 3443–3451.
- [108] P.F. Zhou, D.H. Xiao, Z. Wu, X.Q. Ou, Al<sub>0.5</sub>FeCoCrNi high entropy alloy prepared by selective laser melting with gas-atomized pre-alloy powders, *Mater. Sci. Eng., A* 739 (2019) 86–89.
- [109] K. Sun, W. Peng, L. Yang, L. Fang, Effect of SLM processing parameters on microstructures and mechanical properties of Al<sub>0.5</sub>CoCrFeNi high entropy alloys, *Metals* 10 (2) (2020) 292.
- [110] J. Karimi, P. Ma, Y.D. Jia, K.G. Prashanth, Linear patterning of high entropy alloy by additive manufacturing, *Manuf. Lett.* 24 (2020) 9–13.
- [111] D. Karlsson, A. Marshal, F. Johansson, M. Schuisky, M. Sahlberg, J.M. Schneider, U. Jansson, Elemental segregation in an AlCoCrFeNi high-entropy alloy - A comparison between selective laser melting and induction melting, *J. Alloy Compd.* 784 (2019) 195–203.
- [112] P.D. Niu, R.D. Li, T.C. Yuan, S.Y. Zhu, C. Chen, M.B. Wang, L. Huang, Microstructures and properties of an equimolar AlCoCrFeNi high entropy alloy printed by selective laser melting, *Intermetallics* 104 (2019) 24–32.
- [113] J. Joseph, P. Hodgson, T. Jarvis, X. Wu, N. Stanford, D.M. Fabijanic, Effect of hot isostatic pressing on the microstructure and mechanical properties of additive manufactured Al<sub>x</sub>CoCrFeNi high entropy alloys, *Mater. Sci. Eng., A* 733 (2018) 59–70.
- [114] J. Joseph, N. Stanford, P. Hodgson, D.M. Fabijanic, Understanding the mechanical behaviour and the large strength/ductility differences between FCC and BCC Al<sub>x</sub>CoCrFeNi high entropy alloys, *J. Alloy Compd.* 726 (2017) 885–895.
- [115] L. Huang, Y. Sun, A. Amar, C. Wu, X. Liu, G. Le, X. Wang, J. Wu, K. Li, C. Jiang, J. Li, Microstructure evolution and mechanical properties of Al CoCrFeNi high-entropy alloys by laser melting deposition, *Vacuum* 183 (2021) 109875.
- [116] H.R. Sista, J.W. Newkirk, F. Frank Liou, Effect of Al/Ni ratio, heat treatment on phase transformations and microstructure of Al<sub>x</sub>FeCoCrNi<sub>2-x</sub> (x=0.3, 1) high entropy alloys, *Mater. Des.* 81 (2015) 113–121.
- [117] A. Mohanty, J.K. Sampreeth, O. Bembalge, J.Y. Hascoet, S. Marya, R.J. Immanuel, S.K. Panigrahi, High temperature oxidation study of direct laser deposited Al<sub>x</sub>CoCrFeNi (X=0.3,0.7) high entropy alloys, *Surf. Coat. Technol.* 380 (2019) 125028.
- [118] B. Gwalani, S. Gangireddy, S. Shukla, C.J. Yannetta, S.G. Valentin, R.S. Mishra, R. Banerjee, Compositionally graded high entropy alloy with a strong front and ductile back, *Mater. Today Commun.* 20 (2019) 100602.
- [119] M.S.K.K.Y. Nartu, T. Alam, S. Dasari, S.A. Mantri, S. Gorsse, H. Siller, N. Dahotre, R. Banerjee, Enhanced tensile yield strength in laser additively manufactured Al<sub>0.3</sub>CoCrFeNi high entropy alloy, *Materialia* 9 (2020) 100522.
- [120] H. Peng, S. Xie, P. Niu, Z. Zhang, T. Yuan, Z. Ren, X. Wang, Y. Zhao, R. Li, Additive manufacturing of Al<sub>0.3</sub>CoCrFeNi high-entropy alloy by powder feeding laser melting deposition, *J. Alloy Compd.* 862 (2021) 158286.
- [121] J. Joseph, M. Imran, P.D. Hodgson, M.R. Barnett, D.M. Fabijanic, Towards the large-scale production and strength prediction of near-eutectic Al<sub>x</sub>CoCrFeNi<sub>2,1</sub> alloys by additive manufacturing, *Manuf. Lett.* 25 (2020) 16–20.
- [122] T. Borkar, V. Chaudhary, B. Gwalani, D. Choudhuri, C.V. Mikler, V. Soni, T. Alam, R.V. Ramanujan, R. Banerjee, A combinatorial approach for assessing the magnetic properties of high entropy alloys: role of Cr in AlCo<sub>x</sub>Cr<sub>1-x</sub>FeNi, *Adv. Eng. Mater.* 19 (8) (2017) 1700048.
- [123] V. Chaudhary, T. Borkar, C.V. Mikler, B. Gwalani, D. Choudhuri, V. Soni, T. Alam, R.V. Ramanujan, R. Banerjee, Additively manufactured functionally graded FeNi based high entropy magnetic alloys, in: 2018 IEEE International Magnetics Conference.
- [124] Y. Zhu, S. Zhou, Z. Xiong, Y.-J. Liang, Y. Xue, L. Wang, Enabling stronger eutectic high-entropy alloys with larger ductility by 3D printed directional lamellae, *Addit. Manuf.* 39 (2021) 101901.
- [125] R.J. Vikram, B.S. Murty, D. Fabijanic, S. Suwas, Insights into micro-mechanical response and texture of the additively manufactured eutectic high entropy alloy AlCoCrFeNi<sub>2,1</sub>, *J. Alloy Compd.* 827 (2020) 154034.
- [126] S. Zhao, D. Xin, X. Chen, J. Stasic, M. Trtica, A.N. Siddiquee, S. Mohan, Microstructure and enhanced tensile properties of AlCo<sub>x</sub>CrFeNi high entropy alloys with high Co content fabricated by laser melting deposition, 2022. Available at SSRN: <https://ssrn.com/abstract=4002371>.
- [127] K. Zhou, J. Li, Q. Wu, Z. Zhang, Z. Wang, J. Wang, Remelting induced fully-equiaxed microstructures with anomalous eutectics in the additive manufactured Ni<sub>32</sub>Co<sub>30</sub>Cr<sub>10</sub>Fe<sub>10</sub>Al<sub>18</sub> eutectic high-entropy alloy, *Scr. Mater.* 201 (2021) 113952.
- [128] M. Zhang, J. Li, Y. Li, J. Wang, Z. Li, X. Cheng, Effect of Al addition on the microstructure and hardness of the (Al<sub>x</sub>CoCrFe)<sub>50</sub>Ni high-entropy alloy prepared by directed energy deposition technique, *Mater. Lett.* 285 (2021) 128778.
- [129] H. Shiratori, T. Fujieda, K. Yamanaka, Y. Koizumi, K. Kuwabara, T. Kato, A. Chiba, Relationship between the microstructure and mechanical properties of an equiatomic AlCoCrFeNi high-entropy alloy fabricated by selective electron beam melting, *Mater. Sci. Eng., A* 656 (2016) 39–46.
- [130] K. Yamanaka, H. Shiratori, M. Mori, K. Omura, T. Fujieda, K. Kuwabara, A. Chiba, Corrosion mechanism of an equimolar AlCoCrFeNi high-entropy alloy additively manufactured by electron beam melting, *npj Mater. Degrad.* 4 (1) (2020) 24.
- [131] K. Osintsev, S. Kononov, V. Gromov, I. Panchenko, Y. Ivanov, Microstructural and mechanical characterisation of non-equiaxiomatic Al<sub>2.1</sub>Co<sub>0.3</sub>Cr<sub>0.5</sub>FeNi<sub>2.1</sub> high-entropy alloy fabricated via wire-arc additive manufacturing, *Philos. Mag. Lett.* 101 (9) (2021) 353–359.
- [132] K.A. Osintsev, S.V. Kononov, A.M. Glezer, V.E. Gromov, Y.F. Ivanov, I.A. Panchenko, R.V. Sundeev, Research on the structure of Al<sub>2.1</sub>Co<sub>0.3</sub>Cr<sub>0.5</sub>FeNi<sub>2.1</sub> high-entropy alloy at submicro- and nano-scale levels, *Mater. Lett.* 294 (2021) 129717.
- [133] V. Gromov, Y. Ivanov, S. Kononov, K. Osintsev, A. Semin, Y. Rubannikova, Modification of high-entropy alloy AlCoCrFeNi by electron beam treatment, *J. Mater. Res. Technol.* 13 (2021) 787–797.
- [134] Y. Cai, L. Zhu, Y. Cui, J. Han, Manufacturing of FeCoCrNi + FeCoCrNiAl laminated high-entropy alloy by laser melting deposition (LMD), *Mater. Lett.* 289 (2021) 129445.
- [135] Y. Cai, X. Li, H. Xia, Y. Cui, S.M. Manladan, L. Zhu, M. Shan, D. Sun, T. Wang, X. Lv, J. Han, Fabrication of laminated high entropy alloys using differences in laser melting deposition characteristics of FeCoCrNi and FeCoCrNiAl, *J. Manuf. Processes* 72 (2021) 294–308.
- [136] W.C. Lin, Y.J. Chang, T.H. Hsu, S. Gorsse, F. Sun, T. Furuhashi, A.C. Yeh, Microstructure and tensile property of a precipitation strengthened high entropy alloy processed by selective laser melting and post heat treatment, *Addit. Manuf.* 36 (2020) 101601.
- [137] S. Guan, K. Solberg, D. Wan, F. Berto, T. Welo, T.M. Yue, K.C. Chan, Formation of fully equiaxed grain microstructure in additively manufactured AlCoCrFeNiTi<sub>0.5</sub> high entropy alloy, *Mater. Des.* 184 (2019) 108202.
- [138] S. Liu, D. Wan, S. Guan, Y. Fu, X. Ren, Z. Zhang, J. He, Microstructure and nanomechanical behavior of an additively manufactured (CrCoNiFe)<sub>94</sub>Ti<sub>2</sub>Al<sub>4</sub> high-entropy alloy, *Mater. Sci. Eng., A* 823 (2021) 141737.
- [139] M. Dada, P. Popoola, O. Aramide, N. Mathe, S. Pityana, Optimization of the corrosion property of a high entropy alloy using response surface methodology, *Mater. Today: Proc.* 38 (2021) 1024–1030.
- [140] S. Guan, D. Wan, K. Solberg, F. Berto, T. Welo, T.M. Yue, K.C. Chan, Additively manufactured CrMnFeCoNi/AlCoCrFeNiTi<sub>0.5</sub> laminated high-entropy alloy with enhanced strength-plasticity synergy, *Scr. Mater.* 183 (2020) 133–138.
- [141] Y. Yan, W.D. Song, K.F. Li, K. Zhao, T.T. Sun, K.K. Song, L.N. Hu, Microstructural features and mechanical behaviors of Al<sub>0.5</sub>Cr<sub>0.8</sub>CoFeNi<sub>2.5</sub>V<sub>0.2</sub> high-entropy alloys fabricated by selective laser melting technique, *Acta Metallurgica Sinica (Engl. Lett.)* (2022).
- [142] M. Zhang, X. Zhou, D. Wang, W. Zhu, J. Li, Y.F. Zhao, AlCoCuFeNi high-entropy alloy with tailored microstructure and outstanding compressive properties fabricated via selective laser melting with heat treatment, *Mater. Sci. Eng., A* 743 (2019) 773–784.
- [143] M.N. Zhang, X.L. Zhou, W.Z. Zhu, J.H. Li, Microstructure and mechanical behavior of AlCoCuFeNi high-entropy alloy fabricated by selective laser melting, in: SFF 2017: Proceedings of the 28th Annual International Solid Freeform Fabrication Symposium - An Additive Manufacturing Conference, 2017, pp. 725–732.
- [144] Y. Ren, L. Liang, Q. Shan, A. Cai, J. Du, Q. Huang, H. Wu, Effect of volumetric energy density on microstructure and tribological properties of FeCoNiCuAl high-entropy alloy produced by laser powder bed fusion, *Virtual Phys. Prototyping* 15 (sup1) (2020) 543–554.
- [145] X. Chen, L. Yan, S. Karnati, Y. Zhang, F. Liou, Fabrication and characterization of Al<sub>x</sub>CoFeNiCu<sub>1-x</sub> high entropy alloys by laser metal deposition, *Coatings* 7 (4) (2017) 47.
- [146] S. Sarkar, P.K. Sarswat, M.L. Free, Elevated temperature corrosion resistance of additively manufactured single phase AlCoFeNiTiV<sub>0.9</sub>Sm<sub>0.1</sub> and AlCoFeNiV<sub>0.9</sub>Sm<sub>0.1</sub> HEAs in a simulated syngas atmosphere, *Addit. Manuf.* 30 (2019) 100902.
- [147] H. Li, Y. Mu, G. Wang, Y. Jia, R. Wang, Effect of Annealing on irradiation resistance of (FeCoNi)<sub>86</sub>Al<sub>7</sub>Ti<sub>7</sub> high entropy alloys, *Mater. Lett.* 316 (2022) 131970.
- [148] N. Malatji, A.P.I. Popoola, T. Lengopeng, S. Pityana, Effect of Nb addition on the microstructure, mechanical and electrochemical characteristics of AlCrFeNiCu high-entropy alloy, *Int. J. Miner. Metall. Mater.* 27 (10) (2020) 1332–1340.
- [149] S. Luo, P. Gao, H. Yu, J. Yang, Z. Wang, X. Zeng, Selective laser melting of an equiatomic AlCrCuFeNi high-entropy alloy: processability, non-equilibrium microstructure and mechanical behavior, *J. Alloy Compd.* 771 (2019) 387–397.
- [150] S. Luo, Y. Su, Z. Wang, Microstructural evolution and mechanisms in additively manufactured AlCrCuFeNi<sub>x</sub> complex concentrated alloys via selective laser melting, *J. Alloy Compd.* 870 (2021) 159443.
- [151] Y. Su, S. Luo, Z. Wang, Microstructure evolution and cracking behaviors of additively manufactured Al<sub>x</sub>CrCuFeNi<sub>2</sub> high entropy alloys via selective laser melting, *J. Alloy Compd.* 842 (2020) 155823.
- [152] S. Luo, C. Zhao, H. Yang, Q. Liu, Z. Wang, X. Zeng, Selective laser melting of dual phase AlCrCuFeNi<sub>x</sub> high entropy alloys: formability, heterogeneous

- microstructures and deformation mechanisms, *Addit. Manuf.* 31 (2019) 100925.
- [153] S. Luo, Y. Su, Z. Wang, Tailored microstructures and strengthening mechanisms in an additively manufactured dual-phase high-entropy alloy via selective laser melting, *Sci. China Mater.* 63 (7) (2020) 1279–1290.
- [154] D. Choudhuri, B. Gwalani, S. Gorse, C.V. Mikler, R.V. Ramanujan, M.A. Gibson, R. Banerjee, Change in the primary solidification phase from FCC to BCC-based B2 in high entropy or complex concentrated alloys, *Scr. Mater.* 127 (2017) 186–190.
- [155] N. Malatji, T. Lengopeng, S. Pityana, A.P.I. Popoola, Microstructural, mechanical and electrochemical properties of AlCrFeCuNiWx high entropy alloys, *J. Mater. Res. Technol.* 11 (2021) 1594–1603.
- [156] D. Vogiatzief, A. Evirgen, S. Gein, V.R. Molina, A. Weisheit, M. Pedersen, Laser powder bed fusion and heat treatment of an AlCrFe<sub>2</sub>Ni<sub>2</sub> high entropy alloy, *Front. Mater.* 7 (2020) 248.
- [157] V.R. Molina, A. Weisheit, S. Gein, U. Hecht, D. Vogiatzief, Laser metal deposition of ultra-fine duplex AlCrFe<sub>2</sub>Ni<sub>2</sub>-based high-entropy alloy, *Front. Mater.* 7 (2020) 275.
- [158] H. Yao, Z. Tan, D. He, Z. Zhou, Z. Zhou, Y. Xue, L. Cui, L. Chen, G. Wang, Y. Yang, High strength and ductility AlCrFeNiV high entropy alloy with hierarchically heterogeneous microstructure prepared by selective laser melting, *J. Alloy Compd.* 813 (2020) 152196.
- [159] Y. Liao, P. Zhu, S. Li, Synthesis of AlFeCrNiV high entropy alloy by gas atomization and selective laser melting, *J. Multidisc. Eng. Sci. Technol.* 7 (3) (2020) 11591–11594.
- [160] V.V. Popov, A. Katz-Demyanetz, A. Koptuyug, M. Bamberger, Selective electron beam melting of Al<sub>0.5</sub>CrMoNbTa<sub>0.5</sub> high entropy alloys using elemental powder blend, *Heliyon* 5 (2) (2019) e01188.
- [161] A. Katz-Demyanetz, I.I. Gorbachev, E. Eshed, V.V. Popov, V.V. Popov, M. Bamberger, High entropy Al<sub>0.5</sub>CrMoNbTa<sub>0.5</sub> alloy: additive manufacturing vs. casting vs. CALPHAD approval calculations, *Mater. Charact.* 167 (2020) 110505.
- [162] B.A. Welk, M.A. Gibson, H.L. Fraser, A combinatorial approach to the investigation of metal systems that form both bulk metallic glasses and high entropy alloys, *JOM* 68 (3) (2016) 1021–1026.
- [163] S. Thapliyal, S.S. Nene, P. Agrawal, T. Wang, C. Morphew, R.S. Mishra, B.A. McWilliams, K.C. Cho, Damage-tolerant, corrosion-resistant high entropy alloy with high strength and ductility by laser powder bed fusion additive manufacturing, *Addit. Manuf.* 36 (2020) 101455.
- [164] Y. Hou, T. Liu, D. He, Z. Li, L. Chen, H. Su, P. Fu, P. Dai, W. Huang, Sustaining strength-ductility synergy of Slm Fe50Mn30Co10Cr10 metastable high-entropy alloy by Si addition. INTERMETALLICS-D-21-01005, Available at SSRN: <https://ssrn.com/abstract=3996888>.
- [165] G.J. Bi, Z.G. Zhu, Y.X. Chew, F.L. Ng, B.Y. Lee, Microstructure and mechanical characterization of laser aided additive manufactured Fe50Mn30Co10Cr10 high entropy alloy, *Lasers in Manufacturing Conference*, 2019.
- [166] P. Niu, R. Li, Z. Fan, T. Yuan, Z. Zhang, Additive manufacturing of TRIP-assisted dual-phases Fe50Mn30Co10Cr10 high-entropy alloy: Microstructure evolution, mechanical properties and deformation mechanisms, *Mater. Sci. Eng., A* 814 (2021) 141264.
- [167] Z.G. Zhu, X.H. An, W.J. Lu, Z.M. Li, F.L. Ng, X.Z. Liao, U. Ramamurty, S.M.L. Nai, J. Wei, Selective laser melting enabling the hierarchically heterogeneous microstructure and excellent mechanical properties in an interstitial solute strengthened high entropy alloy, *Mater. Res. Lett.* 7 (11) (2019) 453–459.
- [168] Y. Chew, Z.G. Zhu, F. Weng, S.B. Gao, F.L. Ng, B.Y. Lee, G.J. Bi, Microstructure and mechanical behavior of laser aided additive manufactured low carbon interstitial Fe49.5Mn30Co10Cr10Co0.5 multicomponent alloy, *J. Mater. Sci. Technol.* 77 (2021) 38–46.
- [169] J.W. Pegues, M.A. Melia, R. Puckett, S.R. Whetten, N. Argibay, A.B. Kustas, Exploring additive manufacturing as a high-throughput screening tool for multiphase high entropy alloys, *Addit. Manuf.* 37 (2021) 101598.
- [170] Z.G. Zhu, Q.B. Nguyen, F.L. Ng, X.H. An, X.Z. Liao, P.K. Liaw, S.M.L. Nai, J. Wei, Hierarchical microstructure and strengthening mechanisms of a CoCrFeNiMn high entropy alloy additively manufactured by selective laser melting, *Scr. Mater.* 154 (2018) 20–24.
- [171] Y.K. Kim, J. Choe, K.A. Lee, Selective laser melted equiatomic CoCrFeMnNi high-entropy alloy: microstructure, anisotropic mechanical response, and multiple strengthening mechanism, *J. Alloy Compd.* 805 (2019) 680–691.
- [172] Z. Xu, H. Zhang, W. Li, A. Mao, L. Wang, G. Song, Y. He, Microstructure and nanoindentation creep behavior of CoCrFeMnNi high-entropy alloy fabricated by selective laser melting, *Addit. Manuf.* 28 (2019) 766–771.
- [173] Y.H. Zhou, Z.H. Zhang, Y.P. Wang, G. Liu, S.Y. Zhou, Y.L. Li, J. Shen, M. Yan, Selective laser melting of typical metallic materials: an effective process prediction model developed by energy absorption and consumption analysis, *Addit. Manuf.* 25 (2019) 204–217.
- [174] P. Chen, S. Li, Y. Zhou, M. Yan, M.M. Attallah, Fabricating CoCrFeMnNi high entropy alloy via selective laser melting in-situ alloying, *J. Mater. Sci. Technol.* 43 (2020) 40–43.
- [175] Y.K. Kim, S. Yang, K.A. Lee, Compressive creep behavior of selective laser melted CoCrFeMnNi high-entropy alloy strengthened by in-situ formation of nano-oxides, *Addit. Manuf.* 36 (2020) 101543.
- [176] Y.K. Kim, S. Yang, K.A. Lee, Superior temperature-dependent mechanical properties and deformation behavior of equiatomic CoCrFeMnNi high-entropy alloy additively manufactured by selective laser melting, *Sci. Rep.* 10 (1) (2020) 8045.
- [177] H. Peng, Z. Lin, R. Li, P. Niu, Z. Zhang, Corrosion behavior of an equiatomic CoCrFeMnNi high-entropy alloy - a comparison between selective laser melting and cast, *Front. Mater.* 7 (2020) 244.
- [178] C. Zhang, K. Feng, H. Kokawa, B. Han, Z. Li, Cracking mechanism and mechanical properties of selective laser melted CoCrFeMnNi high entropy alloy using different scanning strategies, *Mater. Sci. Eng., A* 789 (2020) 139672.
- [179] D. Zhao, Q. Yang, D. Wang, M. Yan, P. Wang, M. Jiang, C. Liu, D. Diao, C. Lao, Z. Chen, Z. Liu, Y. Wu, Z. Lu, Ordered nitrogen complexes overcoming strength-ductility trade-off in an additively manufactured high-entropy alloy, *Virtual Phys. Prototyping* 15 (sup1) (2020) 532–542.
- [180] Y.-K. Kim, M.-S. Baek, S. Yang, K.-A. Lee, In-situ formed oxide enables extraordinary high-cycle fatigue resistance in additively manufactured CoCrFeMnNi high-entropy alloy, *Addit. Manuf.* 38 (2021) 101832.
- [181] B. Dovgvy, A. Piglione, P.A. Hooper, M.-S. Pham, Comprehensive assessment of the printability of CoNiCrFeMn in Laser Powder Bed Fusion, *Mater. Des.* 194 (2020) 108845.
- [182] P. Litwa, E. Hernandez-Nava, D. Guan, R. Goodall, K.K. Wika, The additive manufacturing processing and machinability of CrMnFeCoNi high entropy alloy, *Mater. Des.* 198 (2021) 109380.
- [183] Y.-K. Kim, M.-C. Kim, K.-A. Lee, 1.45 GPa ultrastrong cryogenic strength with superior impact toughness in the in-situ nano oxide reinforced CrMnFeCoNi high-entropy alloy matrix nanocomposite manufactured by laser powder bed fusion, *J. Mater. Sci. Technol.* 97 (2022) 10–19.
- [184] X.Y. He, H. Wang, Z.G. Zhu, L.Z. Wang, J.Q. Liu, N. Haghaddi, S.M.L. Nai, J. Huang, S. Primig, S.P. Ringer, X.Z. Liao, Texture evolution in a CrMnFeCoNi high-entropy alloy manufactured by laser powder bed fusion, *J. Mater. Sci.* (2022).
- [185] R. Li, P. Niu, T. Yuan, P. Cao, C. Chen, K. Zhou, Selective laser melting of an equiatomic CoCrFeMnNi high-entropy alloy: processability, non-equilibrium microstructure and mechanical property, *J. Alloy Compd.* 746 (2018) 125–134.
- [186] H. Wang, Z.G. Zhu, H. Chen, A.G. Wang, J.Q. Liu, H.W. Liu, R.K. Zheng, S.M.L. Nai, S. Primig, S.S. Babu, S.P. Ringer, X.Z. Liao, Effect of cyclic rapid thermal loadings on the microstructural evolution of a CrMnFeCoNi high-entropy alloy manufactured by selective laser melting, *Acta Mater.* 196 (2020) 609–625.
- [187] P. Chen, C. Yang, S. Li, M.M. Attallah, M. Yan, In-situ alloyed, oxide-dispersion-strengthened CoCrFeMnNi high entropy alloy fabricated via laser powder bed fusion, *Mater. Des.* 194 (2020) 108966.
- [188] J. Guo, M. Goh, Z. Zhu, X. Lee, M.L.S. Nai, J. Wei, On the machining of selective laser melting CoCrFeMnNi high-entropy alloy, *Mater. Des.* 153 (2018) 211–220.
- [189] J. Ren, C. Mahajan, L. Liu, D. Follette, W. Chen, S. Mukherjee, Corrosion behavior of selectively laser melted CoCrFeMnNi high entropy alloy, *Metals* 9 (10) (2019) 1029.
- [190] P. Niu, R. Li, S. Zhu, M. Wang, C. Chen, T. Yuan, Hot cracking, crystal orientation and compressive strength of an equimolar CoCrFeMnNi high-entropy alloy printed by selective laser melting, *Opt. Laser Technol.* 127 (2020) 106147.
- [191] N. Choi, V. Kulitckii, J. Kottke, B. Tas, J. Choe, J.H. Yu, S. Yang, J.H. Park, J.S. Lee, G. Wilde, S.V. Divinski, Analyzing the ‘non-equilibrium state’ of grain boundaries in additively manufactured high-entropy CoCrFeMnNi alloy using tracer diffusion measurements, *J. Alloy Compd.* 844 (2020) 155757.
- [192] M. Jin, A. Piglione, B. Dovgvy, E. Hosseini, P.A. Hooper, S.R. Holdsworth, M.S. Pham, Cyclic plasticity and fatigue damage of CrMnFeCoNi high entropy alloy fabricated by laser powder-bed fusion, *Addit. Manuf.* 36 (2020) 101584.
- [193] Y.K. Kim, J.Y. Suh, K.A. Lee, Effect of gaseous hydrogen embrittlement on the mechanical properties of additively manufactured CrMnFeCoNi high-entropy alloy strengthened by in-situ formed oxide, *Mater. Sci. Eng., A* 796 (2020) 140039.
- [194] Z. Xu, H. Zhang, X. Du, Y. He, H. Luo, G. Song, L. Mao, T. Zhou, L. Wang, Corrosion resistance enhancement of CoCrFeMnNi high-entropy alloy fabricated by additive manufacturing, *Corros. Sci.* 177 (2020) 108954.
- [195] H. Wang, Z.G. Zhu, H.S. Chen, S.M. Nai, X.H. An, R.K. Zheng, X.Z. Liao, Effect of cyclic thermal loadings on the microstructural evolution of a Cantor alloy in 3D printing processes, *Microsc. Microanal.* 25 (S2) (2019) 2568–2569.
- [196] C. Haase, F. Tang, M.B. Wilms, A. Weisheit, B. Hallstedt, Combining thermodynamic modeling and 3D printing of elemental powder blends for high-throughput investigation of high-entropy alloys - Towards rapid alloy screening and design, *Mater. Sci. Eng., A* 688 (2017) 180–189.
- [197] M.A. Melia, J.D. Carroll, S.R. Whetten, S.N. Esmaeely, J. Locke, E. White, I. Anderson, M. Chandross, J.R. Michael, N. Argibay, E.J. Schindelholz, A.B. Kustas, Mechanical and corrosion properties of additively manufactured CoCrFeMnNi high entropy alloy, *Addit. Manuf.* 29 (2019) 100833.
- [198] Z. Tong, X. Ren, J. Jiao, W. Zhou, Y. Ren, Y. Ye, E.A. Larson, J. Gu, Laser additive manufacturing of FeCrCoMnNi high-entropy alloy: effect of heat treatment on microstructure, residual stress and mechanical property, *J. Alloy Compd.* 785 (2019) 1144–1159.
- [199] S. Xiang, J. Li, H. Luan, A. Amar, S. Lu, K. Li, L. Zhang, X. Liu, G. Le, X. Wang, F. Qu, W. Zhang, D. Wang, Q. Li, Effects of process parameters on microstructures and tensile properties of laser melting deposited CrMnFeCoNi high entropy alloys, *Mater. Sci. Eng., A* 743 (2019) 412–417.
- [200] S. Guan, D. Guan, K. Solberg, F. Berto, T. Welo, T.M. Yee, K.C. Chan, Additive manufacturing of fine-grained and dislocation-populated CrMnFeCoNi high

- entropy alloy by laser engineered net shaping, *Mater. Sci. Eng., A* 761 (2019) 138056.
- [201] Z. Tong, H. Liu, J. Jiao, W. Zhou, Y. Yang, X. Ren, Laser additive manufacturing of CrMnFeCoNi high entropy alloy: microstructural evolution, high-temperature oxidation behavior and mechanism, *Opt. Laser Technol.* 130 (2020) 106326.
- [202] Z. Tong, H. Liu, J. Jiao, W. Zhou, Y. Yang, X. Ren, Microstructure, microhardness and residual stress of laser additive manufactured CoCrFeMnNi high-entropy alloy subjected to laser shock peening, *J. Mater. Process. Technol.* 285 (2020) 116806.
- [203] H.G. Li, T.L. Lee, W. Zheng, Y.Z. Lu, H.B.C. Yin, J.X. Yang, Y.J. Huang, J.F. Sun, Characterization of residual stress in laser melting deposited CoCrFeMnNi high entropy alloy by neutron diffraction, *Mater. Lett.* 263 (2020) 127247.
- [204] X. Zhang, R. Li, L. Huang, A. Amar, C. Wu, G. Le, X. Liu, D. Guan, G. Yang, J. Li, Influence of in-situ and ex-situ precipitations on microstructure and mechanical properties of additive manufacturing CoCrFeMnNi high-entropy alloys, *Vacuum* 187 (2021) 110111.
- [205] M.R. Jones, B.L. Naton, J.A. Wellington-Johnson, J.F. Curry, A.B. Kustas, P. Lu, M. Chandross, N. Argibay, Evidence of inverse Hall-Petch behavior and low friction and wear in high entropy alloys, *Sci. Rep.* 10 (1) (2020) 10151.
- [206] Y.L. Wang, L. Zhao, D. Wan, S. Guan, K.C. Chan, Additive manufacturing of TiB<sub>2</sub>-containing CoCrFeMnNi high-entropy alloy matrix composites with high density and enhanced mechanical properties, *Mater. Sci. Eng., A* 825 (2021) 141871.
- [207] M. Zheng, C. Li, X. Zhang, Z. Ye, X. Yang, J. Gu, The influence of columnar to equiaxed transition on deformation behavior of FeCoCrNiMn high entropy alloy fabricated by laser-based directed energy deposition, *Addit. Manuf.* 37 (2021) 101660.
- [208] H. Li, Y. Huang, S. Jiang, Y. Lu, X. Gao, X. Lu, Z. Ning, J. Sun, Columnar to equiaxed transition in additively manufactured CoCrFeMnNi high entropy alloy, *Mater. Des.* 197 (2021) 109262.
- [209] Y. Bai, H. Jiang, K. Yan, M. Li, Y. Wei, K. Zhang, B. Wei, Phase transition and heterogeneous strengthening mechanism in CoCrFeNiMn high-entropy alloy fabricated by laser-engineered net shaping via annealing at intermediate-temperature, *J. Mater. Sci. Technol.* 92 (2021) 129–137.
- [210] X. Gao, Y. Lu, Laser 3D printing of CoCrFeMnNi high-entropy alloy, *Mater. Lett.* 236 (2019) 77–80.
- [211] J. Li, H. Luan, L. Zhou, A. Amar, R. Li, L. Huang, C. Jiang, Phase transformation - induced strengthening of an additively manufactured multi-principal element CrMnFeCoNi alloy, *Mater. Des.* 195 (2020) 108999.
- [212] Y. Chew, G.J. Bi, Z.G. Zhu, F.L. Ng, F. Weng, S.B. Liu, S.M.L. Nai, B.Y. Lee, Microstructure and enhanced strength of laser aided additive manufactured CoCrFeNiMn high entropy alloy, *Mater. Sci. Eng., A* 744 (2019) 137–144.
- [213] P. Wang, P. Huang, F.L. Ng, W.J. Sin, S. Lu, M.L.S. Nai, Z. Dong, J. Wei, Additively manufactured CoCrFeNiMn high-entropy alloy via pre-alloyed powder, *Mater. Des.* 168 (2019) 107576.
- [214] M. Cagirci, P. Wang, F.L. Ng, M.L.S. Nai, J. Ding, J. Wei, Additive manufacturing of high-entropy alloys by thermophysical calculations and in situ alloying, *J. Mater. Sci. Technol.* 94 (2021) 53–66.
- [215] J.M. Park, J. Choe, J.G. Kim, J.W. Bae, J. Moon, S. Yang, K.T. Kim, J.H. Yu, H.S. Kim, Superior tensile properties of 1%C-CoCrFeMnNi high-entropy alloy additively manufactured by selective laser melting, *Mater. Res. Lett.* 8 (2019) 1638844.
- [216] J.M. Park, J. Choe, H.K. Park, S. Son, J. Jung, T.S. Kim, J.H. Yu, J.G. Kim, H.S. Kim, Synergetic strengthening of additively manufactured (CoCrFeMnNi)<sub>99</sub>C<sub>1</sub> high-entropy alloy by heterogeneous anisotropic microstructure, *Addit. Manuf.* 35 (2020) 101333.
- [217] J.G. Kim, J.M. Park, J.B. Seol, J. Choe, J.H. Yu, S. Yang, H.S. Kim, Nano-scale solute heterogeneities in the ultrastrong selectively laser melted carbon-doped CoCrFeMnNi alloy, *Mater. Sci. Eng., A* 773 (2019) 138726.
- [218] Y.-K. Kim, J.-H. Yu, H.S. Kim, K.-A. Lee, In-situ carbide-reinforced CoCrFeMnNi high-entropy alloy matrix nanocomposites manufactured by selective laser melting: Carbon content effects on microstructure, mechanical properties, and deformation mechanism, *Compos. B Eng.* 210 (2021) 108638.
- [219] R. Savinov, Y. Wang, J. Shi, Microstructure and properties of CeO<sub>2</sub>-doped CoCrFeMnNi high entropy alloy fabricated by laser metal deposition, *J. Manuf. Processes* 56 (2020) 1245–1251.
- [220] N. Li, S. Wu, D. Ouyang, J. Zhang, L. Liu, Fe-based metallic glass reinforced FeCoCrNiMn high entropy alloy through selective laser melting, *J. Alloy Compd.* 822 (2020) 153695.
- [221] L. Guo, J. Gu, B. Gan, S. Ni, Z. Bi, Z. Wang, M. Song, Effects of elemental segregation and scanning strategy on the mechanical properties and hot cracking of a selective laser melted FeCoCrNiMn-(N, Si) high entropy alloy, *J. Alloy Compd.* 865 (2021) 158892.
- [222] H. Chen, T. Lu, Y. Wang, Y. Liu, T. Shi, K.G. Prashanth, K. Kosiba, Laser additive manufacturing of nano-TiC particles reinforced CoCrFeMnNi high-entropy alloy matrix composites with high strength and ductility, *Mater. Sci. Eng., A* 833 (2022) 142512.
- [223] A. Amar, J. Li, S. Xiang, X. Liu, Y. Zhou, G. Le, X. Wang, F. Qu, S. Ma, W. Dong, Q. Li, Additive manufacturing of high-strength CrMnFeCoNi-based high entropy alloys with TiC addition, *Intermetallics* 109 (2019) 162–166.
- [224] B. Li, L. Zhang, Y. Xu, Z. Liu, B. Qian, F. Xuan, Selective laser melting of CoCrFeNiMn high entropy alloy powder modified with nano-TiN particles for additive manufacturing and strength enhancement: process, particle behavior and effects, *Powder Technol.* 360 (2020) 509–521.
- [225] B. Li, L. Zhang, B. Yang, Grain refinement and localized amorphization of additively manufactured high-entropy alloy matrix composites reinforced by nano ceramic particles via selective-laser-melting/remelting, *Composites, Communications* 19 (2020) 56–60.
- [226] B. Li, B. Qian, Y. Xu, Z. Liu, F. Xuan, Fine-structured CoCrFeNiMn high-entropy alloy matrix composite with 12 wt% TiN particle reinforcements via selective laser melting assisted additive manufacturing, *Mater. Lett.* 252 (2019) 88–91.
- [227] J. Li, S. Xiang, H. Luan, A. Amar, X. Liu, S. Lu, Y. Zeng, G. Le, X. Wang, F. Qu, C. Jiang, G. Yang, Additive manufacturing of high-strength CrMnFeCoNi high-entropy alloys-based composites with WC addition, *J. Mater. Sci. Technol.* 35 (2019) 2430–2434.
- [228] P. Agrawal, S. Thapliyal, S.S. Nene, R.S. Mishra, B.A. McWilliams, K.C. Cho, Excellent strength-ductility synergy in metastable high entropy alloy by laser powder bed additive manufacturing, *Addit. Manuf.* 32 (2020) 101098.
- [229] Q. Wang, A. Amar, C. Jiang, H. Luan, S. Zhao, H. Zhang, G. Le, X. Liu, X. Wang, X. Yang, J. Li, CoCrFeNiMo<sub>0.2</sub> high entropy alloy by laser melting deposition: Prospective material for low temperature and corrosion resistant applications, *Intermetallics* 119 (2020) 106727.
- [230] T. Fujieda, M. Chen, H. Shiratori, K. Kuwabara, K. Yamanaka, Y. Koizumi, A. Chiba, S. Watanabe, Mechanical and corrosion properties of CoCrFeNiTi-based high-entropy alloy additive manufactured using selective laser melting, *Addit. Manuf.* 25 (2019) 412–420.
- [231] T. Ikeda, M. Yonehara, T.-T. Ikeshoji, T. Nobuki, M. Hatate, K. Kuwabara, Y. Otsubo, H. Kyogoku, Influences of Process Parameters on the Microstructure and Mechanical Properties of CoCrFeNiTi Based High-Entropy Alloy in a Laser Powder Bed Fusion Process, *Crystals* 11 (5) (2021) 549.
- [232] K. Zhou, Z. Wang, F. He, S. Liu, J. Li, J. Kai, J. Wang, A precipitation-strengthened high-entropy alloy for additive manufacturing, *Addit. Manuf.* 35 (2020) 101410.
- [233] D. Lin, L. Xu, H. Jing, Y. Han, L. Zhao, F. Minami, Effects of annealing on the structure and mechanical properties of FeCoCrNi high-entropy alloy fabricated via selective laser melting, *Addit. Manuf.* 32 (2020) 101058.
- [234] D. Lin, L. Xu, H. Jing, Y. Han, L. Zhao, Y. Zhang, H. Li, A strong, ductile, high-entropy FeCoCrNi alloy with fine grains fabricated via additive manufacturing and a single cold deformation and annealing cycle, *Addit. Manuf.* 36 (2020) 101591.
- [235] D. Lin, L. Xu, Y. Han, Y. Zhang, H. Jing, L. Zhao, F. Minami, Structure and mechanical properties of a FeCoCrNi high-entropy alloy fabricated via selective laser melting, *Intermetallics* 127 (2020) 106963.
- [236] M. Song, R. Zhou, J. Gu, Z. Wang, S. Ni, Y. Liu, Nitrogen induced heterogeneous structures overcome strength-ductility trade-off in an additively manufactured high-entropy alloy, *Appl. Mater. Today* 18 (2020) 100498.
- [237] Y.O. Kuzminova, D.G. Firsov, S.A. Dagesyan, S.D. Konev, S.N. Sergeev, A.P. Zhilyaev, M. Kawasaki, I.S. Akhatov, S.A. Evlashin, Fatigue behavior of additive manufactured CrFeCoNi medium-entropy alloy, *J. Alloy Compd.* 863 (2021) 158609.
- [238] W. Zhao, J.-K. Han, Y.O. Kuzminova, S.A. Evlashin, A.P. Zhilyaev, A.M. Pesin, J.-I. Jang, K.-D. Liss, M. Kawasaki, Significance of grain refinement on micro-mechanical properties and structures of additively-manufactured CoCrFeNi high-entropy alloy, *Mater. Sci. Eng., A* 807 (2021) 140898.
- [239] X.-H. Gu, T. Lu, T. Zhang, W. Guo, Y. Pan, T. Dai, Anisotropy of microstructures and mechanical properties in FeCoNiCr<sub>0.5</sub> high-entropy alloy prepared via selective laser melting, *Rare Met.* 41 (2022) 2047–2054.
- [240] Y. Kuzminova, D. Firsov, A. Dudin, S. Sergeev, A. Zhilyaev, A. Dyakov, A. Chupueva, A. Alekseev, D. Martynov, I. Akhatov, S. Evlashin, The effect of the parameters of the powder bed fusion process on the microstructure and mechanical properties of CrFeCoNi medium-entropy alloys, *Intermetallics* 116 (2020) 106651.
- [241] J.M. Park, P. Asghari-Rad, A. Zargarani, J.W. Bae, J. Moon, H. Kwon, J. Choe, S. Yang, J.-H. Yu, H.S. Kim, Nano-scale heterogeneity-driven metastability engineering in ferrous medium-entropy alloy induced by additive manufacturing, *Acta Mater.* 221 (2021) 117426.
- [242] Z. Sun, X.P. Tan, M. Descroins, D. Mangelinck, S.B. Tor, C.S. Lim, Revealing hot tearing mechanism for an additively manufactured high-entropy alloy via selective laser melting, *Scr. Mater.* 168 (2019) 129–133.
- [243] Y. Cai, M. Shan, Y. Cui, S.M. Manladan, X. Lv, L. Zhu, J. Han, Microstructure and properties of FeCoCrNi high entropy alloy produced by laser melting deposition, *J. Alloy Compd.* 887 (2021) 161323.
- [244] M.R. Barnett, M. Senadeera, D. Fabijanic, K.F. Shamlay, J. Joseph, S.R. Kada, S. Rana, S. Gupta, S. Venkatesh, A scrap-tolerant alloying concept based on high entropy alloys, *Acta Mater.* 200 (2020) 735–744.
- [245] G.M. Karthik, S. Panikar, G.D.J. Ram, R.S. Kottada, Additive manufacturing of an aluminum matrix composite reinforced with nanocrystalline high-entropy alloy particles, *Mater. Sci. Eng., A* 679 (2017) 193–203.
- [246] R. Zhou, Y. Liu, C. Zhou, S. Li, W. Wu, M. Song, B. Liu, X. Liang, P.K. Liaw, Microstructures and mechanical properties of C-containing FeCoCrNi high-entropy alloy fabricated by selective laser melting, *Intermetallics* 94 (2018) 165–171.
- [247] R. Zhou, Y. Liu, B. Liu, J. Li, Q. Fang, Precipitation behavior of selective laser melted FeCoCrNi<sub>0.05</sub> high entropy alloy, *Intermetallics* 106 (2019) 20–25.
- [248] W. Wu, R. Zhou, B. Wei, S. Ni, Y. Liu, M. Song, Nanosized precipitates and dislocation networks reinforced C-containing CoCrFeNi high-entropy alloy fabricated by selective laser melting, *Mater. Charact.* 144 (2018) 605–610.
- [249] Z. Wang, J. Gu, D. An, Y. Liu, M. Song, Characterization of the microstructure and deformation substructure evolution in a hierarchical high-entropy alloy by correlative EBSD and ECCI, *Intermetallics* 121 (2020) 106788.

- [250] Y. Peng, Y. Kong, W. Zhang, M. Zhang, H. Wang, Effect of diffusion barrier and interfacial strengthening on the interface behavior between high entropy alloy and diamond, *J. Alloy Compd.* 852 (2021) 157023.
- [251] D. Lin, L. Xu, X. Li, H. Jing, G. Qin, H. Pang, F. Minami, A Si-containing FeCoCrNi high-entropy alloy with high strength and ductility synthesized in situ via selective laser melting, *Addit. Manuf.* 35 (2020) 101340.
- [252] Z. Gu, X. Su, W. Peng, W. Guo, S. Xi, X. Zhang, H. Tu, Y. Gao, H. Wu, An important improvement of strength and ductility on a new type of CoCr<sub>2.5</sub>FeNi<sub>2</sub>TiW<sub>0.5</sub> high entropy alloys under two different protective gases by selective laser melting, *J. Alloy Compd.* 868 (2021) 159088.
- [253] C.K. Ng, K. Bai, D. Wu, K.B. Lau, J.J. Lee, A.K.H. Cheong, F. Wei, B. Cheng, P. Wang, D.C.C. Tan, Y.-W. Zhang, Additive manufacturing of high-strength and ductile high entropy alloy CoCrFeNiW<sub>0.2</sub> composites via laser powder bed fusion and post-annealing, *J. Alloy Compd.* 906 (2022) 164288.
- [254] S. Xia, Z. Xia, D. Zhao, Y. Xie, X. Liu, L. Wang, Microstructure formation mechanism and corrosion behavior of FeCrCuTiV two-phase high entropy alloy prepared by different processes, *Fusion Eng. Des.* 172 (2021) 112792.
- [255] X. Yang, Y. Ge, J. Lehtonen, S.P. Hannula, Hierarchical Microstructure of Laser Powder Bed Fusion Produced Face-Centered-Cubic-Structured Equiatomic CrFeNiMn Multicomponent Alloy, *Materials* 13 (20) (2020) 4498.
- [256] G. Huser, I. Demirci, P. Aubry, I. Guillot, L. Perrière, E. Rigal, H. Maskrot, Study of the elaboration of high entropy material from powder by laser additive manufacturing, *Procedia CIRP* 94 (2020) 270–275.
- [257] B.W. Wang, P. Luo, L.J. Zhang, B.H. Lu, Selective laser melting of multi-principal NiCrWFeTi alloy: processing, microstructure and performance, *Mater. Sci. Forum* 944 (2019) 182–189.
- [258] X. Yang, Y. Zhou, S. Xi, Z. Chen, P. Wei, C. He, T. Li, Y. Gao, H. Wu, Grain-anisotropied high-strength Ni<sub>6</sub>Cr<sub>4</sub>WFe<sub>3</sub>Ti high entropy alloys with outstanding tensile ductility, *Mater. Sci. Eng., A* 767 (2019) 138382.
- [259] X. Yang, Y. Zhou, S. Xi, Z. Chen, P. Wei, C. He, T. Li, Y. Gao, H. Wu, Additively manufactured fine grained Ni<sub>6</sub>Cr<sub>4</sub>WFe<sub>3</sub>Ti high entropy alloys with high strength and ductility, *Mater. Sci. Eng., A* 767 (2019) 138394.
- [260] I. Kuncce, M. Polański, T. Czujko, Microstructures and hydrogen storage properties of LaNiFeVMn alloys, *Int. J. Hydrogen Energy* 42 (44) (2017) 27154–27164.
- [261] H. Dobbelstein, E.P. George, E.L. Gurevich, A. Kostka, A. Ostendorf, G. Laplanche, Laser metal deposition of refractory high-entropy alloys for high-throughput synthesis and structure-property characterization, *Int. J. Extreme Manuf.* 3 (1) (2021) 015201.
- [262] H. Zhang, Y. Zhao, J. Cai, S. Ji, J. Geng, X. Sun, D. Li, High-strength NbMoTaX refractory high-entropy alloy with low stacking fault energy eutectic phase via laser additive manufacturing, *Mater. Des.* 201 (2021) 109462.
- [263] T. Ishimoto, R. Ozasa, K. Nakano, M. Weinmann, C. Schmitter, M. Stenzel, A. Matsugaki, T. Nagase, T. Matsuzaka, M. Todai, H.S. Kim, T. Nakano, Development of TiNbTaZrMo bio-high entropy alloy (BioHEA) super-solid solution by selective laser melting, and its improved mechanical property and biocompatibility, *Scr. Mater.* 194 (2021) 113658.
- [264] F. Huber, D. Bartels, M. Schmidt, In-situ alloy formation of a WMoTaNbV refractory metal high entropy alloy by laser powder bed fusion (LPBF-LB/M), *Materials* 14 (11) (2021) 3095.
- [265] H. Zhang, Y. Zhao, S. Huang, S. Zhu, F. Wang, D. Li, Manufacturing and analysis of high-performance refractory high-entropy alloy via selective laser melting (SLM), *Materials* 12 (5) (2019) 720.
- [266] H. Zhang, W. Xu, Y. Xu, Z. Lu, D. Li, The thermal-mechanical behavior of WTaMoNb high-entropy alloy via selective laser melting (SLM): experiment and simulation, *Int. J. Adv. Manuf. Technol.* 96 (1–4) (2018) 461–474.
- [267] M. Moorehead, K. Bertsch, M. Niezgodka, C. Parkin, M. Elbakhshwan, K. Sridharan, C. Zhang, D. Thoma, A. Couet, High-throughput synthesis of Mo-Nb-Ta-W high-entropy alloys via additive manufacturing, *Mater. Des.* 187 (2019) 108358.
- [268] Q. Li, H. Zhang, D. Li, Z. Chen, S. Huang, Z. Lu, H. Yan, W<sub>x</sub>NbMoTa refractory high-entropy alloys fabricated by laser cladding deposition, *Materials* 12 (3) (2019) 533.
- [269] J. Liu, J. Li, X. Du, Y. Tong, R. Wang, D. He, Z. Cai, H. Wang, Microstructure and mechanical properties of wire arc additively manufactured MoNbTaWTi high entropy alloys, *Materials* 14 (16) (2021) 4512.
- [270] I. Kuncce, M. Polanski, J. Bystrzycki, Microstructure and hydrogen storage properties of a TiZrNbMoV high entropy alloy synthesized using laser engineered net shaping (LENS), *Int. J. Hydrogen Energy* 39 (18) (2014) 9904–9910.
- [271] I. Maskery, N.T. Aboulkhair, M.R. Corfield, C. Tuck, A.T. Clare, R.K. Leach, R.D. Wildman, I.A. Ashcroft, R.J.M. Hague, Quantification and characterisation of porosity in selectively laser melted Al–Si10–Mg using X-ray computed tomography, *Mater. Charact.* 111 (2016) 193–204.
- [272] D. Gu, Y.C. Hagedorn, W. Meiners, G. Meng, R.J.S. Batista, K. Wissenbach, R. Poprawe, Densification behavior, microstructure evolution, and wear performance of selective laser melting processed commercially pure titanium, *Acta Mater.* 60 (9) (2012) 3849–3860.
- [273] X.J. Wang, L.C. Zhang, M.H. Fang, T.B. Sercombe, The effect of atmosphere on the structure and properties of a selective laser melted Al–12Si alloy, *Mater. Sci. Eng., A* 597 (2014) 370–375.
- [274] S. Marola, S. Bosia, A. Veltro, G. Fiore, D. Manfredi, M. Lombardi, G. Amato, M. Baricco, L. Bettezzati, Residual stresses in additively manufactured AlSi10Mg: Raman spectroscopy and X-ray diffraction analysis, *Mater. Des.* 202 (2021) 109550.
- [275] S. Goel, M. Neikter, J. Capek, E. Polatidis, M.H. Colliander, S. Joshi, R. Pederson, Residual stress determination by neutron diffraction in powder bed fusion-built Alloy 718: Influence of process parameters and post-treatment, *Mater. Des.* 195 (2020) 109045.
- [276] F.C. Liu, X. Lin, G.L. Yang, M.H. Song, J. Chen, W.D. Huang, Microstructure and residual stress of laser rapid formed Inconel 718 nickel-base superalloy, *Opt. Laser Technol.* 43 (2011) 208–213.
- [277] H. Attar, M. Calin, L.C. Zhang, S. Scudino, J. Eckert, Manufacture by selective laser melting and mechanical behavior of commercially pure titanium, *Mater. Sci. Eng., A* 593 (2014) 170–177.
- [278] P. Mercelis, J.P. Kruth, Residual stresses in selective laser sintering and selective laser melting, *Rapid Prototyping J.* 12 (2006) 254–265.
- [279] M. Strantz, R.K. Ganerwala, B. Clausen, T.Q. Phan, L.E. Levine, D. Pagan, W.E. King, N.E. Hodge, D.W. Brown, Coupled experimental and computational study of residual stresses in additively manufactured Ti-6Al-4V components, *Mater. Lett.* 231 (2018) 221–224.
- [280] F. Liu, X. Lin, C. Huang, M. Song, G. Yang, J. Chen, W. Huang, The effect of laser scanning path on microstructures and mechanical properties of laser solid formed nickel-base superalloy Inconel 718, *J. Alloy Compd.* 509 (13) (2011) 4505–4509.
- [281] Y. Liu, Y. Yang, D. Wang, A study on the residual stress during selective laser melting (SLM) of metallic powder, *Int. J. Adv. Manuf. Technol.* 87 (2016) 647–656.
- [282] T.L. Lee, J. Mi, S. Ren, S. Zhao, J. Fan, S. Kabra, S. Zhang, P.S. Grant, Modelling and neutron diffraction characterization of the interfacial bonding of spray formed dissimilar steels, *Acta Mater.* 155 (2018) 318–330.
- [283] W. Xing, D. Ouyang, N. Li, L. Liu, Estimation of residual stress in selective laser melting of a Zr-based amorphous alloy, *Materials* 11 (2018) 1480.
- [284] L. Parry, I.A. Ashcroft, R.D. Wildman, Understanding the effect of laser scan strategy on residual stress in selective laser melting through thermo-mechanical simulation, *Addit. Manuf.* 12 (2016) 1–15.
- [285] B. Song, S.J. Dong, Q. Liu, H.L. Liao, C. Coddet, Vacuum heat treatment of iron parts produced by selective laser melting: microstructure, residual stress and tensile behavior, *Mater. Des.* 54 (2014) 727–733.
- [286] R. Rodriguez, R.W. Hayes, P.B. Berbon, E.J. Lavernia, Tensile and creep behavior of cryomilled Inco 625, *Acta Mater.* 51 (2003) 911–929.
- [287] P. Pratt, S.D. Felicelli, L. Wang, C.R. Hubbard, Residual stress measurement of laser-engineered net shaping AISI410 thin plates using neutron diffraction, *Metall. Mater. Trans. A* 39 (2008) 3155–3163.
- [288] D.D. Gu, W. Meiners, K. Wissenbach, R. Poprawe, Laser additive manufacturing of metallic components: materials, processes and mechanisms, *Int. Mater. Rev.* 57 (3) (2012) 133–164.
- [289] W. Kurz, C. Bezençon, M. Gäumann, Columnar to equiaxed transition in solidification processing, *Sci. Technol. Adv. Mater.* 2 (2001) 185–191.
- [290] M. Rappaz, J.M. Drezet, M.A. Gremaud, A new hot-tearing criterion, *Metall. Mater. Trans. A* 30 (1999) 449–455.
- [291] M. Laurent-Brocq, A. Akhatova, L. Perrière, S. Chebini, X. Sauvage, E. Leroy, Y. Champion, Insights into the phase diagram of the CrMnFeCoNi high entropy alloy, *Acta Mater.* 88 (2015) 355–365.
- [292] Z. Tang, M.C. Gao, H. Diao, T. Yang, J. Liu, T. Zuo, Y. Zhang, Z. Lu, Y. Cheng, Y. Zhang, K.A. Dahmen, P.K. Liaw, Aluminum alloying effects on lattice types, microstructures, and mechanical behavior of high-entropy alloys systems, *JOM* 65 (2013) 1848–1858.
- [293] X.P. Ren, H.Q. Li, H. Guo, F.L. Shen, C.X. Qin, E.T. Zhao, X.Y. Fang, A comparative study on mechanical properties of Ti–6Al–4V alloy processed by additive manufacturing vs. traditional processing, *Mater. Sci. Eng., A* 817 (2021) 141384.
- [294] Z. Xiao, C. Chen, H. Zhu, Z. Hu, B. Nagarajan, L. Guo, X. Zeng, Study of residual stress in selective laser melting of Ti6Al4V, *Mater. Des.* 193 (2020) 108846.
- [295] J.J. Lewandowski, M. Seifi, Metal additive manufacturing: a review of mechanical properties, *Annu. Rev. Mater. Res.* 46 (1) (2016) 151–186.
- [296] S. Wang, Atomic structure modeling of multi-principal-element alloys by the principle of maximum entropy, *Entropy* 15 (2013) 5536–5548.
- [297] W.R. Wang, W.L. Wang, S.C. Wang, Y.C. Tsai, C.H. Lai, J.W. Yeh, Effects of Al addition on the microstructure and mechanical property of Al<sub>x</sub>CoCrFeNi high-entropy alloys, *Intermetallics* 26 (2012) 44–51.
- [298] C.J. Tong, M.R. Chen, S.K. Chen, J.W. Yeh, T.T. Shun, S.J. Lin, S.Y. Chang, Mechanical performance of the Al<sub>2</sub>CoCrCuFeNi high-entropy alloy system with multiprincipal elements, *Metall. Mater. Trans. A* 36 (2005) 1263–1271.
- [299] O.N. Senkov, G.B. Wilks, J.M. Scott, D.B. Miracle, Mechanical properties of Nb<sub>25</sub>Mo<sub>25</sub>Ta<sub>25</sub>W<sub>25</sub> and V<sub>20</sub>Nb<sub>20</sub>Mo<sub>20</sub>Ta<sub>20</sub>W<sub>20</sub> refractory high entropy alloys, *Intermetallics* 19 (5) (2011) 698–706.
- [300] Y. Chang, C.Y. Wang, K.M. Zhao, H. Dong, J.W. Yan, An introduction to medium-Mn steel: metallurgy, mechanical properties and warm stamping process, *Mater. Des.* 94 (2016) 424–432.
- [301] S. Suresh, *Fatigue of Materials*, second ed., Cambridge University Press, Cambridge, 1998.
- [302] J. Schijve, *Fatigue of structures and materials in the 20th century and the state of the art*, *Int. J. Fatigue* 25 (8) (2003) 679–702.
- [303] K.V.S. Thurston, B. Gludovatz, Q. Yu, G. Laplanche, E.P. George, R.O. Ritchie, Temperature and load-ratio dependent fatigue-crack growth in the CrMnFeCoNi high-entropy alloy, *J. Alloy Compd.* 794 (2019) 525–533.
- [304] Y. Ma, G.J. Peng, D.H. Wen, T.H. Zhang, Nanoindentation creep behavior in a CoCrFeCuNi high-entropy alloy film with two different structure states, *Mater. Sci. Eng., A* 621 (2015) 111–117.

- [305] D.H. Lee, M.Y. Seok, Y. Zhao, I.C. Choi, J. He, Z. Lu, J.Y. Suh, U. Ramamurty, M. Kawasaki, T.G. Langdon, J. Il Jang, Spherical nanoindentation creep behavior of nanocrystalline and coarse-grained CoCrFeMnNi high-entropy alloys, *Acta Mater.* 109 (2016) 314–322.
- [306] Z. Li, C. Tasan, H. Springer, B. Gault, D. Raabe, Interstitial atoms enable joint twinning and transformation induced plasticity in strong and ductile high-entropy alloys, *Sci. Rep.* 7 (2017) 40704.
- [307] E. Akiba, H. Iba, Hydrogen absorption by Laves phase related BCC solid solution, *Intermetallics* 6 (6) (1998) 461–470.
- [308] J. Huot, H. Enoki, E. Akiba, Synthesis, phase transformation, and hydrogen storage properties of ball-milled TiV<sub>0.9</sub>Mn<sub>1.1</sub>, *J. Alloy Compd.* 453 (1) (2008) 203–209.
- [309] J. Montero, G. Ek, L. Laversenne, V. Nassif, G. Zepon, M. Sahlberg, C. Zlotea, Hydrogen storage properties of the refractory Ti–V–Zr–Nb–Ta multi-principal element alloy, *J. Alloy Compd.* 835 (2020) 155376.
- [310] M.M. Nygård, G. Ek, D. Karlsson, M.H. Sørby, M. Sahlberg, B.C. Hauback, Counting electrons - a new approach to tailor the hydrogen sorption properties of high-entropy alloys, *Acta Mater.* 175 (2019) 121–129.
- [311] F. Weng, Y. Chew, Z. Zhu, X. Yao, L. Wang, F.L. Ng, S. Liu, G. Bi, Excellent combination of strength and ductility of CoCrNi medium entropy alloy fabricated by laser aided additive manufacturing, *Addit. Manuf.* 34 (2020) 101202.
- [312] C.E. Slone, J. Miao, E.P. George, M.J. Mills, Achieving ultra-high strength and ductility in equiatomic CrCoNi with partially recrystallized microstructures, *Acta Mater.* 165 (2019) 496–507.
- [313] B. Gludovatz, A. Hohenwarter, K.V.S. Thurston, H. Bei, Z. Wu, E.P. George, R.O. Ritchie, Exceptional damage-tolerance of a medium-entropy alloy CrCoNi at cryogenic temperatures, *Nat. Commun.* 7 (1) (2016) 10602.
- [314] G. Laplanche, A. Kostka, C. Reinhart, J. Hunfeld, G. Eggeler, E.P. George, Reasons for the superior mechanical properties of medium-entropy CrCoNi compared to high-entropy CrMnFeCoNi, *Acta Mater.* 128 (2017) 292–303.
- [315] J. Miao, C.E. Slone, T.M. Smith, C. Niu, H. Bei, M. Ghazisaeidi, G.M. Pharr, M.J. Mills, The evolution of the deformation substructure in a Ni-Co-Cr equiatomic solid solution alloy, *Acta Mater.* 132 (2017) 35–48.
- [316] S.S. Sohn, A. Kwiatkowski da Silva, Y. Ikeda, F. Kormann, W. Lu, W.S. Choi, B. Gault, D. Ponge, J. Neugebauer, D. Raabe, Ultrastrong medium-entropy single-phase alloys designed via severe lattice distortion, *Adv. Mater.* 31 (8) (2019) e1807142.
- [317] T.M. Smith, A.C. Thompson, T.P. Gabb, C.L. Bowman, C.A. Kantzos, Efficient production of a high-performance dispersion strengthened, multi-principal element alloy, *Sci. Rep.* 10 (1) (2020) 9663.
- [318] H. Chang, T.W. Zhang, S.G. Ma, D. Zhao, R.L. Xiong, T. Wang, Z.Q. Li, Z.H. Wang, Novel Si-added CrCoNi medium entropy alloys achieving the breakthrough of strength-ductility trade-off, *Mater. Des.* 197 (2021) 109202.
- [319] S.Y. Lee, S. Byeon, H.S. Kim, H. Jin, S. Lee, Deep learning-based phase prediction of high-entropy alloys: Optimization, generation, and explanation, *Mater. Des.* 197 (2021) 109260.
- [320] Y. Zeng, M. Man, K. Bai, Y.W. Zhang, Revealing high-fidelity phase selection rules for high entropy alloys: A combined CALPHAD and machine learning study, *Mater. Des.* 202 (2021) 109532.
- [321] C. Kenel, N.P.M. Casati, D.C. Dunand, 3D ink-extrusion additive manufacturing of CoCrFeNi high-entropy alloy micro-lattices, *Nat. Commun.* 10 (1) (2019) 904.
- [322] S. Peng, S. Mooraj, R. Feng, L. Liu, J. Ren, Y. Liu, F. Kong, Z. Xiao, C. Zhu, P.K. Liaw, W. Chen, Additive manufacturing of three-dimensional (3D)-architected CoCrFeNiMn high-entropy alloy with great energy absorption, *Scr. Mater.* 190 (2021) 46–51.
- [323] Z. Xu, Z. Zhu, P. Wang, G.K. Meenashisundaram, S.M.L. Nai, J. Wei, Fabrication of porous CoCrFeMnNi high entropy alloy using binder jetting additive manufacturing, *Addit. Manuf.* 35 (2020) 101441.
- [324] D. Karlsson, G. Lindwall, A. Lundbäck, M. Amnebrink, M. Boström, L. Riekehr, M. Schuisky, M. Sahlberg, U. Jansson, Binder jetting of the AlCoCrFeNi alloy, *Addit. Manuf.* 27 (2019) 72–79.
- [325] Q. Shen, X. Kong, X. Chen, X. Yao, V.B. Deev, E.S. Prusov, Powder plasma arc additive manufactured CoCrFeNi(SiC)<sub>x</sub> high-entropy alloys: microstructure and mechanical properties, *Mater. Lett.* 282 (2021) 128736.
- [326] Y. Zhang, X. Chen, S. Jayalakshmi, R.A. Singh, V.B. Deev, E.S. Prusov, Factors determining solid solution phase formation and stability in CoCrFeNiX<sub>0.4</sub> (X=Al, Nb, Ta) high entropy alloys fabricated by powder plasma arc additive manufacturing, *J. Alloy Compd.* 857 (2021) 157625.
- [327] Y. Zhang, Q. Shen, X. Chen, S. Jayalakshmi, R.A. Singh, S. Kononov, V.B. Deev, E.S. Prusov, Strengthening Mechanisms in CoCrFeNiX<sub>0.4</sub> (Al, Nb, Ta) High Entropy Alloys Fabricated by Powder Plasma Arc Additive Manufacturing, *Nanomaterials (Basel)* 11 (3) (2021).
- [328] B. Dong, Z. Wang, Z. Pan, O. Muránský, C. Shen, M. Reid, B. Wu, X. Chen, H. Li, On the development of pseudo-eutectic AlCoCrFeNi<sub>2.1</sub> high entropy alloy using Powder-bed Arc Additive Manufacturing (PAAM) process, *Mater. Sci. Eng., A* 802 (2021) 140639.